Generating Point Cloud Failure Surface of Polymeric Unidirectional Composites Using Virtual Tests

by

Daniel Mutahwa Katusele

A Thesis Presented in Partial Fulfillment
of the Requirements for the Degree
Master of Science

Approved July 2021 by the
Graduate Supervisory Committee:

Subramaniam Rajan, Chair
Barzin Mobasher
Narayanan Neithalath

ARIZONA STATE UNIVERSITY

August 2021

ABSTRACT

Composite materials have gained interest in the aerospace, mechanical and civil engineering industries due to their desirable properties - high specific strength and modulus, and superior resistance to fatigue. Design engineers greatly benefit from a reliable predictive tool that can calculate the deformations, strains, and stresses of composites under uniaxial and multiaxial states of loading including damage and failure predictions. Obtaining this information from (laboratory) experimental testing is costly, time consuming, and sometimes, impractical. On the other hand, numerical modeling of composite materials provides a tool (virtual testing) that can be used as a supplemental and an alternate procedure to obtain data that either cannot be readily obtained via experiments or is not possible with the currently available experimental setup. In this study, a unidirectional composite (Toray T800-F3900) is modeled at the constituent level using repeated unit cells (RUC) so as to obtain homogenized response all the way from the unloaded state up until failure (defined as complete loss of load carrying capacity). The RUC-based model is first calibrated and validated against the principal material direction laboratory tests involving unidirectional loading states. Subsequently, the models are subjected to multi-directional states of loading to generate a point cloud failure data under in-plane and out-of-plane biaxial loading conditions. Failure surfaces thus generated are plotted and compared against analytical failure theories. Results indicate that the developed process and framework can be used to generate a reliable failure prediction procedure that can possibly be used for a variety of composite systems.

DEDICATION

This thesis is dedicated to my parents. My late father Katusele Deogratias and my mother Kavira Godiane have always encouraged me to embrace my dreams and follow through every challenge I encounter on the way. Their love has been the backbone of my desire to always aim higher. I also dedicate this thesis to my siblings Eric, Grâce, Gloire, Dieudonné and Nathalie Katusele whose support has always made me feel loved.

ACKNOWLEDGMENTS

My utmost gratitude goes to Dr. Subramaniam Rajan for his unrelenting mentorship and guidance throughout the preparation of this thesis and for serving as my defense committee chair. I would like to also thank Dr. Barzin Mobasher and Dr. Narayanan Neithalath for their serving as committee members and for the teaching they provided me. Finally, my gratitude goes to Dr. Bilal Khaled and Dr. Loukham Shyamsunder for their continued guidance and mentorship.

TABLE OF CONTENTS

CHAPTER Page

LIST OF TABLES

Table Page

Table Page

LIST OF FIGURES

Figure Page

Figure Page

Figure Page

Figure Page

Figure Page

Figure Page

Figure Page

1. INTRODUCTION

1.1. BACKGROUND AND LITERATURE REVIEW

Composite materials have become ubiquitous in aerospace, mechanical and civil engineering applications due to the advantages they offer over conventional materials such as aluminum and steel. Some of the applications where fiber-reinforced polymer composites are used include aircraft, yachts, motor vehicles, chemical and process plant, sporting goods, military equipment, etc. In the design of structural components made of fiber-reinforced polymeric composite materials, engineers assess the performance of the structure through a complex combination of testing and analysis for structural performance and durability. This, however, is a costly and time-consuming process.

Alternatively, numerical simulations are being used in various industries to predict the behavior of fiber-reinforced composite materials. In structures-based industries, e.g., aerospace and automotive industries, design engineers execute high fidelity finite element (FE) models that include the capability to simulate the behavior of fiber reinforced composites. The FE models are used to simulate elastic and inelastic deformation, damage, failure initiation as well as failure progression. The anisotropic behavior of carbon fiber reinforced composites coupled with the complexity of its architecture renders the predictions of its behavior, including failure, a challenging task for researchers and design engineers. The development of numerical tools to predict the behavior of composite materials, including failure, in uniaxial and multiaxial loading is very important for assessing the performance of composite structures (Camanho, et al.,

2015) as well as design and manufacturing of new components (Kaddour & Hinton, 2010).

Failure Modeling and Predictions

Unlike homogeneous and isotropic materials whose failure criteria can be modeled relatively easily from micromechanical or phenomenological considerations due to the existence of a few failure mechanisms at critical stresses (Totry, et al., 2008a), polymer matrix composites (PMC) exhibit various failure modes based on loading direction, state of stress, and manufacturing defects. The failure modes in PMC include fiber failure modes such as fiber breakage in longitudinal tension and localized fiber buckling in longitudinal compression, and matrix failure modes such as matrix cracking in transverse tension and fracture due to formation of matrix shear bands in transverse compression and in-plane shear (Hinton, et al., 2004a). The prediction of failure involving various mechanisms and under different loading conditions has been the focus of research for many decades.

To assess the accuracy and establish a level of confidence in various failure criteria proposed over the years, World-Wide Failure Exercises (WWFE) have been organized where participants have used experimental data to validate their theories (Hinton, et al., 2004b). The first World-Wide Failure Exercise (WWFE-I) focused on response of fiber-reinforced polymer composites under in-plane biaxial loading in absence of stress concentrations. The failure theories considered include interactive failure theories, physically based failure criteria, damage mechanics, industrial and standard design code approaches as well as commercial software vendors and developers (Hinton, et al., 2004b). The predictions from theories were compared to experimental results as presented in (Hinton, et al., 2004a). The second World-Wide Failure Exercise (WWFE-II) focused on the response of laminated fiber-reinforced composites under three-dimensional stress condition (Hinton & Kaddour, 2012). Twelve groups took part and ranking of the participating theories were made. Kaddour and Hinton (2013) noted that “The designers, wishing to use the models benchmarked in WWFE-II, can only expect a few theories to give acceptable correlation (within 50%) with test data for 75% of the test cases used”. The comparison between the various theories was presented in (Kaddour & Hinton, 2013). The third world-wide failure exercise (WWFE-III) focuses on modeling sub-critical damage under in-plane loading, especially continuum damage mechanics (CDM) and fracture mechanics approaches (Kaddour, et al., 2013). From the three exercises, Kaddour and Hinton (2018) noted that “…none of the theories was capable of predicting all the strength and deformation of the lamina and laminates within ±10% of the measured data”.

Some of the earliest and widely used failure criteria are the maximum stress and maximum strain failure criteria for orthotropic materials. In these criteria, failure occurs when the stress components in material directions exceeds the strength or ultimate strain in that direction. Because of their simplicity, they have been implemented in commercial finite element codes (Barbero, 2013; ANSYS-LST, 2020) for use by design engineers. By considering each material direction separately, the interaction between different stress or strain components (Li & Sitnikova, 2018) are not accounted for. A truncated form of maximum strain failure criterion was proposed by Hart Smith (Hart-Smith, 1998).

Azzi and Tsai (1965) proposed a failure criterion based on Hill’s theory for yielding and plastic flow of anisotropic metals (Talreja, 2014). The proposed failure criterion considers three failure modes – tension or compression failure in the longitudinal direction, tension or compression failure in the transverse direction, and in-plane shear failure. It assumes transverse isotropy and considers only linear response of the material in longitudinal and transverse directions as well as in-plane shear (Talreja, 2014). Tsai and Wu (1971) proposed an interactive failure criterion derived from a quadratic yield criterion for orthotropic ductile materials. This criterion uses a single polynomial equation to predict failure in a laminae under general loading. The equation representating failure of unidirectional composite as proposed by Tsai-Wu (1971) describes an ellipsoid in in-plane stress space. Talreja (2014) noted that "… the ellipsoidal representation of the strength of thin sheets of unidirectional composites in the in-plane stress components is only a postulate that is not motivated or supported by any physical consideration of the failure mechanisms".

Hashin (1980) proposed three-dimensional failure criteria which considers four failure modes – tensile fiber mode, compressive fiber mode, tensile matrix mode, and compressive matrix mode. This criteria assumes quadratic interaction between stresses on the plane of fracture and requires piecewise smooth surfaces with each branch representing one failure mode. This assumption is based on logical reasoning rather than micromechanical observations (Pinho, et al., 2005). Hashin's theory, however, does not always fit experimental results from transverse compression owing to the fact that it does not account for the effect of in-plane shear on compressive strength (Pinho, et al., 2005).

Puck's failure theory (Deuschle & Kröplin, 2012) is based on physical considerations proposed by Hashin (1980). This criteria distingushes two failure modes that are independent – fiber failure and inter-fiber failure. The fracture condition is formulated on an action-plane or failure plane, and the tractions on that plane as well the inclination angle of the plane constitutes the variables. Puck and Schürmann (1998) proposed a procedure for evaluating the angle of inclination of the failure plane and the critical tractions on that plane. The limitations of Puck failure criterion are that it is valid only for transverse isotropic material at lamina level, the master fracture body is not a closed envelope (Kaddour & Hinton, 2013), and the failure criterion is not function of rate and temperature (Shyamsunder, et al., 2021).

The classical failure criteria presented above do not take account of the microstructure of the composite in failure predictions. They use homogenized properties to make predictions at the lamina level (macroscale). The microstructure of composites is, however, responsible, to a large extent, for the complexity of failure mechanisms in any composite architecture.

Micromechanical Modeling for Failure Prediction

Virtual testing by means of micromechanics which relies on Representative Volume Elements (RVE) and Repeated Unit Cells (RUC) is commonly used for predicting deformation, damage and failure at the constituent level (Harrington, et al., 2017; Khaled, et al., 2021; Vaughan & McCarthy, 2011; Canal, et al., 2009; Romanowicz, 2012; Totry, et al., 2008a; Totry, et al., 2008b; Vogler, et al., 2000; Naya, et al., 2017; Vajari, 2015).

Totry et al. (2008b) used computational micromechanics by generating RVE with random fiber arrangement to simulate the response of carbon fiber reinforce composites under transverse compression and out-of-plane shear. The generated failure surface was compared to Hashin, Puck and LaRC (Davila, et al., 2005) failure criteria. It was concluded that the failure locus generated through computational micromechanical simulations was in excellent agreement with experimental results and the transition from shear to compression-dominated fracture was adequately predicted. Sun et al. (2019) generated failure data through biaxial testing in the transverse tension/compression and in-plane, transverse tension/compression and out-of-plane shear, and longitudinal tension/compression and in-plane shear while accounting for initial fiber misalignment in an RVE. The generated data was compared to existing classical failure criteria, namely Puck, Tsai-Wu, Hashin, Pinho-LaRC04 (Pinho, et al., 2006; Pinho, et al., 2005) and NU-Daniel (Daniel, et al., 2018) failure. It was found that all classical failure criteria gave different predictions from that of computational micromechanical models in the combined transverse compression and in-plane shear, and combined transverse compression and out-of-plane shear especially with the presence of high shear stress (Sun, et al., 2019). The failure envelopes obtained from computational micromechanics and the observed failure mechanisms were used to propose a new set of homogenized failure criteria based on NU-Daniel failure theory (Sun, et al., 2019). Romanowicz (2012) used repeating unit cells in hexagonal packing made of fiber, matrix and an interface to generate a failure locus under biaxial longitudinal tension and transverse compression. The prediction was compared to Puck failure criterion. It was concluded that the results from numerical homogenization agreed better with experimental results than Puck failure criterion (Romanowicz, 2012).

Harrington, et al. (2017) conducted analytical and FE-based virtual tests on unidirectional composites considering the fiber and matrix phase in the simulation. The analytical approach used the generalized method of cells (Aboudi, 2004). The finite element-based Virtual Testing Software System (VTSS) (Harrington, 2015) is used to obtain homogenized stress-strain curves. The deformation analysis was carried out on the composite and the generated homogenized stress-strain curves were used as a part of the constitutive orthotropic material model for fiber-reinforced polymer composites. In a follow up work, the material properties of the F3900 epoxy resin matrix were characterized using experimental testing (Robbins (2019)) and subsequently used, in combination with fiber T800S[1] properties, to predict failure of T800S/F3900 unidirectional composite subjected to in-plane uniaxial loading (longitudinal tension and compression, transverse tension and compression as well as in-plane shear) (Parakhiya, 2020). Khaled, et al. (2021) extended the develop VTSS framework using a combination of experimental and computational mesoscale modeling technique with FE models that include fiber and matrix phases for generating failure data. This work forms the foundation of the current research study.

1.2. THESIS OBJECTIVES

An orthotropic elasto-plastic damage material model (OEPDMM) suitable for impact analysis of composite materials has been developed through a joint research project funded by the Federal Aviation Administration (FAA) and the National Aeronautics and Space Administration (NASA) (Goldberg, et al., 2016; Hoffarth, et al., 2016; Hoffarth, et al., 2017; Harrington, et al., 2017; Khaled, et al., 2018; Shyamsunder, et al., 2020; Shyamsunder, et al., 2021). In the recent continuing work (Robbins, 2019; Parakhiya, 2020; Khaled, et al., 2021), a framework for predicting failure in composites

[1] https://www.toraycma.com/page.php?id=661

using virtual testing was developed. The framework uses a multiscale modeling approach where the constituents, fiber and matrix, are modeled to conduct virtual tests for failure prediction. The strength of the virtual test framework (Harrington, 2015; Khaled, et al., 2021) lie in showing the significance of the of the composite architecture and in explaining the deficiency of macro-scale (homogenized) models that are deficient in predicting damage and failure. It provides a means of obtaining experimental data for macroscale models if experimental test cannot be conducted reliably (Khaled, et al., 2021). Moreover, it provides data for point cloud data generation that represent failure surface when analytical expressions are not available or possible.

The study presented in this thesis focuses on generating failure data for T800S/F3900 unidirectional composite under uniaxial and biaxial loadings. Classical failure criteria developed by researchers use smooth or piecewise smooth curve to approximate the failure envelope due to insufficient experimental data for failure characterization. This study presents failure data that could be used in a tabulated or a point cloud failure surface making no approximations regarding the nature of the failure surface. The composite is modeled at the constituent level using repeating unit cell (RUC) in a square packing. Three-dimensional (3D) finite element models for in-plane tests are generated from experimental specimens and validated against experimental data. For out-of-plane tests, two-dimensional (2D) plane strain models are generated through a square packing of repeating unit cells in the transverse plane of the composite. The generated 2D models are examined for the effect of the size of the RUC, mesh sensitivity and effect of the gauge section on the response, and then validated against experimental results. Biaxial tests are carried out to generate failure data which is compared to classical failure criteria.

Following the background of the research and the thesis objective, Chapter 2 presents Puck and Tsai-Wu failure criteria with the relevant analytical expressions that define the failure surface summarized. Next, the Point Cloud Failure Criteria is introduced. In Chapter 3, the material models used for the fiber and the matrix are described and the calibration of the failure parameters in the matrix is discussed. Subsequently, in Chapter 4, the generation of finite element models for the in-plane and out-of-plane tests is explained and the models are validated against available experimental data. In Chapter 5, the biaxial test results are discussed, failure surfaces are plotted and compared against existing classical failure criteria. Finally, the results of the study are summarized in Chapter 6 along with the planned future work.

2. FAILURE CRITERIA IN OEPDMM

Failure in composites remains one of the challenging behaviors to predict due to its complexity. Various failure criteria have been proposed for many years. Among them, there are phenomenological failure criteria such as Puck Failure Criterion (PFC) (Puck & Schürmann, 1998) and interactive failure criteria such as Tsai-Wu Failure Criterion (TWFC) (Tsai & Wu, 1971). Both Puck and Tsai-Wu failure criteria have been implemented as Orthotropic Elasto-Plastic Damage Material Model (OEPDMM) as an integral part of ANSYS-LST commercial finite element software (ANSYS-LST, 2020). A new failure criterion known as Point Cloud Failure Criterion (PCFC) is being developed to complement and provide an alternative to the existing failure models in MAT_213 (OEPDMM). In this chapter, the details of the PFC and TWFC are presented followed by an introduction to PCFC.

2.1. PUCK FAILURE CRITERION

PFC is an action-plane-based model for transversely isotropic unidirectional fiber-reinforced composite lamina (Shyamsunder, et al., 2020). The action plane refers to the plane resisting the applied force. Puck and Schürmann (1998) distinguished two independent fracture criteria that are applied simultaneously, namely the fiber failure (FF) and inter-fiber failure (IFF). In the following sections, the analytical expressions for Puck failure criteria in various stress spaces of interest are discussed.

2.1.1. FAILURE SURFACE IN THE $\sigma_1 - \sigma_2$ SPACE

The main failure modes in the $\sigma_1 - \sigma_2$ stress space are the fiber failure (FF) and inter-fiber failure (IFF). The fundamental hypothesis for fiber failure is that it occurs in a unidirectional composite under combined state of stress (σ_1 , σ_2 , σ_3 , τ_{23} , τ_{31} , τ_{21}) at the same fiber stress as that acting in the fibers under uniaxial longitudinal loading (Puck & Schürmann, 1998). The “stress magnification effect” produced by the difference in moduli between the fiber and the matrix, leading to slightly higher stress in the fiber than the matrix, is accounted for by a stress magnification factor. This leads to fiber failure equation 2.1 for the longitudinal tension loading and equation 2.2 for longitudinal compression loading. In transverse load dominated failure modes (inter-fiber failure), the maximum stress failure criterion is applied to predict the failure strength as shown in equation 2.3 for tension and 2.4 for compression. This does not account for the degradation of inter-fiber fracture resistance due to single fiber failure. The local damage in the vicinity of single fiber breaks, which includes debonding between the fiber and the matrix as well as matrix microcracks, causes a decrease in fracture resistance (Puck & Schürmann, 1998). Experimentally determined values that express the degradation of the fracture resistances induced by single fiber breaks at high values of longitudinal stress could not be obtained for the composites studied in this thesis. The failure surface is shown in figure 2.1.

$$\frac{\sigma_1}{X_T} - \nu_{12}\frac{\sigma_2}{X_T} + \nu_{f12}\frac{E_1}{E_{f1}} m_{f\sigma}\frac{\sigma_2}{X_T} = 1 \quad (2.1)$$

$$\frac{\sigma_1}{X_C} - \nu_{12}\frac{\sigma_2}{X_C} + \nu_{f12}\frac{E_1}{E_{f1}} m_{f\sigma}\frac{\sigma_2}{X_C} = 1 \quad (2.2)$$

$$\frac{\sigma_2}{Y_T} = 1 \quad (2.3)$$

$$\frac{\sigma_2}{Y_C} = 1 \quad (2.4)$$

where

σ_1 , σ_2 are normal stresses in a unidirectional layer,

X_T , X_C are the tensile and compressive strength of the unidirectional layer parallel to the fiber direction, respectively,

Y_T , Y_C are the tensile and compressive strength of the unidirectional layer transverse to the fiber direction, respectively,

ν_{12} is the Poisson's ratio of the composite in the 1-2 plane,

$m_{f\sigma}$ is the mean stress magnification factor for the fibers in the 2-direction due to difference between the transverse modulus of the fiber and the modulus of the matrix,

ν_{f12} is the Poisson's ratio of the fiber in the 1-2 plane,

E_{f1} is the fiber modulus in the 1-direction, and

E_1 is the elastic modulus of the unidirectional layer in the 1-direction.

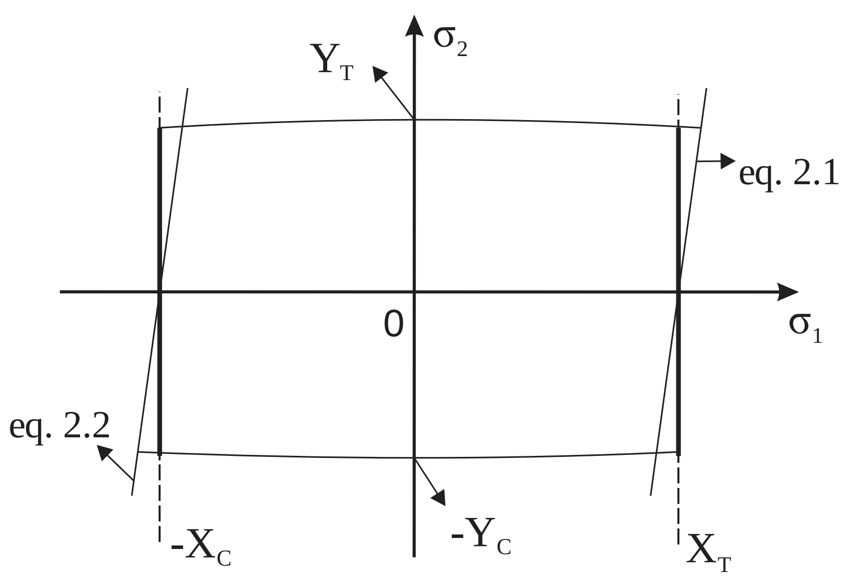

Figure 2.1. Puck failure criteria fracture curve in the $\sigma_1 - \sigma_2$ stress space

2.1.2. FAILURE SURFACE IN THE $\sigma_2 - \tau_{21}$ SPACE

In Puck's failure criterion, inter-fiber failure mode dominates the $\sigma_2 - \tau_{21}$ stress space. The stresses on the action plane (i.e. the plane resisting the applied force) parallel to fibers consist of a normal stress σ_n and two shear stress components τ_{n1} and τ_{nt} (figure 2.2), namely the transverse-longitudinal shear stress and the transverse-transverse shear stress respectively (Puck & Schürmann, 1998). In the case of transverse normal stress in tension, the stress on the action plane is equal to the transverse strength in tension $\sigma_n = \sigma_2$. This means, the fracture resistance on the action plane $R_{\perp}^{(+)A}$ equals the transverse tensile strength $R_{\perp}^{(+)}$. Similarly, in the case of in-plane shear (referred to as transverse-longitudinal shear), the shear fracture resistance on the action plane $R_{\perp\|}^{A}$ equals the in-plane shear strength $R_{\perp\|}$. The failure surface equation then derived for the case of transverse tensile stress and in-plane shear is given in equation 2.5 and represents fracture Mode A (Puck & Schürmann, 1998). The failure surface equation for fracture mode B, which is in-plane shear dominated mode, is given in equation 2.6. Fracture mode C, the compression dominated failure, is given in equation 2.7. Figure 2.3 shows the fracture (failure) envelope in the $\sigma_2 - \tau_{21}$ stress space as derived in (Puck & Schürmann, 1998).

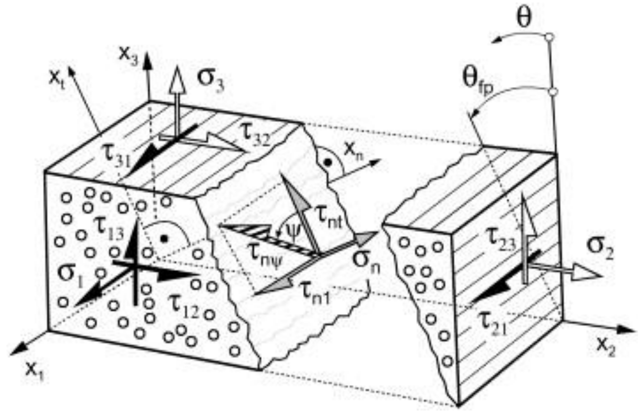

Figure 2.2. Stresses acting on the action plane (Puck, et al., 2002)

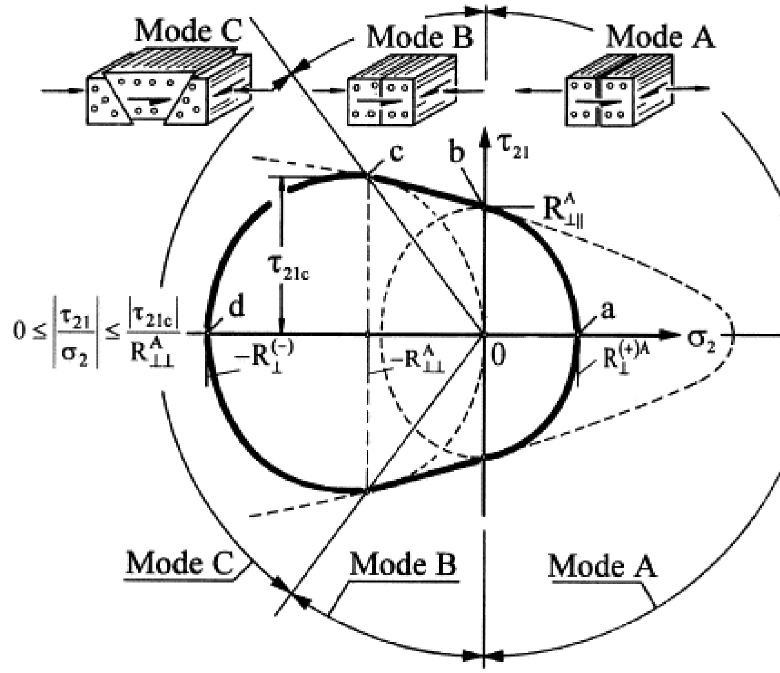

Figure 2.3. Puck failure criterion fracture curve in the stress space (Puck & Schürmann, 1998)

$$\left(\frac{\tau_{21}}{R_{\perp\parallel}}\right)^2 + \left(1 - p_{\perp\parallel}^{(+)}\frac{R_\perp^{(+)}}{R_{\perp\parallel}}\right)^2 \left(\frac{\sigma_2}{R_\perp^{(+)}}\right)^2 = \left(1 - p_{\perp\parallel}^{(+)}\frac{\sigma_2}{R_{\perp\parallel}}\right)^2 \text{ for } \sigma_2 \ge 0 \qquad (2.5)$$

$$\tau_{21}{}^2 + \left(p_{\perp\parallel}^{(-)}\sigma_2\right)^2 = \left(R_{\perp\parallel} - p_{\perp\parallel}^{(-)}\sigma_2\right)^2 \text{ for } \sigma_2 \le 0 \text{ mode B} \qquad (2.6)$$

$$\left(\frac{\tau_{21}}{2(1+p_{\perp\perp}^{(-)})R_{\perp\parallel}}\right)^2=\left[1+\left(\frac{\sigma_2}{R_{\perp}^{(-)}}\right)^2\frac{R_{\perp}^{(-)}}{\sigma_2}\right]\frac{-\sigma_2}{R_{\perp}^{(-)}} \text{ for } \sigma_2\leq 0 \text{ mode C} \tag{2.7}$$

where

τ_{21} is the shear stress in the unidirectional layer in the 1-2 plane,

$R_{\perp\parallel}$ is the fracture resistance if the stress action plane against its fracture due to transverse/parallel shear stressing,

$R_{\perp}^{(+)}$ is the fracture resistance if the stress action plane against its fracture due to transverse tensile stressing,

$R_{\perp}^{(-)}$ is the fracture resistance if the stress action plane against its fracture due to transverse compressive stressing,

$p_{\perp\parallel}^{(+)}$ is the slope of the (σ_n, τ_{n1}) fracture envelope for $\sigma_n \geq 0$ at $\sigma_n = 0$,

$p_{\perp\parallel}^{(-)}$ is the slope of the (σ_n, τ_{n1}) fracture envelope for $\sigma_n \leq 0$ at $\sigma_n = 0$,

$p_{\perp\perp}^{(-)}$ is the slope of the (σ_n, τ_{nt}) fracture envelope for $\sigma_n \leq 0$ at $\sigma_n = 0$

The fracture resistances $R_{\perp\parallel}$, $R_{\perp}^{(+)}$ and $R_{\perp}^{(-)}$ are obtained from experimentally obtained data (Khaled, et al., 2018) as described in (Puck, et al., 2002). The value of the slopes $p_{\perp\parallel}^{(+)}$, $p_{\perp\parallel}^{(-)}$ and $p_{\perp\perp}^{(-)}$ are determined as explained in (Puck, et al., 2002).

2.1.3. FAILURE SURFACE IN THE $\sigma_2 - \sigma_3$ SPACE

The failure surface in the $\sigma_2 - \sigma_3$ stress space is made of two parts – one is the ellipse part of the master fracture curve transferred into the $\sigma_2 - \sigma_3$ space for $\sigma_n > 0$ (the normal stress of the action plane is tensile) and the other is a parabola part for $\sigma_n \leq 0$. The derivation of the failure surface equations can be found in (Puck & Deuschle, 2013).

The equation for the ellipse part (equation 2.8) below and that of the parabola part (equation 2.9) and the fracture envelope for this stress space is shown in figure 2.4.

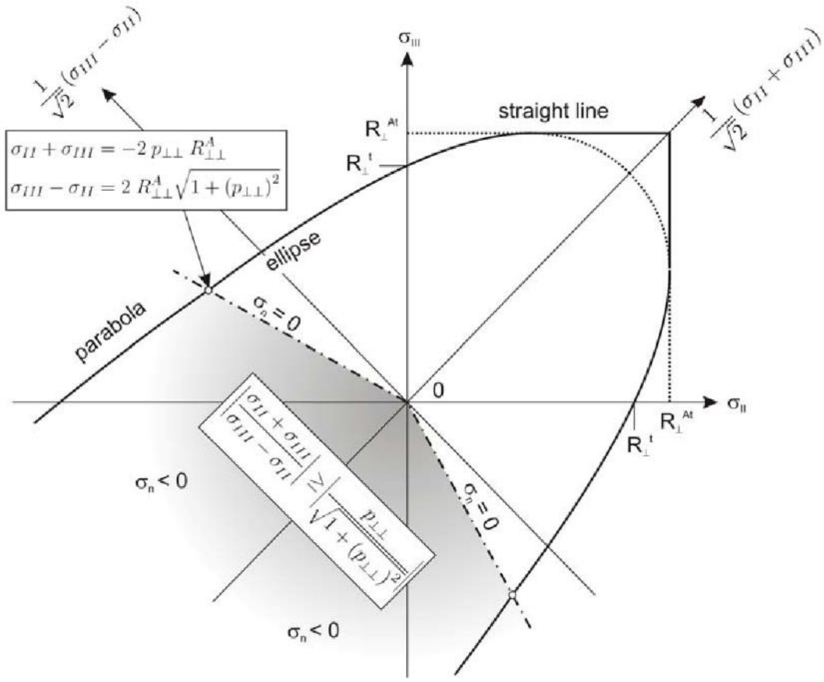

Figure 2.4. Puck failure criterion fracture (failure) envelope in the $\sigma_2 - \sigma_3$ space (Puck & Deuschle, 2013)

$$\frac{1}{4}\left(\sigma_3 - \sigma_2\right)^2 = \left(R_{\perp\perp}^{A}\right)^2 \left[1 - \frac{\left(p_{\perp\perp}\right)^2}{1 - C_2}\right] - \frac{p_{\perp\perp} R_{\perp\perp}^{A}}{1 - C_2}\left(\sigma_3 + \sigma_2\right) - \left[1 - \frac{C_2}{4\left(1 - C_2\right)}\right]\left(\sigma_3 + \sigma_2\right)^2 \qquad (2.8)$$

$$\frac{1}{4}\left(\sigma_3 - \sigma_2\right)^2 = \left(R_{\perp\perp}^{A}\right)^2 \left[1 - \left(p_{\perp\perp}\right)^2\right] - p_{\perp\perp} R_{\perp\perp}^{A}\left(\sigma_3 + \sigma_2\right) \qquad (2.9)$$

$$C_2 = \left(\frac{R_{\perp\perp}^{A}}{R_{\perp}^{At}}\right)^2 - 2\, p_{\perp\perp} \frac{R_{\perp\perp}^{A}}{R_{\perp}^{At}} \qquad (2.10)$$

$$p_{\perp\perp}^{(-)} = \frac{1}{2}\left(\sqrt{1 + 2\, p_{\perp\parallel}^{(-)} \frac{R_{\perp}^{(-)}}{R_{\perp\parallel}}} - 1\right) \qquad (2.11)$$

$$R_{\perp\perp}^{A} = \frac{R_{\perp}^{(-)}}{2\left(1 + p_{\perp\perp}^{(-)}\right)} \qquad (2.12)$$

where $R_{\perp\perp}^{A}$ is the fracture resistance of the action plane against its fracture due to transverse/transverse shear, i.e., shear stress in the 2-3 plane.

2.1.4. FAILURE SURFACE IN THE $\sigma_2 - \tau_{23}$ SPACE

The basis for the analytical approach in this stress space is formed from Mohr's and Coulomb's ideas. The master fracture curve, also known as fracture envelope (Puck & Deuschle, 2013) for the $\sigma_2 - \tau_{23}$ stress space is made of a parabolic part for $\sigma_n \leq 0$ whose analytical expression is shown in equation 2.13, and an ellipse part for $\sigma_n \geq 0$ whose analytical expression is in equation 2.14. These equations are combined with the Mohr's stress circle to complete the master fracture curve, which is the failure surface in the context of this thesis. The fracture surface, as produced by Puck & Deuschle (2013) in the $\sigma_2 - \tau_{23}$ space, is shown in figure 2.5. It is assumed here that in pure transverse shear loading, the shear stress on the fracture plane τ_{nt} is equal to the shear stress τ_{23}, and under uniaxial transverse tension load, the normal stress on the fracture surface σ_n is equal to σ_2.

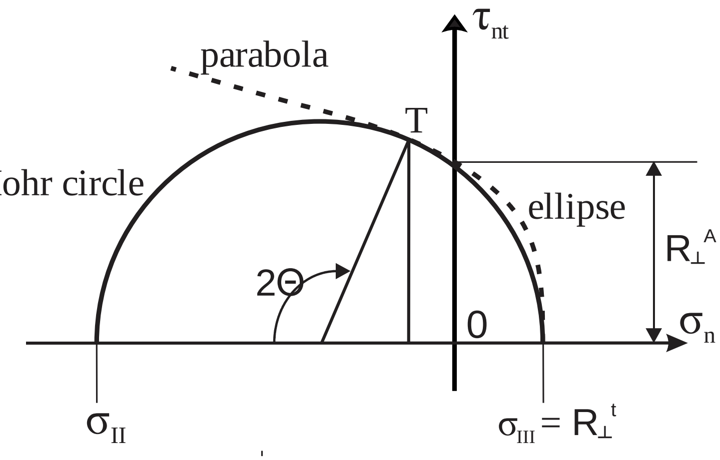

Figure 2.5. Puck failure criterion fracture envelope in the $\sigma_2 - \tau_{23}$ space (Puck & Deuschle, 2013)

$$\left(\tau_{23}\right)^2 = \left(R_{\perp\perp}^A\right)^2 - 2p_{\perp\perp}^{(-)}R_{\perp\perp}^A\sigma_2 \text{ for } \sigma_2 \le 0 \tag{2.13}$$

$$\left(\tau_{23}\right)^2 = \left(R_{\perp\perp}^A\right)^2 - 2p_{\perp\perp}^{(-)}R_{\perp\perp}^A\sigma_2 - \left[\left(\frac{R_{\perp\perp}^A}{R_{\perp}^{At}}\right)^2 - 2p_{\perp\perp}^{(-)}\frac{R_{\perp\perp}^A}{R_{\perp}^{At}}\right]\sigma_2^2 \text{ for } \sigma_2 \ge 0$$

(2.14)

2.2. TSAI-WU FAILURE CRITERION

Tsai-Wu failure criterion is one of the most commonly used failure criteria for modeling failure in composite. In its general form, assuming transverse isotropy in the composite, Tsai-Wu failure criterion is given as shown in equation 2.15.

$$\begin{aligned} F &= F_{11}\sigma_1^2 + F_{22}\left(\sigma_2^2+\sigma_3^2\right) + \left(2F_{22}-F_{44}\right)\sigma_2\sigma_3 + 2F_{12}\sigma_1\left(\sigma_2+\sigma_3\right) + F_1\left(\sigma_1+\sigma_2\right) \\ &+F_2\sigma_3 + F_{44}\tau_{23}^2 + F_{66}\left(\tau_{13}^2+\tau_{23}^2\right) \end{aligned} \tag{2.15}$$

where

$$F_1 = \frac{1}{X_T} - \frac{1}{X_C} \qquad F_2 = \frac{1}{Y_T} - \frac{1}{Y_C} \qquad F_{11} = \frac{1}{X_T X_C} \qquad F_{22} = \frac{1}{Y_T Y_C} \qquad F_{12} = -\sqrt{F_{11}F_{22}}$$

$$F_{66} = \frac{1}{S_{21}} \qquad F_{44} = \frac{1}{S_{23}^2}$$

σ_1, σ_2, σ_3, τ_{23}, τ_{13}, τ_{12} are normal and shear stresses,

X_T, X_C are the tensile and compressive strength of the unidirectional layer parallel to the fiber direction respectively,

Y_T, Y_C are the tensile and compressive strength of the unidirectional layer transverse to the fiber direction respectively,

S_{21} is the shear strength of a unidirectional layer transverse and parallel to the fiber i.e., in the 1-2 plane, and

S_{23} is the shear strength of a unidirectional layer transverse to the fiber i.e. in the 2-3 plane.

In the following sections, the analytical expression used for forming the failure surface is presented along with the definition of the input parameters.

2.2.1. FAILURE SURFACE IN THE $\sigma_1 - \sigma_2$ SPACE

In the $\sigma_1 - \sigma_2$ stress space, only longitudinal and transverse normal stresses are non-zero and all other stress components are eliminated from the equation. The simplified equation for this space is shown in equation 2.16 where only the normal stresses in the 1- and 2-directions are non-zero. It represents an equation of an ellipse. The failure surface driven by T800/F3900 composite is shown in figure 2.6. The input parameters used to plot the surface are found in table 5.2 (refer to Chapter 5).

$$F_{11}\sigma_1^2 + F_{22}\sigma_2^2 + 2F_{12}\sigma_1\sigma_2 + F_1\sigma_1 + F_2\sigma_2 = 1 \qquad (2.16)$$

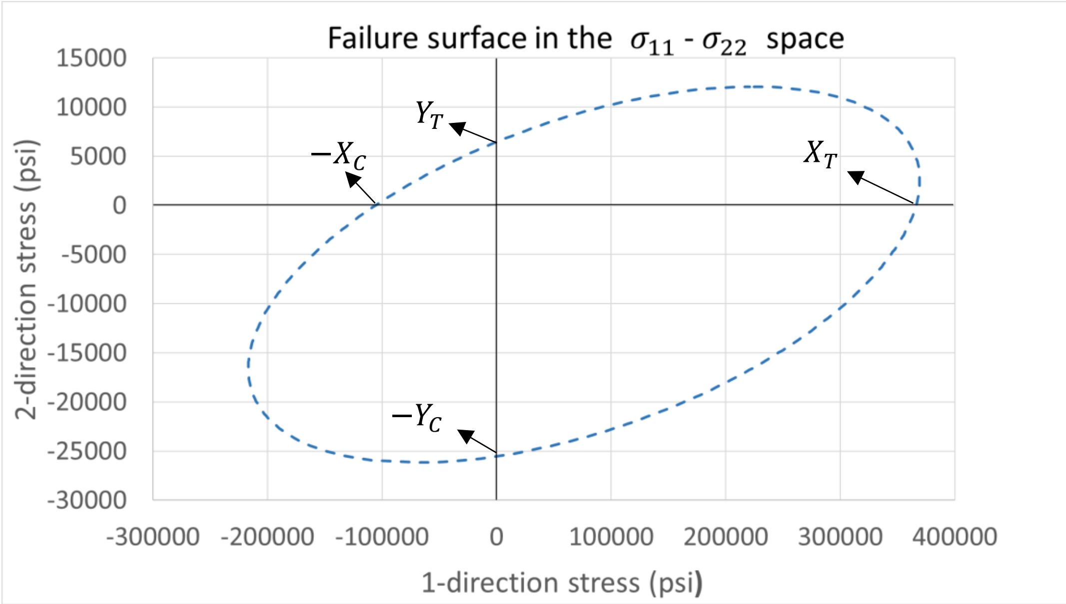

Figure 2.6. Tsai-Wu failure surface in the $\sigma_1 - \sigma_2$ stress space driven by T800S/F3900 composite failure data ($X_T = 366097\,psi$, $X_C = 105766\,psi$, $Y_T = 6471\,psi$, $Y_C = 25530\,psi$)

2.2.2. FAILURE SURFACE IN THE $\sigma_2 - \tau_{21}$ SPACE

In the $\sigma_2 - \tau_{21}$ stress space, the failure surface forms an ellipse whose analytical expression is shown in equation 2.17.

$$F_{22}\sigma_2^2 + F_2\sigma_2 + F_{66}\tau_{21}^2 = 1 \tag{2.17}$$

2.2.3. FAILURE SURFACE IN THE $\sigma_2 - \sigma_3$ SPACE

The failure surface in the $\sigma_2 - \sigma_3$ stress space not only depends on normal strength but also depends on the shear strength on the 2-3 plane. The analytical expression in equation 2.18 has a term, F_{44} , which depends on the 2-3 plane shear strength. The failure surface in the $\sigma_2 - \sigma_3$ has a shape of a parabola. Thus, it is an open surface implying that the material does not fail under biaxial compression loading (Li, et al., 2017). The failure surface in the $\sigma_2 - \sigma_3$ space driven by T800/F3900 data in figure 2.7 is open in the biaxial transverse compression quadrant.

$$F_{22}\left(\sigma_2^2+\sigma_3^2\right)+\left(2F_{22}-F_{44}\right)\sigma_2\sigma_3+F_2\sigma_2+F_3\sigma_3=1 \tag{2.18}$$

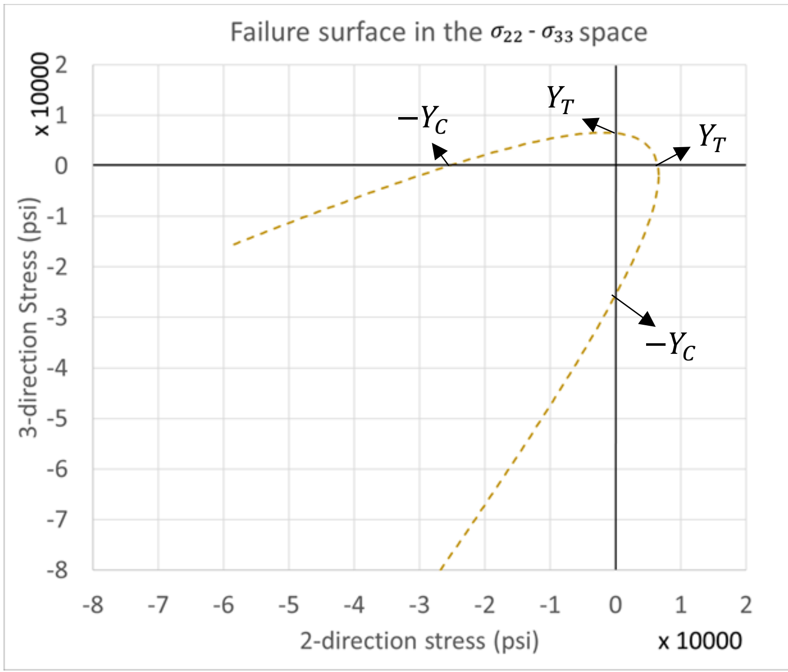

Figure 2.7. Tsai-Wu failure surface in the $\sigma_2 - \sigma_3$ stress space driven by T800S/F3900 composite failure data ($Y_T = 6471 psi$, $Y_C = 25530 psi$)

2.2.4. FAILURE SURFACE IN THE $\sigma_2 - \tau_{23}$ SPACE

Finally, the failure surface in the $\sigma_2 - \tau_{23}$ stress space, where only the transverse normal and 2-3 plane shear components are non-zero and is shown in equation 2.19.

$$F_{22}\sigma_2^2+F_2\sigma_2+F_{44}\tau_{23}^2=1 \tag{2.19}$$

2.3. POINT CLOUD FAILURE CRITERION

The Point Cloud Failure Criterion relies on point cloud data of the failure surface for failure prediction (Rajan, et al., 2021). Once the points on the failure surface are generated, the Approximate Nearest Neighbor Method (ANN) (Arya & Mount, 1993; Mount, 2010) is used to determine k-nearest neighbors to a query point from which it can be ascertained if a given stress tensor computed at a finite element stress Gauss point is inside or outside the point cloud representing the failure surface.

A set of points P in a *d*-dimensional space is the input to the ANN method. The input data is preprocessed into a data structure such that when given a query, it can be reported efficiently (Mount, 2010), i.e., whether the query point is inside or outside of the *d*-dimensional point cloud surface can be computed efficiently. Figure 2.1 shows the representation of the point cloud where the k-nearest neighbors are identified once the query point is specified.

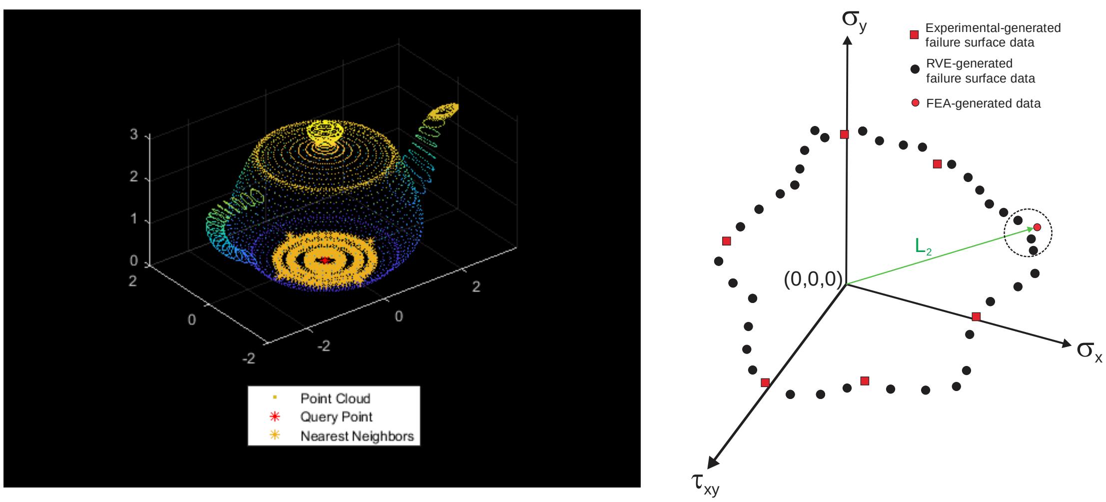

(a) (b)

Figure 2.1. (a) Finding k-nearest neighbors in a point cloud[2] (b) Failure surface and k-nearest neighbors in the stress-based point cloud.

In the context of failure prediction using virtual tests or experiments, the *d*-dimensional point cloud is made of failure points obtained from uniaxial and multiaxial tests. The query point represents state of stress or strain at Gauss points in a finite element. In a stress-based failure surface data, a three-dimensional ($d = 3$), four-dimensional ($d = 4$) and six-dimensional ($d = 6$) point clouds are obtained from a plane stress, plane strain and full three-dimensional state of stress, respectively. Once the point cloud failure surface has been generated, the nearest neighbors to the finite element (FE) generated Gauss point can be found and the question of whether the FE-generated point is inside or outside the point cloud failure surface can be answered (Rajan, et al., 2021).

Given general norm, L_r,

[2] https://www.mathworks.com/help/vision/ref/pointcloud.findnearestneighbors.html

$$L_r = \left(\sqrt{\sum_{i=1}^{d} |v_i|^r} \right) \tag{2.19}$$

where

d is the dimension of the space

v is the vector position of each point in the d-dimensional space,

the following conditions determine whether the point is inside or outside the surface-generated data (SGD) or point cloud. That is, the determination is made as

Outside: $L_2^{FEA} \geq L_2^{SGD} - \alpha\sigma_{range}$

Inside: $L_2^{FEA} < L_2^{SGD} - \alpha\sigma_{range}$

where

$\sigma_{range} = \sigma_{\max} - \sigma_{\min}$

$\alpha\sigma_{range}$ is the factor of safety in the prediction with $0 < \alpha < 1$

The implementation of the ANN library in a C++ computer program follows the steps described below (Rajan, et al., 2021).

Step 1: Specify P , d and the error bound ε .

Step 2: Data points are passed to the library to create the ANN data structure.

Step 3: Provide k (number of nearest neighbors).

Step 4: Specify the query point q as many times are required.

The accuracy (Mount, 2010) is function of a real-valued number $\varepsilon \geq 0$. If provided, the kth nearest neighbor is a (1+ε) approximation of the true kth nearest neighbor. If ε is omitted, then the nearest neighbors are computed accurately. The efficiency and accuracy of the ANN method depends on:

- The number of points in the failure surface.
- The distribution of the points in the search space so that sufficiently close points can be found during the search process.
- The accuracy, ε, with which the nearest neighbors are to be found.

Point cloud failure surface is generated in this thesis both in the three-dimensional (1-2 plane) and the four-dimensional (2-3 plane) stress/strain spaces.

3. MATERIAL MODELS DESCRIPTION

The T800-F3900 unidirectional composite shown in figure 3.1 is the focus of the numerical study. Toray describes T800S as an intermediate modulus, high tensile strength graphite fiber. The epoxy resin system is labeled F3900 where a toughened epoxy is combined with small elastomeric particles to form a compliant interface or interleaf between fiber plies to resist impact damage and delamination (Smith & Dow, 1991). The following should be noted about the finite element models used in the study – the carbon fibers are modeled with a circular cross-section and are assumed to be straight, and a perfect bonding between the fiber and the matrix is assumed so that modeling the fiber-matrix interface is not needed. Numerical studies carried out earlier (Parakhiya, 2020) showed that the numerical calibration of the interface modeled with cohesive zone finite elements, did not yield superior results. In addition, the laminate is modeled assuming no resin rich zone at the interface of adjacent lamina. In the first section, the fiber material model is developed. This is followed by experimental characterization of the matrix. Finally, the input data to the matrix material model is presented.

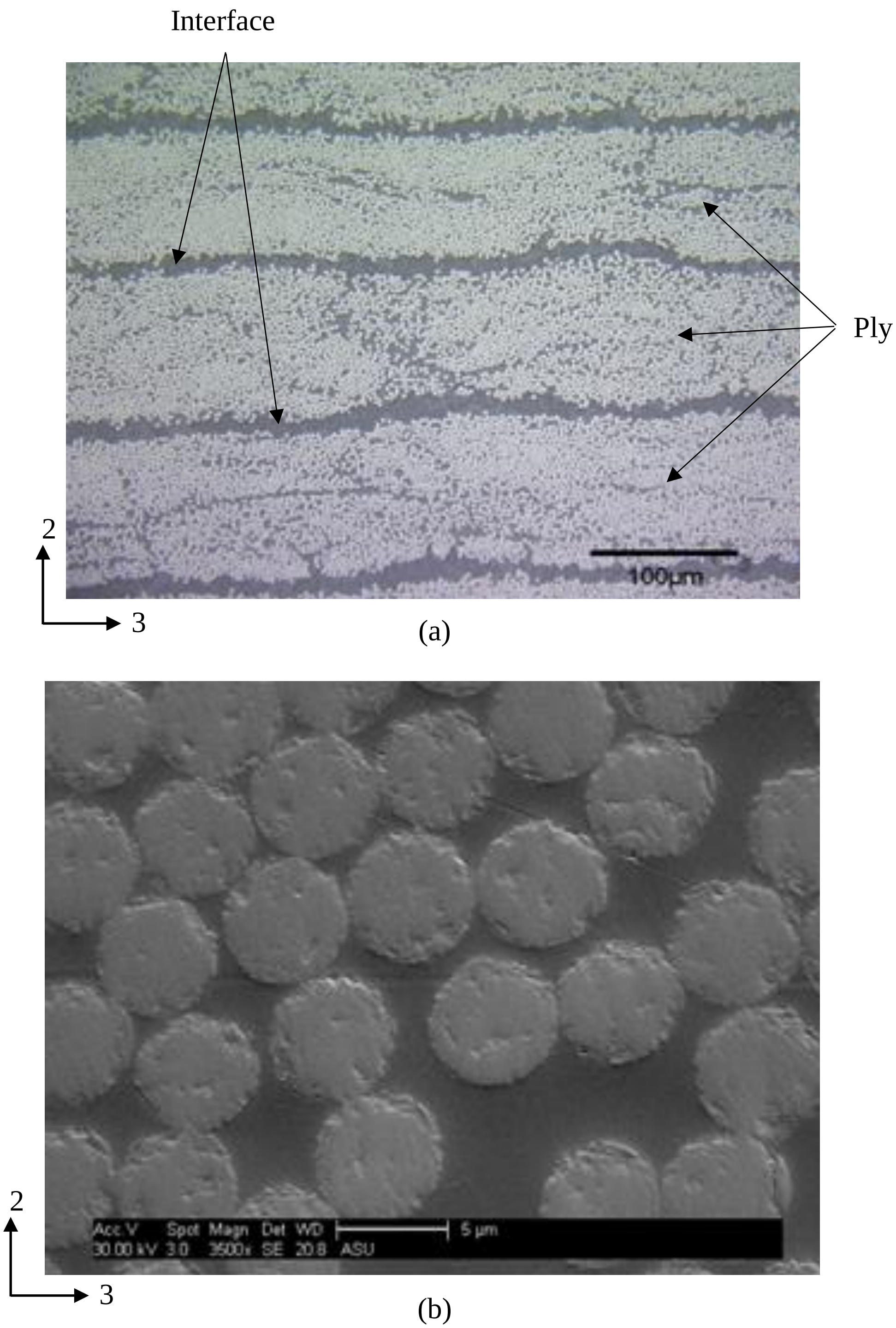

Figure 3.1. Cross-section of the T800/F3900 composite panel (a) optical micrograph image (b) SEM image (Holt, 2018)

3.1. MATERIAL MODEL FOR T800S FIBER

The fiber is modeled as a linear elastic, transversely isotropic material up to failure. In a three-dimensional model, fibers are modeled as cylinders of uniform cross-section (figure 3.2). No initial fiber misalignment is included in the model. The input for the fiber material model requires elastic moduli in the longitudinal and transverse directions as well as Poisson's ratios for the stress-strain response, and failure strain values. The fiber longitudinal tension elastic modulus (E_{11}^{T}) was obtained from manufacturer's datasheet[3] while longitudinal compression elastic modulus (E_{11}^{C}) was calibrated to match the stiffness from the 1-direction compression test (Khaled, et al., 2018). The in-situ longitudinal compression and tension moduli have been shown experimentally to be different (Herráez, et al., 2018). Tension/compression asymmetry is included in the material model. The transverse elastic modulus, longitudinal Poisson's ratio, and transverse Poisson's ratio were obtained from inverse analysis of the T800S/F3900 composite and from other carbon fibers with similar properties to T800S (Harrington, et al., 2017). The Micromechanics Analysis Code based on Generalized Method of Cells (Bednarcyk & Arnold, 2002) was used in inverse analysis to obtain the shear modulus from experimental results of T800S/F3900 composite (Raju & Acosta, 2010).

The experimental tests performed by Khaled et al. (2018) showed fiber failure only in the 1-direction tension and compression tests. In the 2-direction and 3-direction

[3] https://www.toraycma.com/page.php?id=661

tension and compression tests, inter-fiber (matrix) failure was observed to dominate the response. Therefore, only fiber failure along the 1-direction is considered. The previously referenced material model, MAT_213 is used to model the fiber. The Principal Strain Failure Criterion implemented in MAT_213 (version V1.3.4) was activated for modeling failure in the fiber. The principal strain at failure in tension was obtained from (Khaled, et al., 2021) while the principal strain at failure in compression was taken as the failure strain in the 1-direction compression test in (Khaled, et al., 2018). Table 3.2 summarizes the principal failure strains used.

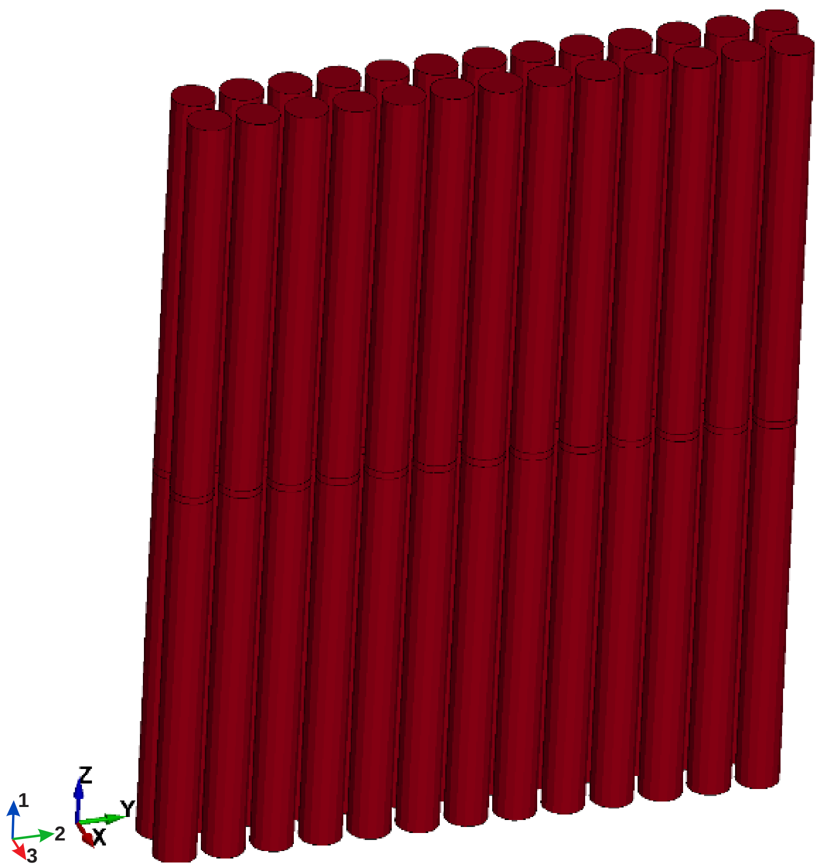

Figure 3.2. Fiber finite element model

Table 3.1. T800S material properties

Engineering Constant	Value	Source
E_{11}^{T}	$4(10^{7})\,psi$	Toray Datasheet
E_{11}^{C}	$3.1(10^{7})\,psi$	(Khaled, et al., 2021)
$E_{22} = E_{33}$	$2.25(10^{6})\,psi$	(Harrington, et al., 2017)
$\nu_{31} = \nu_{21}$	0.01125	(Harrington, et al., 2017)
ν_{23}	0.25	(Harrington, 2015)
$G_{22} = G_{13}$	$1.5(10^{7})\,psi$	(Harrington, et al., 2017)
G_{23}	$1.5(10^{7})\,psi$	(Harrington, et al., 2017)

Table 3.2. Failure strains for fiber used in MAT213

Principal material direction	Failure strain value
1-direction tension	0.02
1-direction compression	0.00629

In the two-dimensional (2D) model used for 2-3 plane loading where only transverse material properties are considered. No failure was activated in the fiber because the fibers are assumed to fail only in the longitudinal direction (1-direction). The fiber material model in this case is MAT_001 (ANSYS-LST, 2020) which is a linear elastic model with isotropic material properties. Detailed discussions on the finite element modeling are presented in Chapter 4.

3.2. MATERIAL MODEL FOR F3900 EPOXY RESIN

The highly toughened epoxy resin F3900 was modeled as an isotropic elasto-plastic material. The experimental characterization of the epoxy resin (Khaled, et al., 2021; Robbins, 2019) showed different behavior under tension, compression and shear with significant nonlinearity. The elastic material constants obtained from experimental characterization include the bulk, elastic and shear moduli as well as elastic Poisson's ratio as shown in table 3.3.

Table 3.3. Elastic properties for F3900 matrix

Material Constant	**Value**
Bulk Modulus	$6.02(10^5)$ psi
Shear Modulus	$1.47(10^5)$ psi
Elastic Modulus	$4.09(10^5)$ psi
Elastic Poisson's ratio	0.387

The material model implemented in LS-DYNA (ANSYS-LST, 2020) as MAT_187, a Semi Analytical Model for Polymers (SAMP) (Kolling, et al., 2005), is used to model the epoxy resin. A pressure dependent yield criterion, f, presented in equation 3.1 is implemented in the material model and requires stress versus plastic strain curves as inputs as

$$f = \sigma_{vm}^2 - A_0 - A_1 p - A_2 p^2 \leq 0 \tag{3.1}$$

where

$p = -\dfrac{\sigma_{xx} + \sigma_{yy} + \sigma_{zz}}{3}$ is the pressure,

$\sigma_{vm} = \sqrt{\dfrac{3}{2}\left[\left(\sigma_{xx} + p\right)^2 + \left(\sigma_{yy} + p\right)^2 + \left(\sigma_{zz} + p\right)^2 + 2\sigma_{xy}^2 + 2\sigma_{yz}^2 + 2\sigma_{zx}^2\right]}$ is the von-Mises stress,

$$A_0 = 3\sigma_s^2,\ A_1 = 9\sigma_s^2\left(\frac{\sigma_c - \sigma_t}{\sigma_c\sigma_t}\right) \text{ and } A_2 = 9\left(\frac{\sigma_c\sigma_t - 3\sigma_s^2}{\sigma_c\sigma_t}\right)$$

σ_t, σ_c and σ_s are stresses from stress-strain curves obtained from uniaxial tension, compression and shear tests on the epoxy resin respectively. Pressure dependence is explained by the fact that thermoplastics are compressible during plastic flow (Kolling, et al., 2005). The yield stress versus plastic strain curves from uniaxial tension (LCID-T), uniaxial compression (LCID-C) and pure shear (LCID-S) tests from experimental characterization of the epoxy resin (Robbins, 2019) are fed as tabulated input to model the yield behavior of the material. These are shown in figure 3.3(a), (b) and (c), respectively. The yield surface is taken to be like a Drucker-Prager cone in the principal stress space. The shape of the yield surface is shown in figure 3.4.

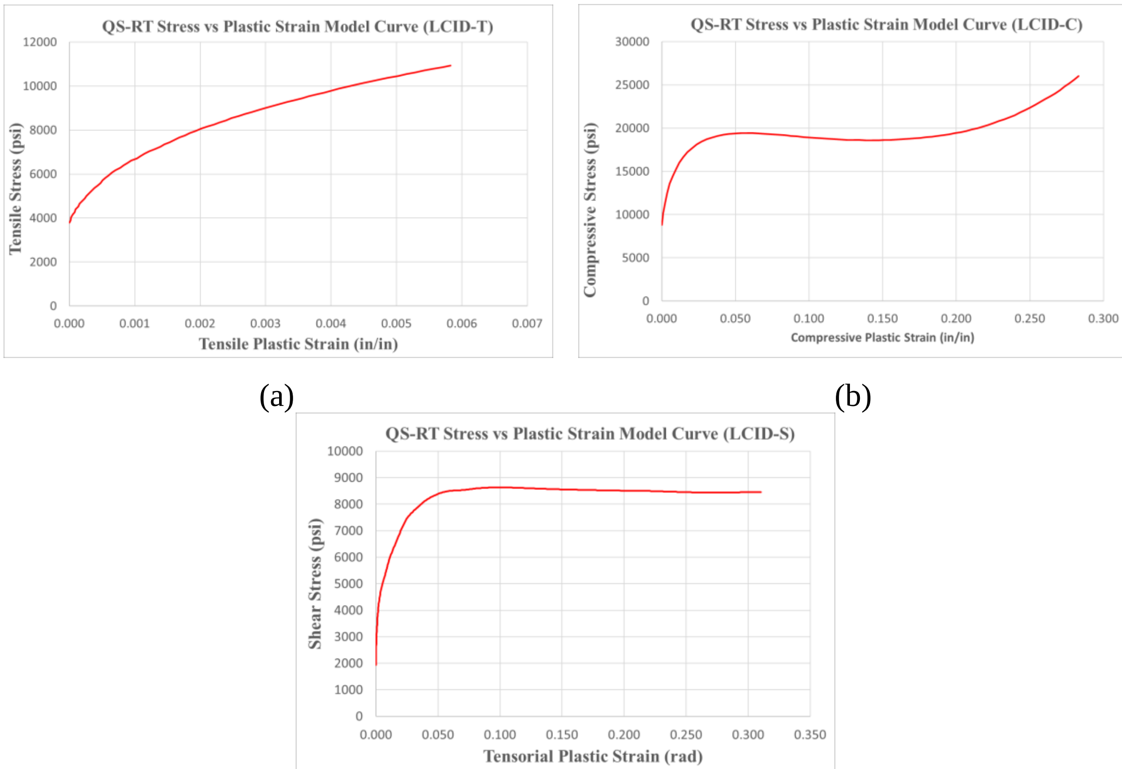

Figure 3.3. F3900 matrix material model input curves (a)LCID-T (b)LCID-C (c)LCID-S

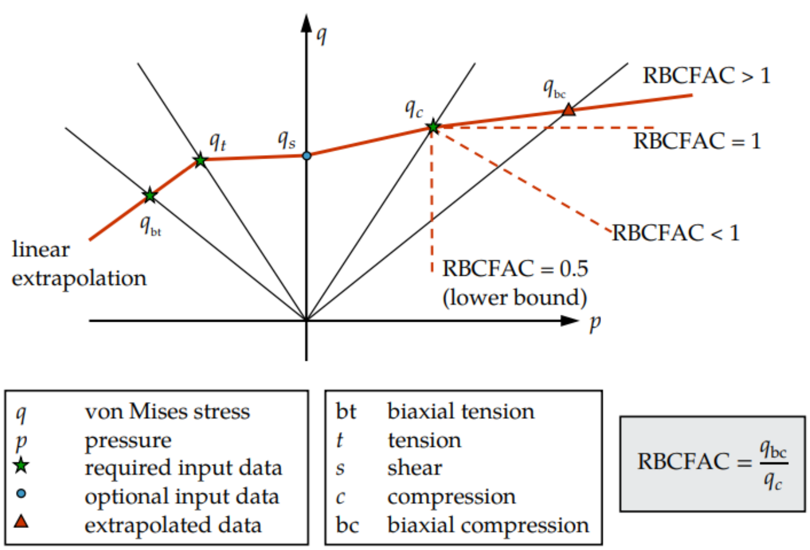

Figure 3.4. Yield surface implemented in MAT187 (ANSYS-LST, 2020)

Additional inputs to drive the material model for the epoxy resin cannot be obtained experimentally and hence are obtained by calibrating the FE model output with experimental tests. The following section explains the calibration procedure and presents the calibrated values that are used throughout the numerical analyses.

3.3. CALIBRATION OF MATERIAL PROPERTIES FOR EPOXY RESIN F3900

The material model for the matrix (MAT_187) requires more inputs than those obtained from experimental characterization of the epoxy resin. These include the input stress-plastic strain curve defining yield behavior under equi-biaxial tension (LCID-B), the ratio of yield stress in equi-biaxial compression to yield stress under pure compression (RBCFAC), the plastic Poisson's ratio (NUEP (ν_p)) which defines relationship between transverse and longitudinal plastic strains, the equivalent plastic strain value at onset of failure from uniaxial tension test (EPFAIL $\left(\bar{\varepsilon}_p^f\right)$), the curve which defines equivalent plastic failure strain ($\bar{\varepsilon}_p^f$) as a function of triaxiality (LCID-TRI) with normalized ordinate values, and the curve which defines equivalent plastic failure strain ($\bar{\varepsilon}_p^f$) as a function of element characteristic length (LCID-LC).

The stress ordinate in LCID-B was set to be 80% of the stress in LCID-T based on the recommendation from one of the developers of the material model (Khaled, et al., 2021). RBCFAC and NUEP were varied until the best match with experimental data for the tensile, compressive and shear experimental tests on the composite T800S/F3900 was achieved. The RBCFAC was varied from 0.75 to 1.0 while NUEP varied from 0.2 to 0.35. The best match has RBCFAC value of 0.95 and NUEP of 0.275 as shown in figure 3.5.

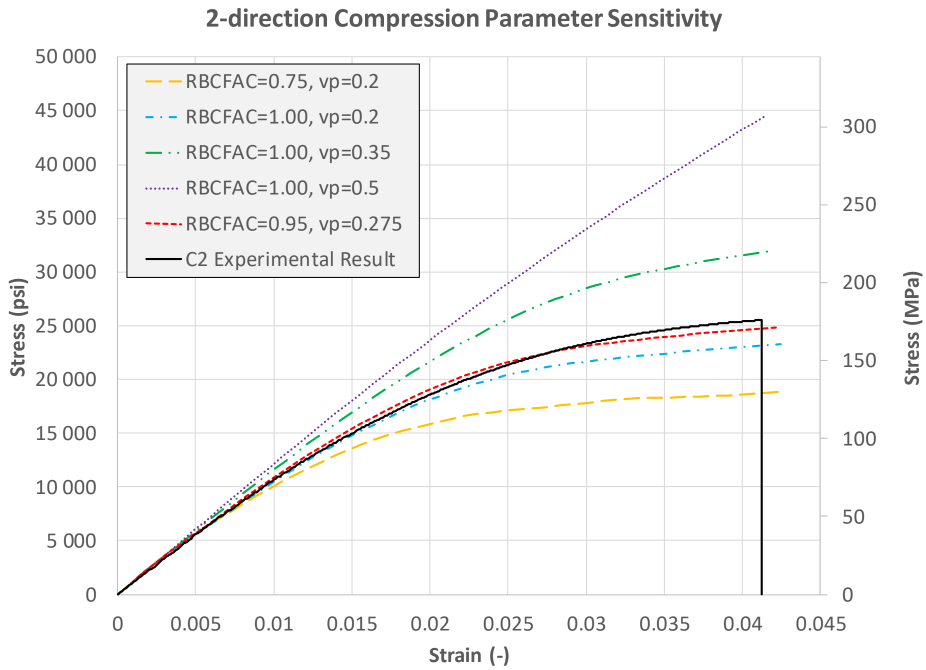

Figure 3.5. Result of calibration exercise for NUEP and RBCFAC using 2-direction compression test (Khaled, et al., 2021)

The equivalent plastic strain at failure $\left(\bar{\varepsilon}_p^f\right)$ is the parameter that determines failure onset in MAT_187. This value is difficult to measure experimentally since the composite does not remain in a state of uniaxial stress in a uniaxial test. The required input to MAT_187 is the equivalent plastic strain at failure from a uniaxial tension test. This value was taken to match the simulation response to that of the experiment.

Failure in MAT_187 is defined through tabulated input curve that provides the plastic strain at failure with respect to stress triaxiality. The details of failure modeling are found in (Kolling, et al., 2005). The failure curve for the matrix used in this study is shown in figure 3.6 and was calibrated in (Khaled, et al., 2021) and validated against experimental data.

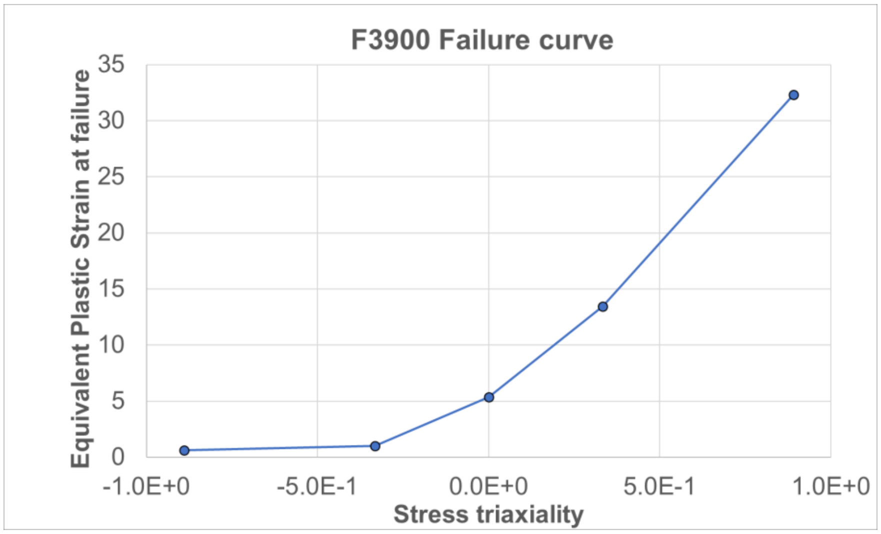

Figure 3.6. F3900 Failure Curve

Table 3.4. Input failure data for MAT_187: Stress triaxiality versus equivalent plastic strain at failure

Condition	$\frac{p}{\sigma_{vm}}$	**Equivalent Plastic Strain at Failure**	$f\left(\frac{p}{\sigma_{vm}}\right)$
Minimum Triaxiality	-0.890	0.0040	0.615
Uniaxial Tension	-0.333	0.0065	1.000
Iosipescu Shear	0.000	0.0350	5.385
Uniaxial Compression	0.333	0.0875	13.46
Maximum Triaxiality	0.890	0.2100	32.31

The failure modeling in MAT_187 allows for an input curve to define failure strain multiplier versus characteristic element length. This curve is used to reduce the effect of the element size on the failure predictions as shown in the mesh sensitivity analysis in section 4.7.2. The MAT_187 input data shown in table 3.5 accounts for the effect of the element characteristic length, l_{cr} , defined as the average length of spatial diagonals of the element, on the equivalent plastic strain at failure.

Table 3.5. Input failure data for MAT_187: Element characteristic length vs equivalent plastic strain at failure

Element characteristic length $\boldsymbol{l_{cr}}$	**Equivalent Plastic Strain at Failure**	$\boldsymbol{f(l_{cr})}$
$1.15(10^{-4})$	0.00702	1.08
$1.73(10^{-4})$	0.0052	0.845
$3.147(10^{-4})$	0.0065	1.0
$9.549(10^{-4})$	0.0065	1.0
$9.658(10^{-4})$	0.0065	1.0

4. FINITE ELEMENT MODEL GENERATION AND VALIDATION

The finite element simulation of unidirectional polymer matrix composite material up to failure is carried out through modeling of the composite at the constituent level. The building block for each model is a repeating unit cell (Harrington, et al., 2017) consisting of a cylindrical fiber embedded in a matrix phase.

In many simulations at the constituent level, the fiber/matrix interface is modeled as an additional phase using cohesive zone elements so as to capture the debonding between fiber and matrix during the simulation (Canal, et al., 2009; Vaughan & McCarthy, 2011; Totry, et al., 2008b). This notion remains vague since the interfacial zone in itself does not exist. It is created during numerical modeling of composites and the interfacial properties are difficult to assign or experimentally obtain (Teklal, et al., 2018). Various tests have been developed to characterize the interface and can be categorized into two groups depending on whether the measurements are taken from micro-composites made of single fiber or fiber tows embedded in matrix, or from actual composites (Rodríguez, et al., 2012). One shortcoming of the single fiber micro-composites is that they are not representative of the mechanical and physio-chemical condition of the actual composite (Rodríguez, et al., 2012). Another shortcoming of fiber/matrix interface characterization techniques is that there is a large scatter in the properties measured with different techniques on the same composite and there is no established standard to measure interfacial properties (Rodríguez, et al., 2012; Zhou, et al., 2001). In this study, a perfect bond is assumed between the fiber and matrix because of reasons stated earlier coupled with the fact that modeling the fiber/matrix in an earlier study (Parakhiya, 2020) did not yield superior results.

The finite element model generation details are presented in this chapter. Virtual test models created to mimic experimental specimen of tests carried out on the T800S/F3900 composites, are presented in detail for the tests performed with in-plane loading. Subsequently, the virtual test models for transverse loading are presented. The post-processing for obtaining homogenized failure data is explained next. Finally, the validation tests for each model are presented and discussed.

4.1. MODEL GENERATION

The composite is modeled at the constituent level with Repeating Unit Cells (RUC) made of a circular fiber embedded in a matrix as shown in Figure 4.1. A fiber bundle of the T800S/F3900 composite (Figure 3.1), is modeled as a single fiber in the RUC as described in (Parakhiya, 2020) and shown in Figure 4.2. The finite element model is then formed from multiple RUC in a square packing. RUC are routinely used [Gao et al., (2017); Li and Sitnikova (2020)] to predict the effective properties of composites. It was shown in (Gao, et al., 2017) through a theoretical approach that square and hexagonal packing of UCs produced the same results under periodic boundary condition due to uniqueness of solution. Moreover, regular fiber arrangements are observed in composites with high fiber volume fraction (Rodríguez, et al., 2012).

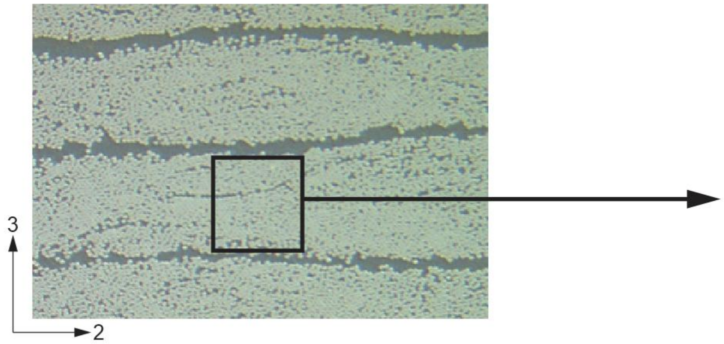

Figure 4.1. Optical micrograph of T800S/F3900 unidirectional composite

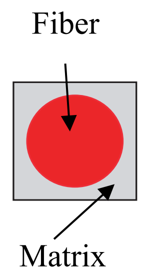

Figure 4.2. Repeating Unit Cell in with fiber in red and matrix in grey

In the case of in-plane tests, three-dimensional models, where normal loading is applied in the longitudinal and transverse directions as well as in-plane shear loading, was generated using an in-house computer program Virtual Testing Software System (VTSS) (Harrington, et al., 2017; Parakhiya, 2020). The software generates models that are geometrically proportional to the experimental specimen of the T800S/F3900 unidirectional composites (Harrington, et al., 2017; Parakhiya, 2020). The equivalent dimensions of each finite element (FE) model were computed by using the ratios $\left[1:\frac{\text{Length}}{\text{Thickness}}:\frac{\text{Width}}{\text{Thickness}}\right]$ to maintain a geometrical proportionality between the FE model and the experimental specimen.

The dimensions of a typical RUC in figure 4.3(a) are shown in table 4.1. The width of the unit cell, *a*, is the ply thickness on the panel type PT1 (Khaled, et al., 2018). The fiber radius, *r*, is determined to maintain a fiber volume fraction of 60%. The dimensions *dxy* and *dz* are standard element lengths while *L* defines the length of the model along the fiber direction. The values of the parameters in table 4.1 were obtained from (Harrington, et al., 2017; Parakhiya, 2020). The model is generated by stacking multiple unit cells in several rows and columns as shown in figure 4.3(b) and generates 3D (solid) finite elements.

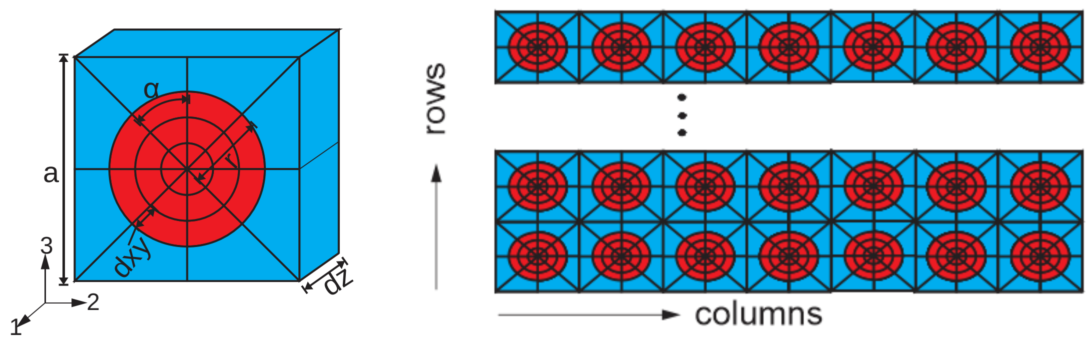

(a) (b)

Figure 4.3. VTSS model (a) RUC geometric parameter (b) stacking of multiple RUC (Khaled, et al., 2021)

Table 4.1. Dimension of a Unit Cell

Parameter	**Dimensions**
a (in)	0.007625
r (in)	0.00333
dxy (in)	0.001666
dz (in)	3.289
α	22.5^{o}

For transverse loading tests (i.e., transverse tension, compression and 2-3 plane shear), a two-dimensional (2D) model in the plane orthogonal to the fiber direction is generated. The same modeling approach as described above is used where two-dimensional RUC are packed in a square arrangement as depicted in figure 4.3(b). Two-dimensional plane strain finite elements are generated in this model. In the following sections, the complete finite element model for each test is described.

4.2. MODEL FOR IN-PLANE (1-2 PLANE) TESTS

The in-plane tests include longitudinal tension and compression, transverse tension and compression, in-plane shear tests as well as their combinations. In the previous work (Parakhiya, 2020; Khaled, et al., 2021), virtual test models were presented for simulating uniaxial tension and compression in the longitudinal and transverse direction as well as in-plane shear. Each model was generated to be consistent with experimental specimens (Khaled, et al., 2018) and later, each model was validated against experimental results for the corresponding test.

The first in-plane model subsequently referred to as “S1-S2 model”, is used for simulating tension and compression loadings in the longitudinal and transverse directions to produce uniaxial and biaxial states of stress. The second in-plane model, subsequently referred to as “S2-S21 model”, is used for transverse tension and compression loadings, as well as in-plane shear and the normal-shear combinations. The geometric dimensions of “S1-S2 model” are obtained from the experimental specimen for 2-direction compression (Khaled, et al., 2018) and is shown in figure 4.4. The tab section of the specimen, where grips are attached, are not modeled. Instead, boundary conditions are applied to induce the appropriate state of stress in the model. The equivalent (proportional) dimensions for the finite element model are shown in figure 4.5.

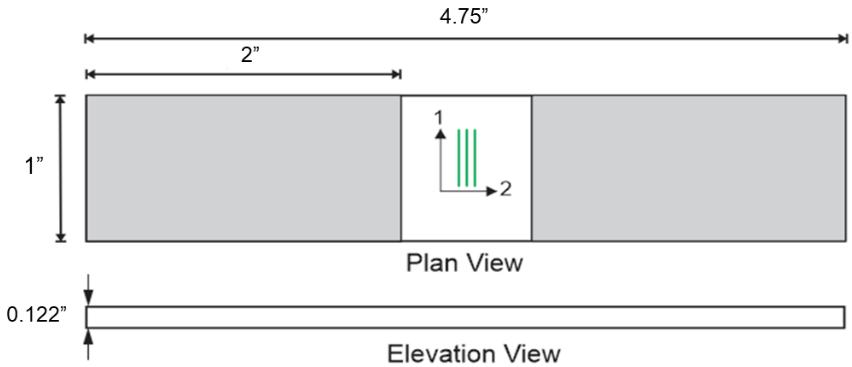

Figure 4.4. T800S/F3900 2-direction compression experimental test specimen

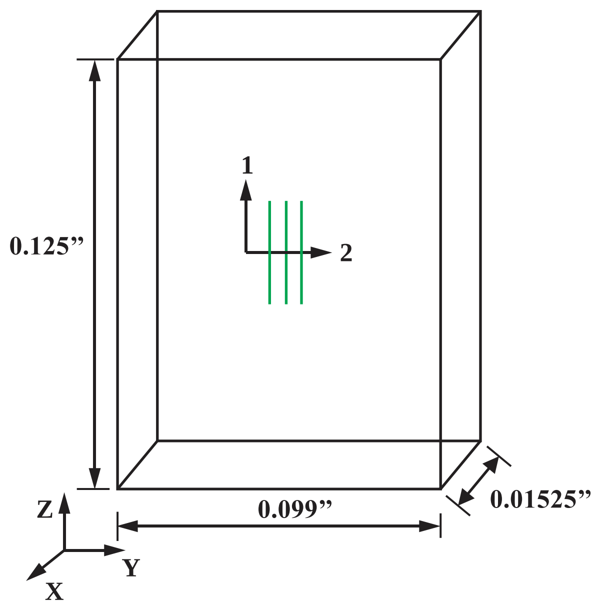

Figure 4.5. Equivalent geometrical dimensions of S1-S2 model

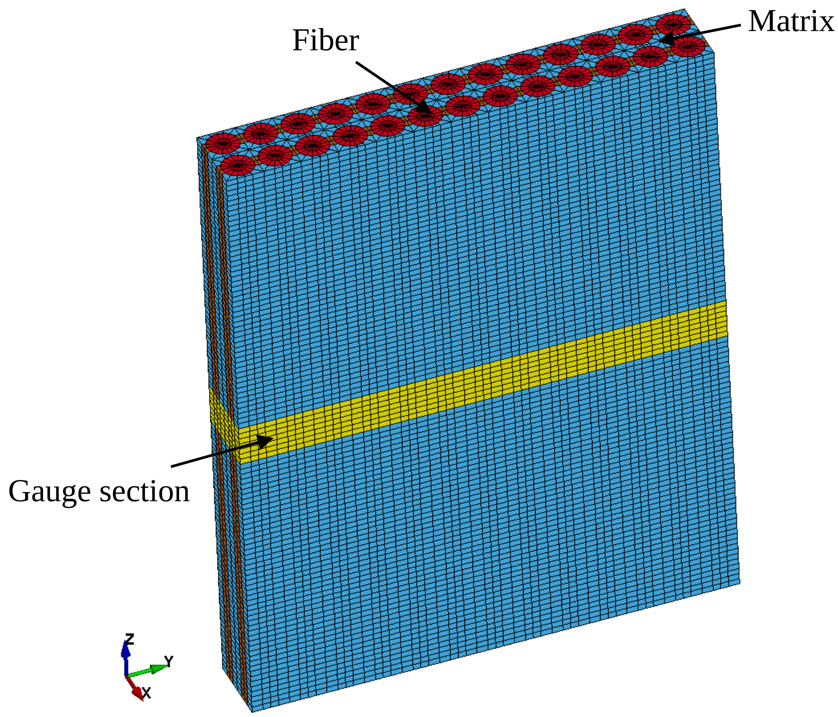

Figure 4.6. S1-S2 finite element model

The finite element model is shown in figure 4.6. It includes the fiber (red), the matrix (blue) and a gauge section (yellow). The gauge section represents the region over which volumetric averaging of stress and strain response is carried out to obtain homogenized response (see section 4.6). A convergence analysis was carried out in for this model (Parakhiya, 2020) to refine the parameters used in generating the model. The number of elements, number of nodes, maximum and minimum aspect ratios for three mesh densities are shown in table 4.2. The failure stresses and strains for the uniaxial compression test in the 2-direction shown in figure 4.7 is using the fine mesh. The fine mesh in (Parakhiya, 2020) for the 2-direction compression test is used in all subsequent virtual tests with the longitudinal and transverse normal loading.

Table 4.2. S1-S2 finite element model details

Parameter	Coarse	Medium	Fine
Number of elements	66144	87360	131040
Number of nodes	59454	78171	116706
Maximum aspect ratio	4.91	3.71	3.29
Minimum aspect ratio	2.968	2.74	2.56

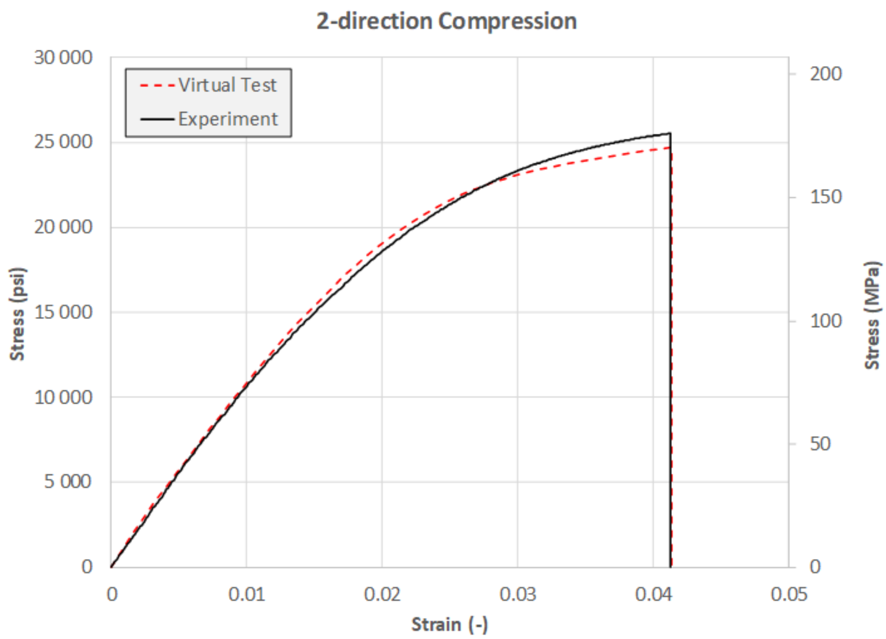

Figure 4.7. Mesh sensitivity for 2-direction compression test (Khaled, et al., 2021)

Similarly, the geometrical dimensions of S2-S21 model were obtained from the experimental specimen shown in figure 4.8. Only the middle portion was used in the finite element model. The equivalent (proportional) dimensions of the FE model are shown in figure 4.9.

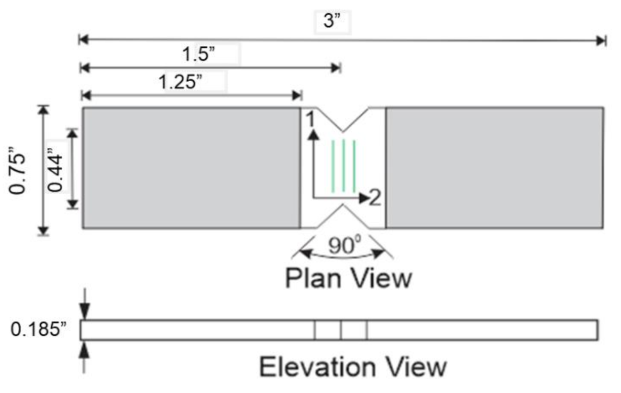

Figure 4.8. T800S/F3900 2-1 plane shear experimental test specimen

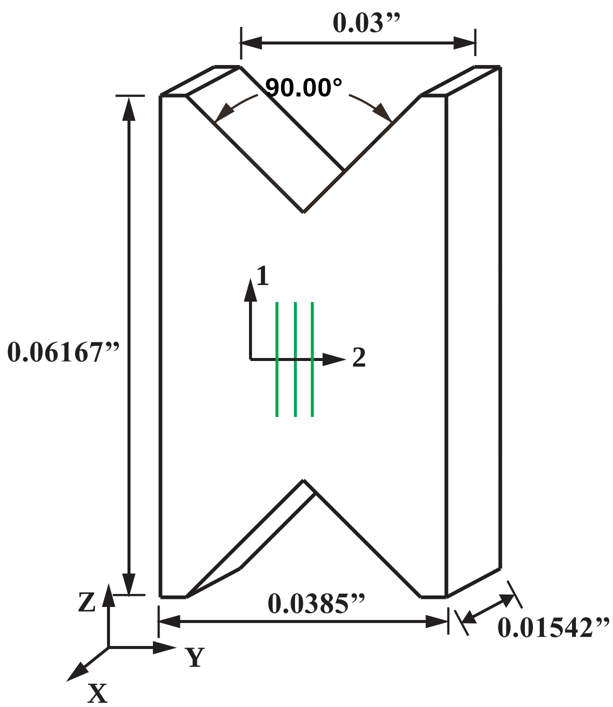

Figure 4.9. Equivalent geometrical dimensions of S2-S21 model

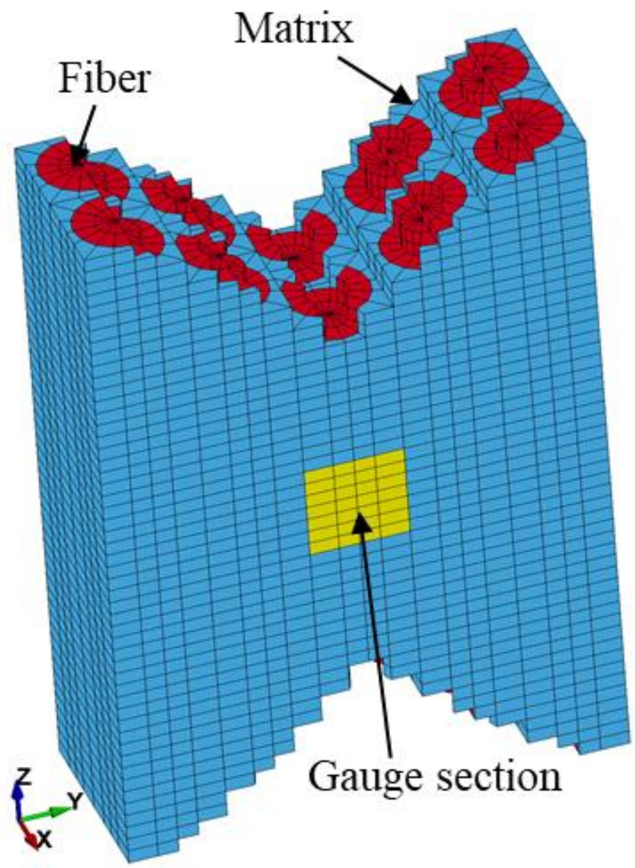

Figure 4.10. Finite element representation of S2-S21 model

The finite element model shown in figure 4.10 features the fiber (red), the matrix (blue) and a gauge section (yellow). The stress-strain curve shown in figure 4.11 for the in-plane shear tests using a V-notch model (Khaled, et al., 2021) is obtained from the fine mesh. The fine mesh for the in-plane shear test model in (Parakhiya, 2020) was used in all the analyses. The number of elements, number of nodes, maximum and minimum aspect ratios are shown in table 4.3.

Table 4.3. S2-S21 finite element model details

Parameter	**Coarse**	**Medium**	**Fine**
Number of elements	10014	13904	19824
Number of nodes	9631	13103	18604

Maximum aspect ratio	4.88	3.73	3.284
Minimum aspect ratio	2.95	2.76	2.56

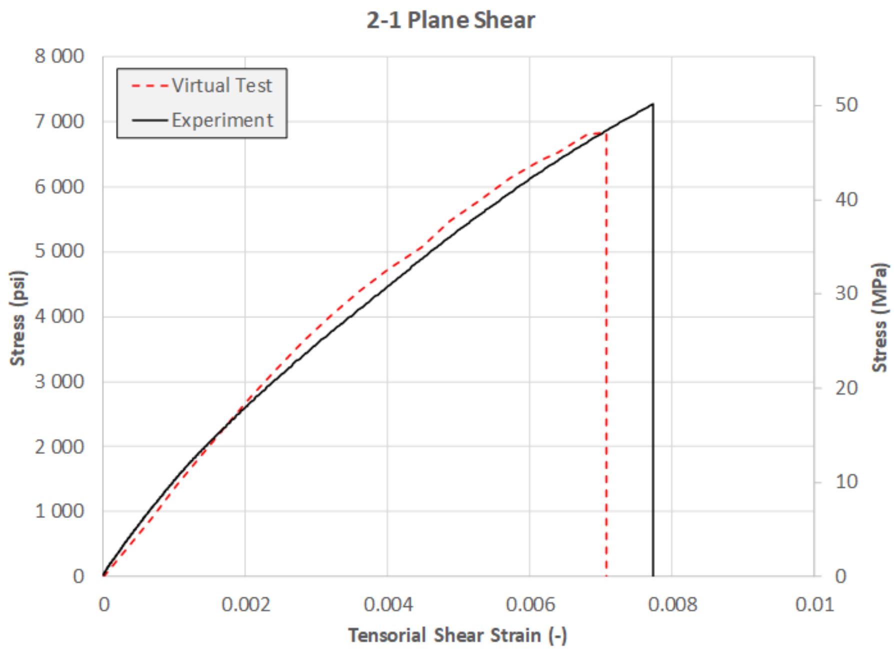

Figure 4.11. Mesh sensitivity for 2-1 plane shear test (Khaled, et al., 2021)

4.3. BOUNDARY CONDITIONS FOR IN-PLANE (1-2 PLANE) TESTS

Loading is applied through displacement boundary conditions to generate the finite element response from which failure data are extracted. The boundary conditions used in each of these tests are described below.

<u>Uniaxial tension/compression in the 1-direction tests: S1-S2 model</u>

The boundary conditions under longitudinal tension and compression are shown in figure 4.13. The nodes on the back face (y-z plane) are restricted in the x-direction, those on the left face (x-z plane) in y direction and those on the bottom face (x-y plane) in z direction. Motion is prescribed to nodes on the top face in positive and negative z direction for tension and compression respectively as shown in figure 4.12.

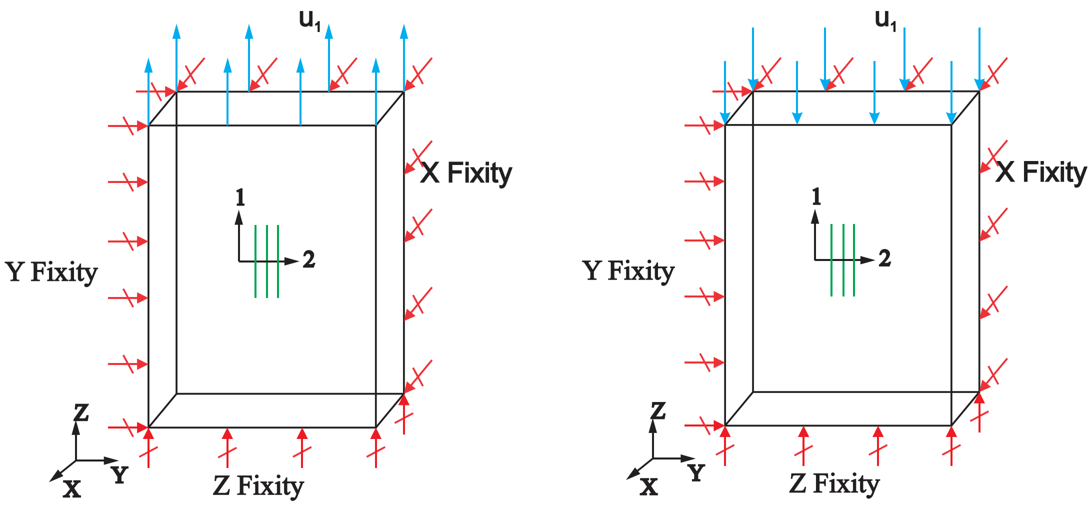

(a) (b)

Figure 4.12. Boundary condition for the S1-S2 model under (a) 1-direction tension (b) 1-direction compression

<u>Uniaxial tension/compression in the 2-direction tests: S1-S2 model</u>

For a 2-direction loading, the fixity conditions are the same as those used in the 1-direction loading scenarios. Motion is prescribed to the nodes on the right face in positive and negative y direction for tension and compression, respectively. The boundary conditions are shown in figure 4.13a and 4.13b respectively.

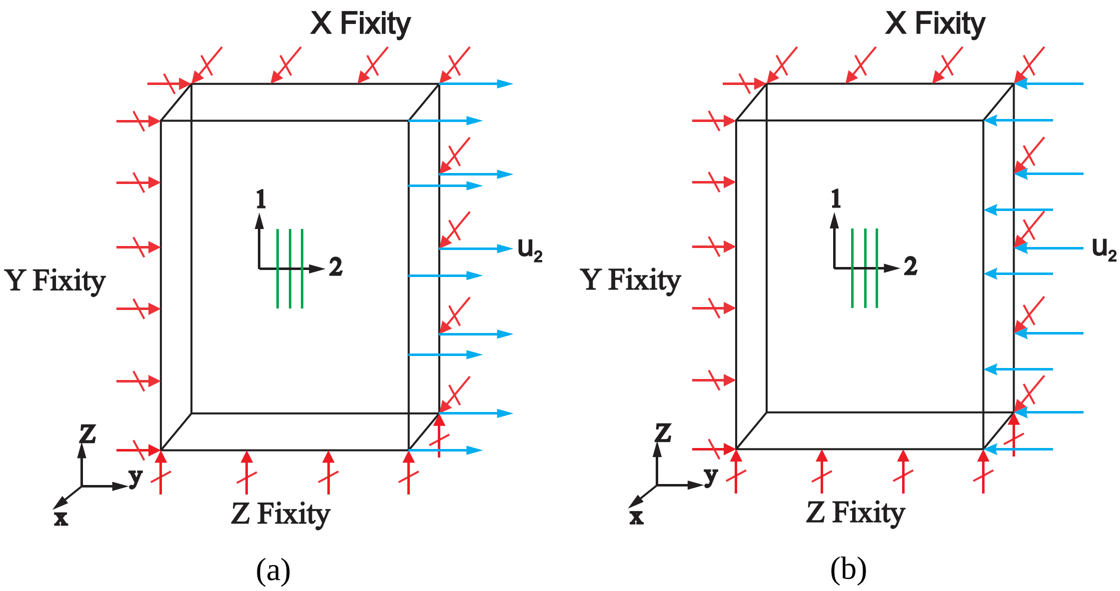

Figure 4.13. Boundary conditions for S1-S2 model under (a) 2-direction tension (b) 2-direction compression and (b) 2-direction compression

Combined 1-direction tension/compression and 2-direction tension/compression tests:

S1-S2 model

In biaxial loading, the loadings from the uniaxial tests are superposed and applied at different rates to generate a set of failure data. The nodal fixities remain the same as those used in the uniaxial loading tests. Motion is prescribed simultaneously in the 1-direction and in the 2-direction to produce biaxial state of stress in the material. The various test carried out are described in chapter 5. Figure 4.14 shows the fixity conditions and loading under biaxial compression in 1- and 2-directions.

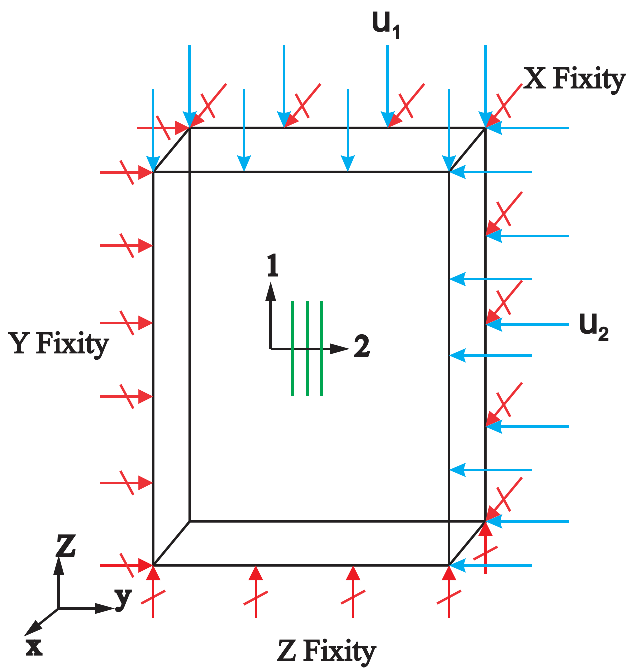

Figure 4.14. Boundary conditions for biaxial compression in 1- and 2-direction for S1-S2 model

The load curve (displacement versus time) in figure 4.15 was used to prescribe motion to the nodes. The curve was scaled up or down in each test to apply the load at different rates depending on the test.

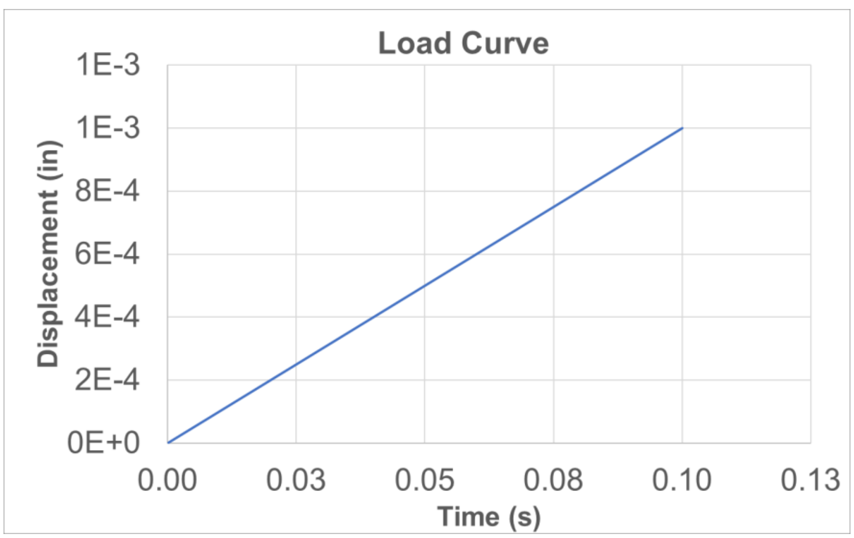

Figure 4.15. Load curve used to prescribe motion

Uniaxial tension/compression in the 2-direction: S2-S21 model

The fixity conditions for the S2-S21 model are such that the nodes on the back face are restricted in the z and y directions while those on the back face are restricted in the x direction.

The load is applied through uniform displacement boundary conditions. The uniform boundary conditions (UBC) were introduced by Hazanov and Amieur (1995) to determine macroscopic stiffness of heterogeneous bodies. They were used by Sun, et al (2019) to predict failure in unidirectional fiber-reinforced composite using representative volume elements. Periodic Boundary Conditions (PBC) are sometimes applied to RUC because to their periodic microstructures (Li, 2008). These define a relative displacement between periodic nodes (i.e., nodes on opposite sides) through constraint equations. These boundary conditions have, however, been implemented only in the implicit time integration scheme in LS-DYNA (Liu, et al., 2018). Since the finite element analyses in this study are carried out using explicit time integration scheme in LS-DYNA (ANSYS-LST, 2020) that does not support PBC, UBC is used instead. Uniform displacement boundary conditions, on the other hand, can be applied in explicit time integration scheme and have been shown to produce results close to those from PBC for sufficiently large Representative Volume Elements (RVE) (Kanit, et al., 2003; Pahr & Böhm, 2008). Equation 4.1 shows the expression used to prescribe motion based on uniform displacement boundary conditions.

$$u_2(\boldsymbol{X},t) = atX_2 \tag{4.1}$$

where

$u_2(\boldsymbol{X},t)$ is the displacement in the 2-direction (y direction) of boundary nodes,

$\boldsymbol{X}$ is the vector position of boundary nodes in the reference (undeformed) configuration,

a is the loading rate,

t is time, and

X_2 is the coordinate of boundary nodes in the 2-direction which acts as a scale factor.

The boundary nodes include the nodes in the notch. The use of uniform displacement boundary conditions is warranted due to the shape of the model as this guarantees a uniaxial state of stress throughout the simulation. A depiction of the fixity conditions as well as the displacement boundary conditions on the right face can be seen in figure 4.16.

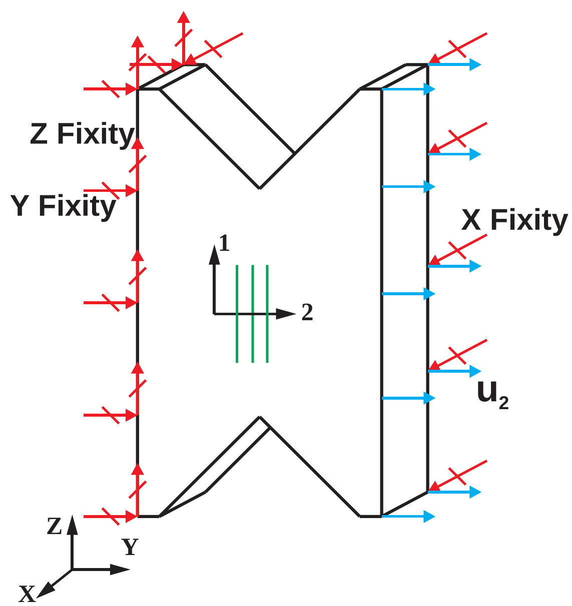

Figure 4.16. Boundary condition for the S2-S21 model under uniaxial transverse tension

<u>2-1 Plane shear test: S2-S21 model</u>

The fixity conditions for this test are the same as those used in the uniaxial transverse tension and compression tests. Displacement is applied on the right face in the

1-direction (z-direction) while motion in the 2-direction on the same face is restricted. This can be seen in figure 4.17.

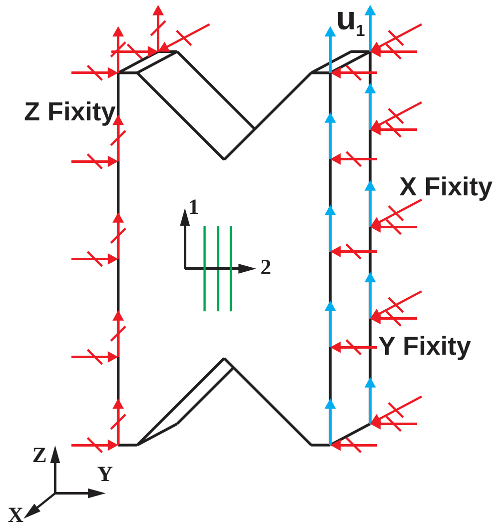

Figure 4.17. Boundary condition for the S2-S21 model under 2-1 plane shear

Combined 2-direction tension/compression and 2-1 plane shear: S2-S21 model

The fixity conditions for a combined transverse and in-plane shear loading are such that the left face is fixed in the y and z direction and the back face is fixed in the x direction (figure 4.18). The shear loading is applied through displacement boundary conditions on the right face in the 1-direction (z-direction) while the transverse loading is applied using the displacement boundary condition in equation 4.1. The transverse and in-plane loading can be applied both simultaneously and at different times depending on whether the loading needs to be tension/compression dominated or shear dominated. This is discussed in greater detail in chapter 5 where results for biaxial loadings are presented.

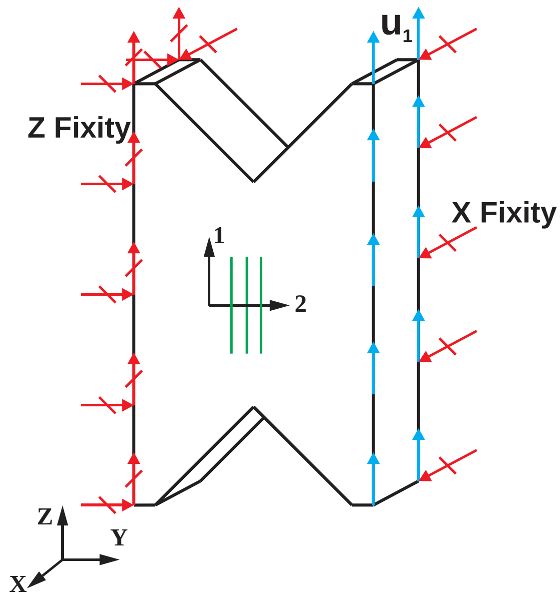

Figure 4.18. Boundary conditions on the S2-S21 model under combined transverse and in-plane shear loading

4.4. MODEL FOR OUT-OF-PLANE TESTS

A two-dimensional (2D) finite element model referred to as S2-S3 model (depending on whether it is subjected to only normal transverse loading or normal) and S2-S23 model (out-of-plane shear loading) under plane strain conditions is used to model of out-of-plane tests. Four stress components were recorded as state of stress in the model. The number of RUC in the model was increased to study their effect on the stress and strain response. Moreover, a mesh sensitivity analysis is carried out to study the effect of mesh density on the model.

In this study, three window sizes are investigated. Window size refers to the outer dimensions of the model and is a function of the number of RUC included in the model. The model generation technique presented in section 4.1 is used to generate square models with nine (9), twenty-five (25) and forty-nine (49) RUC.

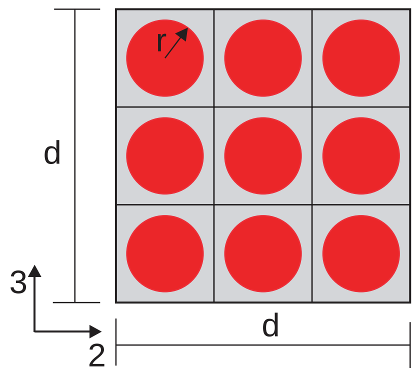

Figure 4.19. 9-Repeating Unit Cell (RUC) model

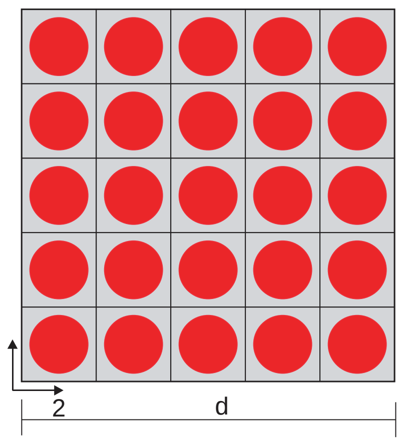

Figure 4.20. 25-Repeating Unit Cell (RUC) model

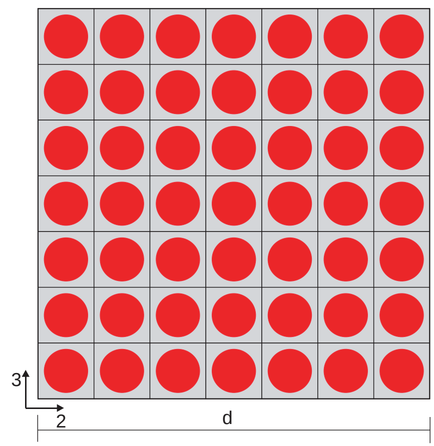

Figure 4.21. 25-Repeating Unit Cell (RUC) model

The 9-, 25- and 49- Repeating Unit Cell models, which are referred to as 9-RUC, 25-RUC and 49-RUC models, are shown in figure 4.19, figure 4.20 and figure 4.21, respectively. The variable d denotes the dimension of the model in the 2- and 3-directions while r is the radius of the fiber. The dimensions were taken from (Parakhiya, 2020) and are shown in the Table 2.1.

Table 4.4 Dimensions of the RUC model

Dimension	**9-RUC model**	**25-RUC model**	**49-RUC model**
d (in)	0.022875	0.038125	0.053375
r (in)	0.00333	0.00333	0.00333

4.5. BOUNDARY CONDITIONS FOR OUT-OF-PLANE (2-3 PLANE) TESTS

Loadings for the out-of-plane tests consists of transverse tension, transverse compression, out-of-plane shear and their combinations. The loadings are applied by imposing uniform displacement on the boundary of the RUC applying a displacement that is function of the position (coordinate) of the boundary node.

Equations for displacements as function of coordinates of boundary nodes in the undeformed configuration and time were derived for each test. An in-house code was used to generate the boundary conditions as LS-DYNA input.

Pure shear test in the 2-3 plane

Given the deformation mapping below

$$\begin{aligned} x_1 &= X_1 \\ x_2 &= \frac{1}{2}(X_2 + X_3)e^{at} + \frac{1}{2}(X_2 - X_3)e^{-at} \\ x_3 &= \frac{1}{2}(X_2 + X_3)e^{at} - \frac{1}{2}(X_2 - X_3)e^{-at} \end{aligned} \tag{4.2}$$

where

t is the time,

x_1, x_2 and x_3 are the coordinates of boundary nodes in the deformed configuration,

X_1, X_2 and X_3 are the coordinates of the boundary nodes in the undeformed configuration, i.e., $t = 0$, and

a is the rate of loading.

The determinant of the deformation gradient, i.e., the Jacobian of the deformation mapping, is equal to 1 regardless of the value of the rate of loading a. This ensures that a state of pure shear is maintained throughout the deformation. The loading matrix is derived from the deformation mapping shown in equation (4.2) as a function of time only. The applied displacement is then the product of the loading matrix and the position (coordinates) of boundary nodes in the undeformed configuration. These are shown in equations 4.3 and 4.4.

$$\begin{bmatrix} u_1 \\ u_2 \\ u_3 \end{bmatrix} = \begin{bmatrix} 0 & 0 & 0 \\ 0 & 0.5(e^{at}+e^{-at})-1 & -0.5(e^{at}-e^{-at}) \\ 0 & -0.5(e^{at}-e^{-at}) & 0.5(e^{at}+e^{-at})-1 \end{bmatrix} \begin{bmatrix} X_1 \\ X_2 \\ X_3 \end{bmatrix} \tag{4.3}$$

where $\mathbf{u}$ is the displacement vector, u_1, u_2 and u_3 are the components of the displacement vector.

The motion prescribed to the undeformed configuration in figure 4.22 results in a pure shear deformation in figure 4.23. A single node at the origin is fixed in the 2- and 3-directions to eliminate any rigid body motion.

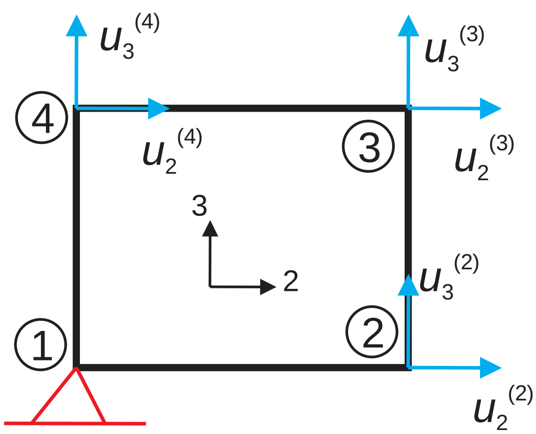

Figure 4.22. Undeformed RUC in the 2-3 plane

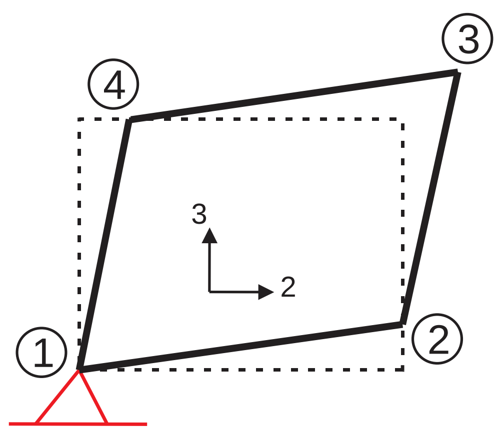

Figure 4.23. Deformed configuration under pure shear in the 2-3 plane

<u>Uniaxial tension/compression in the 2- and 3-directions</u>

Loading for uniaxial tension and compression is applied by prescribing a uniform displacement to the boundary of the model. A loading matrix is used to prescribe motion in similar fashion as shown in equation 4.3. The motion is prescribed to the boundary nodes of the RUC through the equations of displacement shown below. The displacement in the 1-direction is not shown because it is zero in a 2D model.

$$\begin{bmatrix} u_2 \\ u_3 \end{bmatrix} = \begin{bmatrix} bt & 0 \\ 0 & 0 \end{bmatrix} \begin{bmatrix} X_2 \\ X_3 \end{bmatrix}$$
$$\begin{bmatrix} u_2 \\ u_3 \end{bmatrix} = \begin{bmatrix} 0 & 0 \\ 0 & ct \end{bmatrix} \begin{bmatrix} X_2 \\ X_3 \end{bmatrix} \tag{4.5}$$

where b and c are rate of loading for uniaxial tests in the 2- and 3- directions, respectively. A positive value of b or c results in tension loading while a negative value results in compression loading. A single node at the origin is fixed in both 2 and 3 directions to prevent rigid body motion. A deformed configuration under uniaxial tension is shown in figure 4.24. Motion is prescribed only to the degree of freedom in the direction of loading, all other degrees of freedom are unconstrained to allow for Poisson's effect.

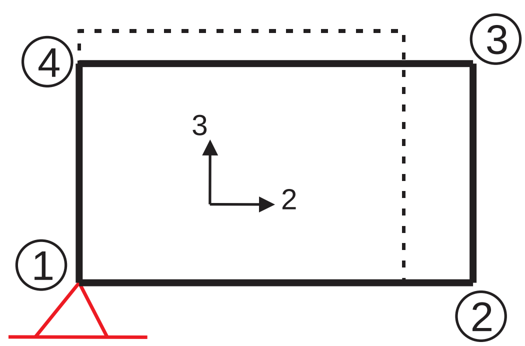

Figure 4.24. Deformed configuration under 2-direction tension

<u>Combined tension, compression and/or shear in the 2-3 plane</u>

In the case of combined loading, equations 4.4 and 4.5 are superposed to obtain the prescribed motion to the S2-S3 (only normal transverse loading) or S2-S23 model (transverse normal and 2-3 plane shear loading) in a biaxial test. The loading matrix for a series of biaxial tests described in chapter 5 is shown in the table 4.5.

Table 4.5. Multiaxial loading matrix

Test	**Loading matrix**
2-direction tension/compression and 3-direction tension/compression	$\begin{bmatrix} 0 & 0 & 0 \\ 0 & bt & 0 \\ 0 & 0 & ct \end{bmatrix}$
2-direction tension/compression and shear in the 2-3 plane	$\begin{bmatrix} 0 & 0 & 0 \\ 0 & 0.5(e^{at}+e^{-at})-1+bt & -0.5(e^{at}-e^{-at}) \\ 0 & 0.5(e^{at}+e^{-at}) & 0.5(e^{at}+e^{-at}) \end{bmatrix}$

4.6. POST-PROCESSING

Homogenization is the process of generating structural scale stress and strain response from constituent scale response. In this study, a volumetric averaging is used to compute homogenized response. The homogenization is carried out in two steps. First, the average response for each phase is computed by averaging the stress or strain in all the finite elements over the volume of the phase material (i.e., fiber and matrix). Second, the average response for the entire composite computed from the volumetric average over the volume of the entire composite. The two steps are combined in equation 4.6.

$$\bar{P}_h = \frac{\sum_{j=1}^{e_t} \left(\frac{\sum_{i=1}^{n_{e_t}} \bar{P}_i V_i}{\sum_{i=1}^{n_{e_t}} V_i} \right)_j V_j}{\sum_{j=1}^{e_t} V_j} \tag{4.6}$$

where

$\overline{P}_h$ is the homogenized response,

$\overline{P}_i$ is the response of the ith element calculated from stresses and strains averaged over the total number of integration points of the element,

e_t is the number of different element types (phases),

n_{e_t} is the number of element in the jth element type, and

V_i is the volume of the ith element in the case of solid element.

4.7. VALIDATION TESTS

The finite element models generated in the previous sections are validated against experimental tests conducted on the T800S/F3900 composites (Khaled, et al., 2018). The S1-S2 model is validated against uniaxial longitudinal and transverse experimental tests, the S2-S21 model against transverse normal and in-plane shear experimental tests, while the two-dimensional model in the 2-3 plane is validated against transverse and out-of-plane (2-3 plane) shear experimental tests. Failure in the finite element simulation is defined as the decrease of load carrying capacity after a suitably defined peak stress is reached such that any additional loading leads to a significant decrease in the stress until element erosion.

The analysis was done under explicit time integration. The energy checks were carried out for all tests. The kinetic energy was less than 1% of the total energy. The hourglass energy was numerically insignificant while the internal energy was numerically equal to the total energy, signifying that there was no rigid body mode in the simulations. The details of the finite element simulation including the computing platform used for the tests are shown in table 4.6.

Table 4.6. Details of the finite element simulation

LS-DYNA Version	mpp d Dev
Revision	136277
Analysis Type	EXPLICIT
1-2 plane model type	ELFORM=2, 8-noded solid hexagonal elements, 6-noded solid wedge elements
2-3 plane model type	ELFORM=13, 4-noded quadrilateral elements
Computing Platform	ASU AGAVE CLUSTER (made of 14,000 CPU cores and 300 GPU accelerators)[4]

4.7.1. VALIDATION OF IN-PLANE TESTS USING S1-S2 MODEL

The S1-S2 model, a three-dimensional model, is validated against uniaxial tests in 1-direction tension, 1-direction compression, 2-direction tension and 2-direction compression. The experimental data used in these tests are taken from (Khaled, et al., 2018). The stress-strain curve from FE simulation is simply referred to as “Simulation” while the curve from experimental testing is referred to as “Model Curve” (the average response from all experimental tested specimens (Khaled, et al., 2018)).

S1-S2 MODEL UNIAXIAL TENSION TEST IN 1-DIRECTION

Model: The S1-S2 model presented in section 4.2 was used for this test. The motion was prescribed to boundary nodes to produce a uniaxial tensile stress along the fiber direction.

[4] https://cores.research.asu.edu/research-computing/user-guide

Results: A uniform strain develops in the matrix and fiber as shown in (Parakhiya, 2020; Khaled, et al., 2021). The stress-strain plot in figure 4.25 shows that the simulation overpredicts the stiffness as the load increases. The strain at failure is underpredicted by 2.4% and the peak stress is over predicted by 4.6% compared to experimental data.

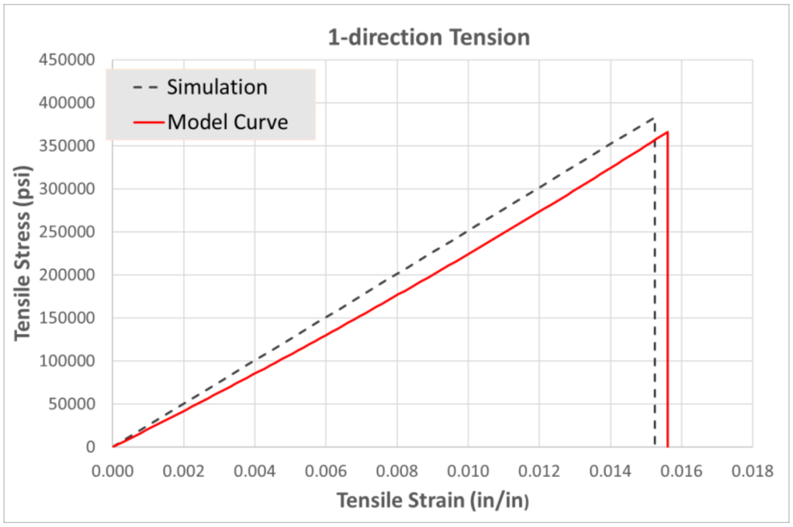

Figure 4.25. Stress strain curve for 1-direction tension using the S1-S2 model

Failure initiates in the fiber since it carries most of the applied load. Matrix elements were eroded subsequently as shown in figure 4.26.

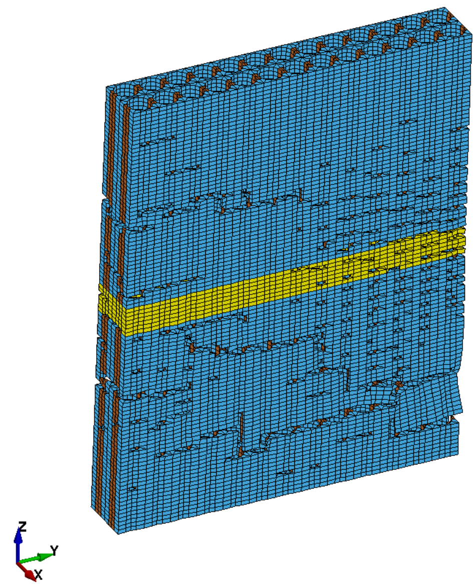

Figure 4.26. 1-direction tension failed specimen using the S1-S2 model

Discussions: The mismatch between the experimental peak stress, ultimate strain, and the stiffness and simulation is likely due to the assumption that there is no initial fiber misalignment in the simulation.

S1-S2 MODEL UNIAXIAL COMPRESSION IN 1-DIRECTION

Model: The boundary conditions for tension test in the longitudinal direction were applied to induce a state of uniaxial stress in the longitudinal direction.

Results: The stress distribution is shown in (Khaled, et al., 2021). The stress-strain curve in figure 4.28 shows that the initial stiffness from the simulation matches that of the model curve. However, as the strain increases, model curve shows a slight nonlinearity as reported in (Khaled, et al., 2018) while the stiffness from the simulation remains constant. This is probably due to the fact that the fiber is modeled as linear elastic. The peak stress is overpredicted by 8.3% and the ultimate strain at failure underpredicted by 0.5% compared to the experimental results

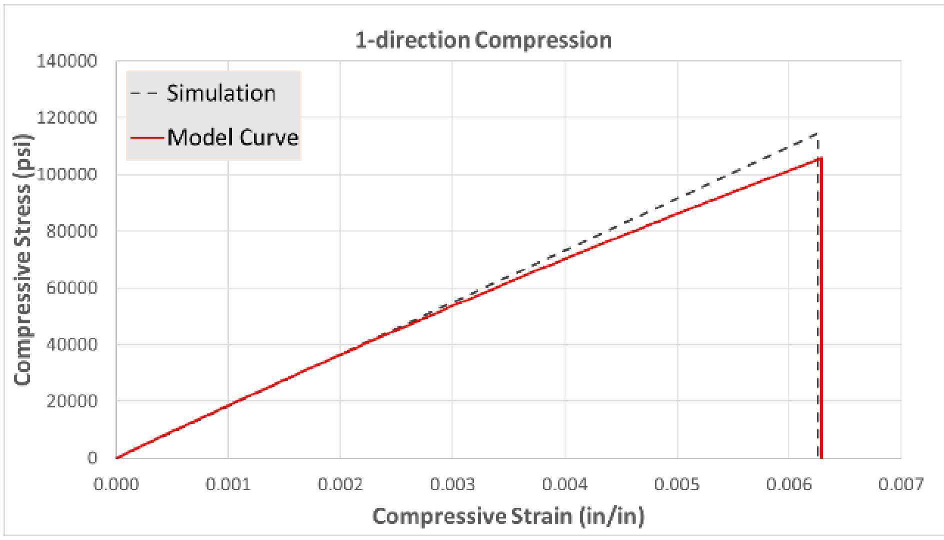

Figure 4.27. Stress-strain curve for 1-direction compression using the S1-S2 model

The failed specimen in figure 4.28 shows that only fiber elements are eroded. The erosion criterion for fibers in compression was reached by most fibers at the same time since the strain is uniformly distributed in the specimen.

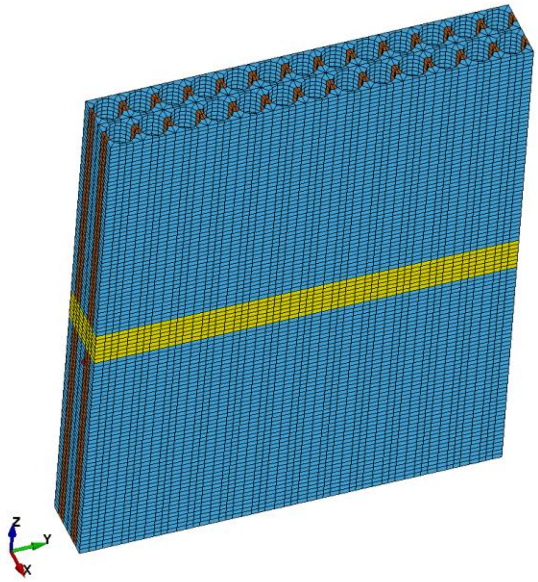

Figure 4.28. 1-direction compression failed specimen using the S1-S2 model

<u>Discussion</u>: The nonlinearity in the model curve can be attributed to microbuckling of the fiber. This nonlinearity is not captured in the simulation result due to the fiber being

modeled as a linear elastic material and the behavior in the 1-direction is mostly controlled by the fiber elements as shown in the failed specimen (figure 4.28).

S1-S2 MODEL UNIAXIAL TENSION IN 2-DIRECTION

Model: The S1-S2 model was subject to 2-direction tensile loading up to failure.

Results: The response of the simulation in figure 4.29 shows that the stiffness of the simulation curve matches that from virtual test. The peak stress in the simulation curve is 3.5% less and the ultimate strain is 4% less than the experimental values. The failed specimen in figure 4.30 shows a crack through the model in the direction perpendicular to the loading direction (y-direction).

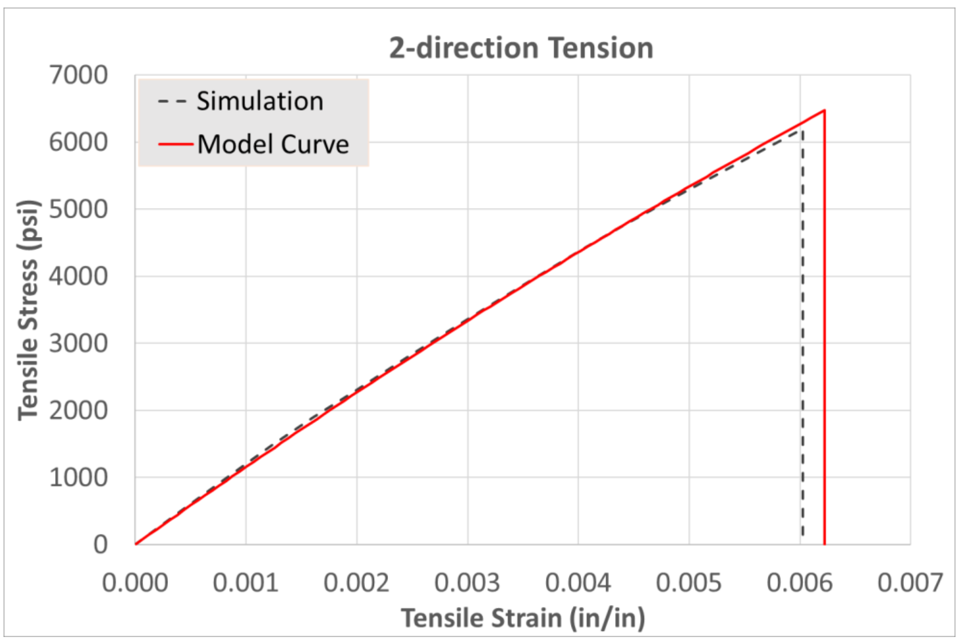

Figure 4.29. Stress-strain curve for 2-direction tension using the S1-S2 model

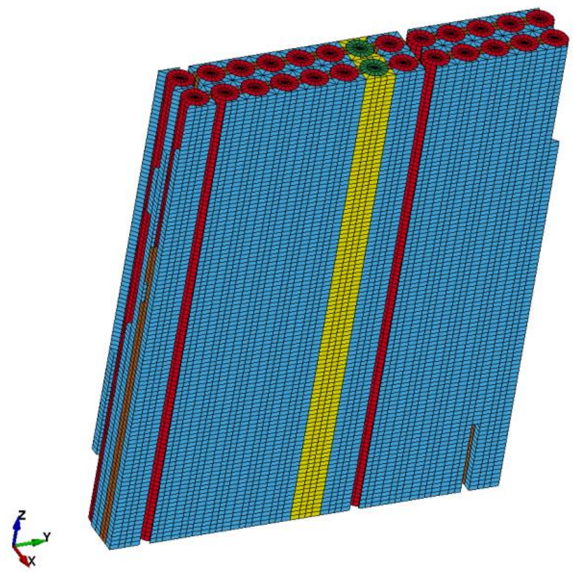

Figure 4.30. 2-direction tension failed specimen using the S1-S2 model

Discussion: The underprediction of the failure stress and strain is most likely due to the smaller size of the model in the transverse direction compared to the 2-direction tension specimen (Khaled, et al., 2018).

S1-S2 MODEL UNIAXIAL COMPRESSION IN 2-DIRECTION

Model: The S1-S2 model was used for simulation of 2-direction compression test. The boundary conditions for 2-direction compression test are shown in figure 4.12b. The displacement is prescribed in the negative y direction until the model fails.

Results: The stress strain curve in figure 4.31 shows a good agreement with the experimental result both in stress and strain. The maximum stress from the simulation is 3% less than the maximum stress from experimental test while strains from simulation and experiment are essentially the same.

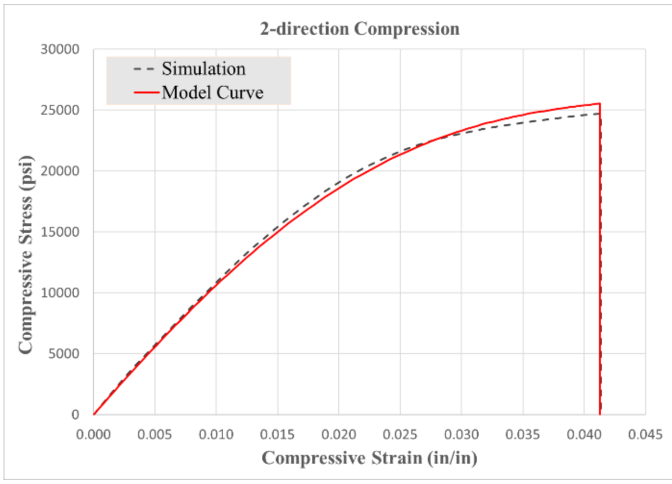

Figure 4.31. Stress-strain curve for 2-direction tension using the S1-S2 model

The failure mode under transverse compression is shown in figure 4.32. There are cracks in the matrix at the bottom of the specimen and at the left and right faces. No failure occurs in the fiber phase.

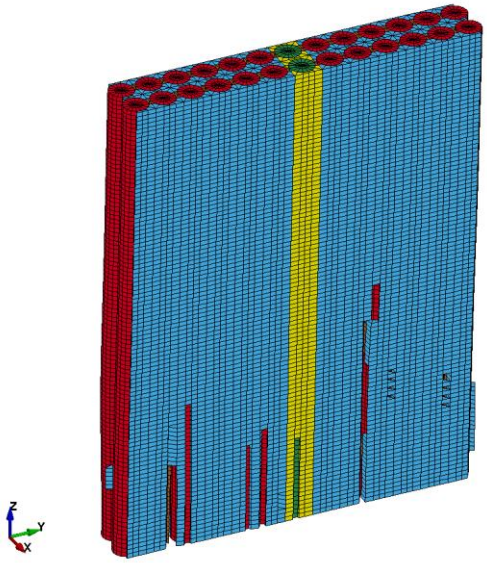

Figure 4.32. 2-direction tension failed specimen using the S1-S2 model

<u>Discussion</u>: The simulation stress-strain curve agrees well with the experimental data.

4.7.2. VALIDATION OF IN-PLANE TESTS USING S2-S21 MODEL

The validation tests for the S2-S21 model are shown next. These include the uniaxial tension in the 2-direction, uniaxial compression in the 2-direction, and 2-1 plane shear tests.

S2-S21 MODEL UNIAXIAL TENSION IN 2-DIRECTION

Model: The S2-S21 model shown in figure 4.10 is used in this test. The loading in the transverse direction was applied using uniform displacement boundary conditions, where a scaled displacement is applied to boundary nodes (including nodes in the notch) to produce a uniform displacement and to ensure that the model remains in a state of uniaxial stress as explained in section 4.3.

Result: The effective plastic strain in the matrix is one of the critical parameters in failure prediction in the matrix elements as explained in section 3.3. The distribution of the effective plastic strain in the model is shown in figure 4.33(a). It is uniformly distributed throughout the model along the y-direction. Figure 4.33(b) shows the Y stress (2-direction stress) distribution in the matrix while figure 4.33(c) shows a top view of Y stress (2-direction stress) distribution in the entire model. Both figures show a uniformly distributed stress with the stress in the fiber being larger than that in the matrix because of its higher elastic modulus. The model at failure (after peak stress) is shown in figure 4.33(d). Only deleted elements after failure are shown. Element erosion takes place in the middle portion, right face and in the left portion of the model. The stress-strain response of the model is shown in figure 4.34.

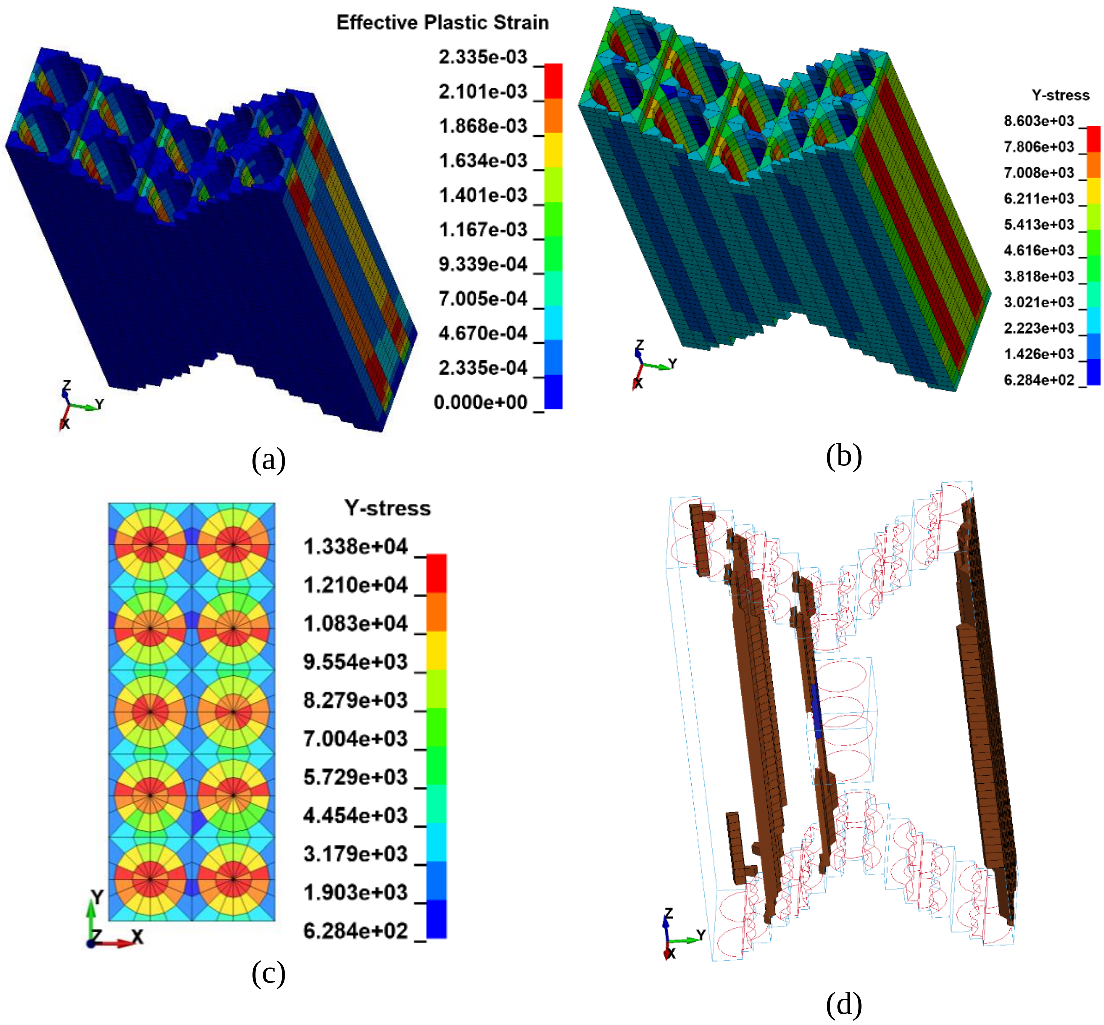

Figure 4.33. Response of the S2-S21 model under 2-direction tension (a) Effective plastic strain plot (b) Y-stress distribution in the matrix (c) Y-stress distribution in the model (top view) (d) Failed model (deleted elements shown)

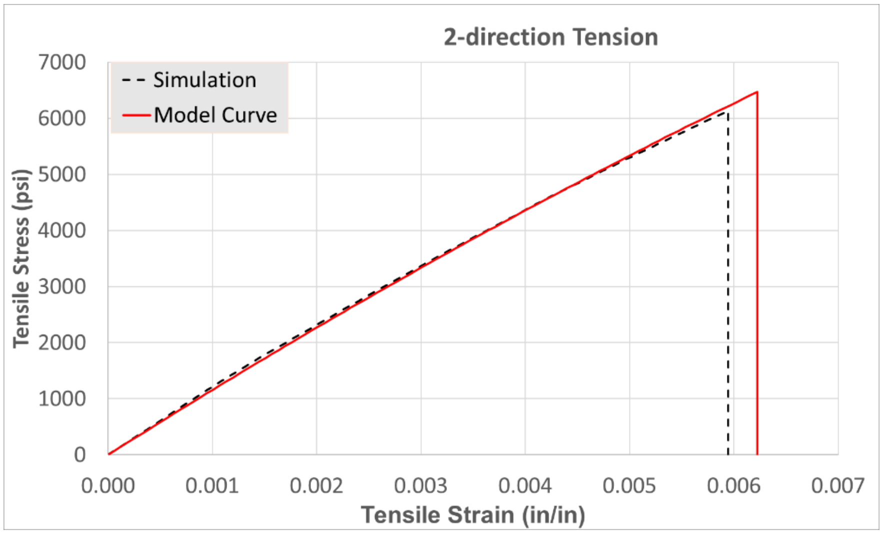

Figure 4.34. Stress-strain curve for 2-direction tension using S2-S21 model

Discussion: The stiffness of the simulation curve matches the model curve although it fails at slightly lower stress and strain values. This is due to the smaller size of the S2-S21 model in the 2-direction (loading direction) compared to the experimental specimen (Khaled, et al., 2018).

S2-S21 MODEL UNIAXIAL TENSION IN 2-DIRECTION

Model: The S2-S21 model is used in this test. Analogous to the uniaxial tension, uniform displacement boundary conditions are used to prescribe motion to the model. The left face is fixed in the 1- and 2-directions as shown in figure 4.16.

Results: The effective plastic strain in the matrix is uniformly distributed as shown in figure 4.35(a). The stress distribution in the matrix (figure 4.35(b)) shows that there is no stress concentration in the matrix at the notch. Figure 4.35(c) indicates a uniform stress distribution in both the matrix and the fiber. The failed specimen in figure 4.35(d) shows only deleted elements at failure. A bulk of elements in the left port of the model are eroded primarily due to the fixity conditions on the left face as are a few elements in the center of the model. Transverse compressive loading causes large strains in the matrix thus causing the specimen to fail at lower stress (6.4% less) and lower strain (16% less) than the experimental curve (figure 4.36).

<u>Discussion</u>: The under prediction of the failure stress and strain at failure is most likely attributable to the smaller size of the S2-S23 model in the 2-direction compared to S1-S2 model. The fixity condition on the left face causes substantial plastic strain accumulation in the left portion of the model. This results in a loss of load carrying capacity at a lower strain value in the 2-direction.

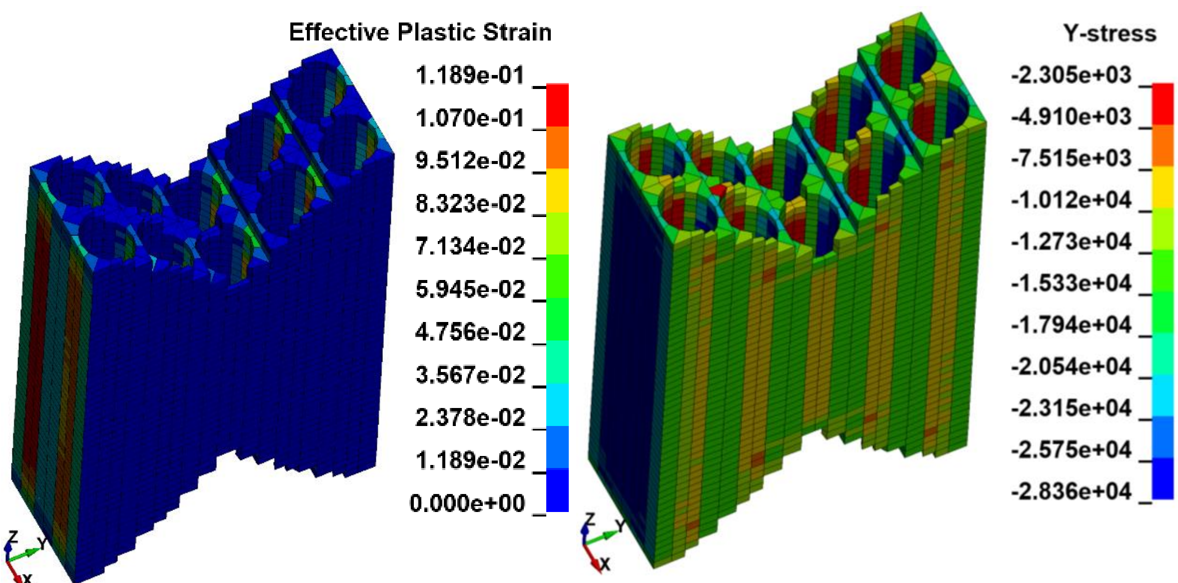

(a) (b)

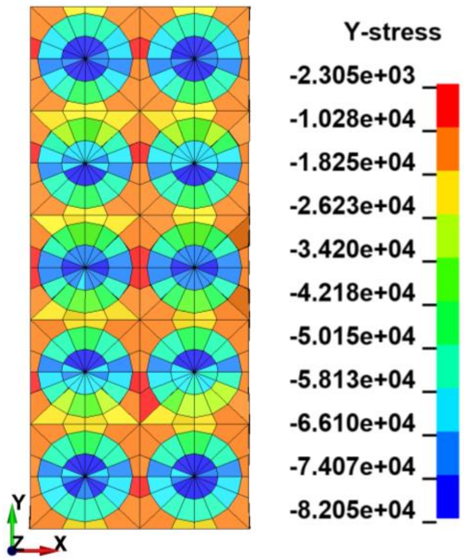

(c)

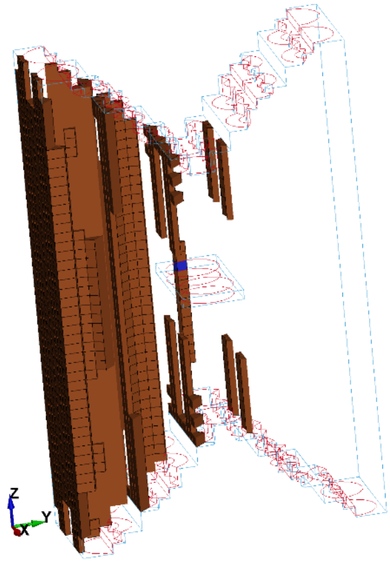

(d)

Figure 4.35. Response of the S2-S21 model under 2-direction compression (a) Effective plastic strain plot (b) Y-stress distribution in the matrix (c) Y-stress distribution in the model (top view) (d) Failed model (deleted elements shown)

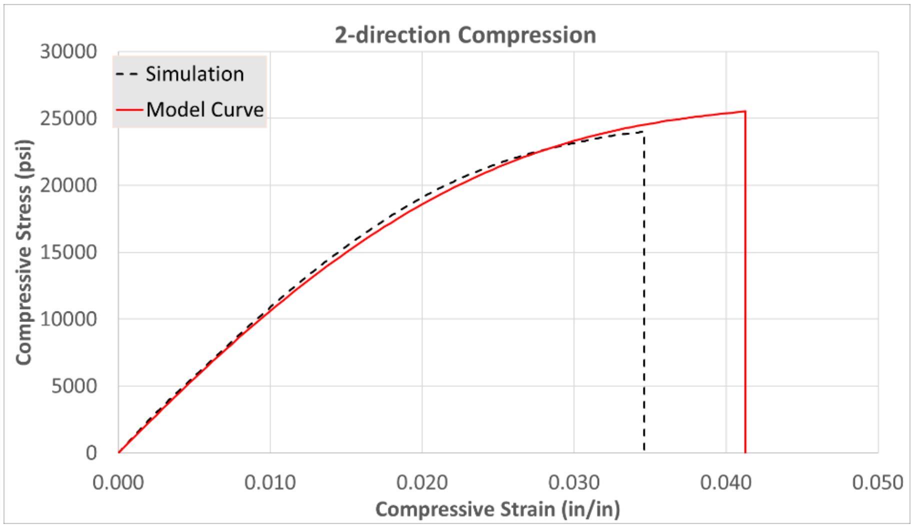

Figure 4.36. Stress-strain curve for 2-direction compression using S2-S21 model

<u>S2-S21 MODEL 2-1 PLANE SHEAR</u>

<u>Model</u>: The boundary conditions applied to the S2-S23 model for the 2-1 plane shear test are described in section 4.3.

Results: Figure 4.37(a) shows that there is no stress concentration in the matrix. However, the stress in the fiber middle portion of the of the model (gauge section) is the highest (figure 4.37(b)). The failed specimen is shown in figure 4.37(c). The matrix elements in the middle portion are eroded first. This results in stress redistribution which causes the elements in the lower left and upper right corner to also erode. The stress strain curve in figure 4.38 shows the stress strain curve from the simulation versus that from experiments. The normal stress components along the 1 and 2-directions are initially zero (figure 4.39), but later increase in magnitude with the stress in the 1-direction reaching 9% of the peak shear strength. This suggests that the model is in a state of pure shear only until the time failure initiation takes place in the middle.

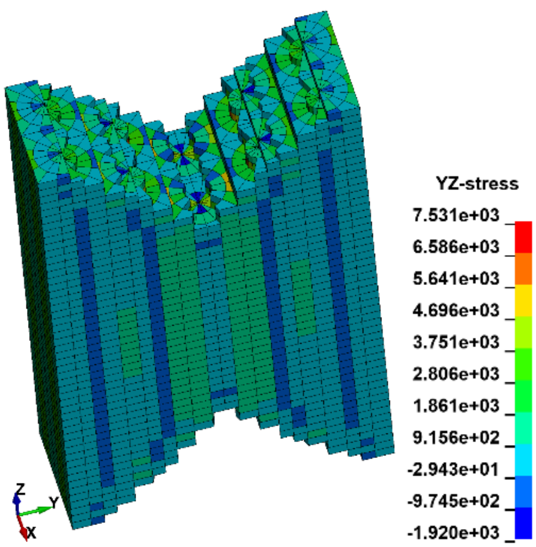

(a)

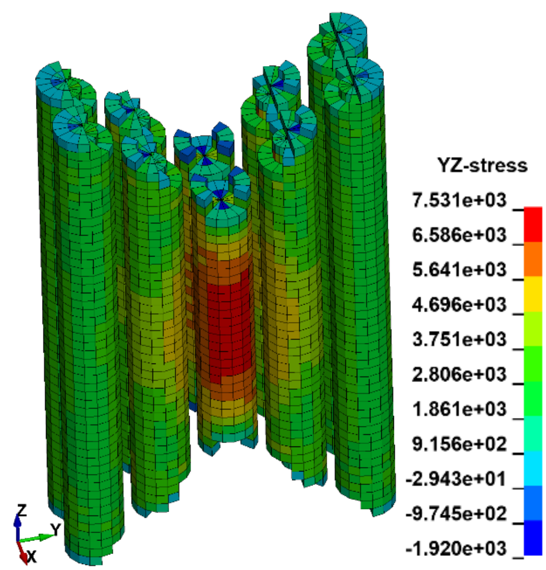

(b)

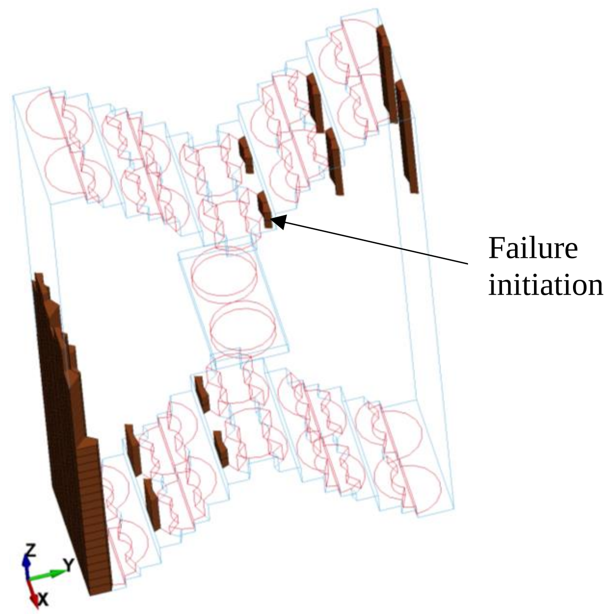

(c)

Figure 4.37. Response of the S2-S21 model under 2-direction (a) YZ-stress distribution in the entire model (b) YZ-stress distribution in the fiber (c) Failed model (deleted elements shown)

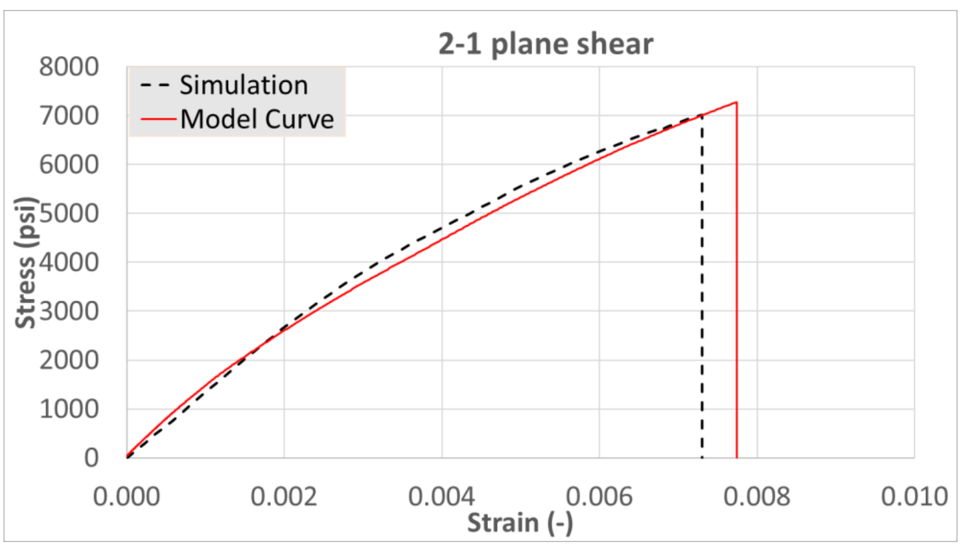

Figure 4.38. Stress-strain curve for 2-1 plane shear using S2-S21 model

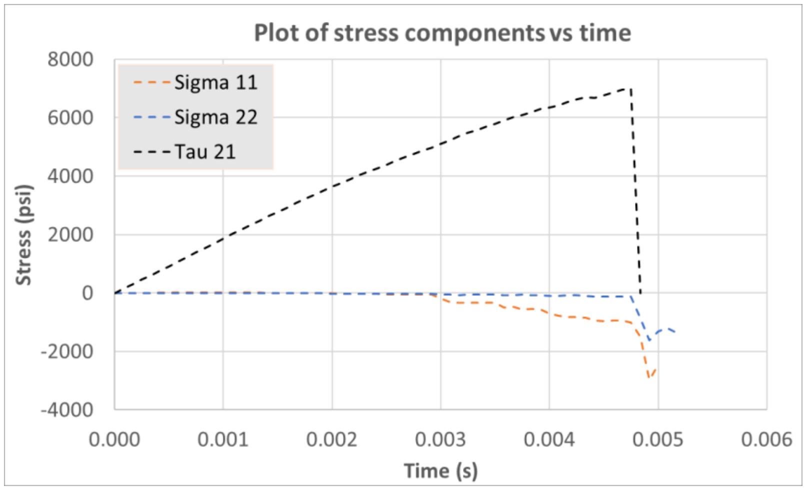

Figure 4.39. Plot of stress components versus time for 2-1 plane shear test

Discussion: The nonlinear behavior of the 2-1 plane shear test is predicted accurately. The peak stress and ultimate strain are slightly underpredicted.

4.7.3. VALIDATION OF OUT-OF-PLANE TESTS

The validation of the two-dimensional (2D) model, referred to as S2-S3 model, for transverse normal loading, and S2-S23 model for out-of-plane shear loading, were carried out by comparing the simulation response to the experimental tests of the composite T800S/F3900 in (Khaled, et al., 2018). The simulated tests are 2-direction tension, 2-direction compression and 2-3 plane shear tests.

First, the effect of the window size is investigated. This is followed by mesh sensitivity analysis and finally, the effect of the gauge section is determined. The results from these investigations are used to select the model parameters for use in 2-3 plane biaxial tests discussed in chapter 5.

4.7.3.1. EFFECT OF WINDOW SIZE

Three window sizes are investigated in this section - nine (9), twenty-five (25) and forty-nine (49) RUC models shown earlier in section 4.4. Each model is subjected to

2-direction tension, 2-direction compression and 2-3 plane shear loadings. The computed response is compared to that of the three-dimensional model (S1-S2 model) discussed in section 4.7.1. The entire model was used as the gauge section.

S2-S3 MODEL UNIAXIAL TENSION IN 2-DIRECTION

Model: The three 2D models with 9, 25 and 49 RUC are used in this test. The boundary conditions are applied as explained in section 4.5.

Results: The stress-strain response in figure 4.40 does not show significant difference between the response of the various window sizes. However, there is a slight increase in the stiffness compared to the experimental values at higher strain values.

Discussion: The initial elastic modulus is accurately predicted by all window sizes. The 49 RUC gives better strength and ultimate strain prediction compared to other window sizes. Moreover, the experimental model does not satisfy the plane strain assumption, this explains why there is stiffness mismatch at higher strain values.

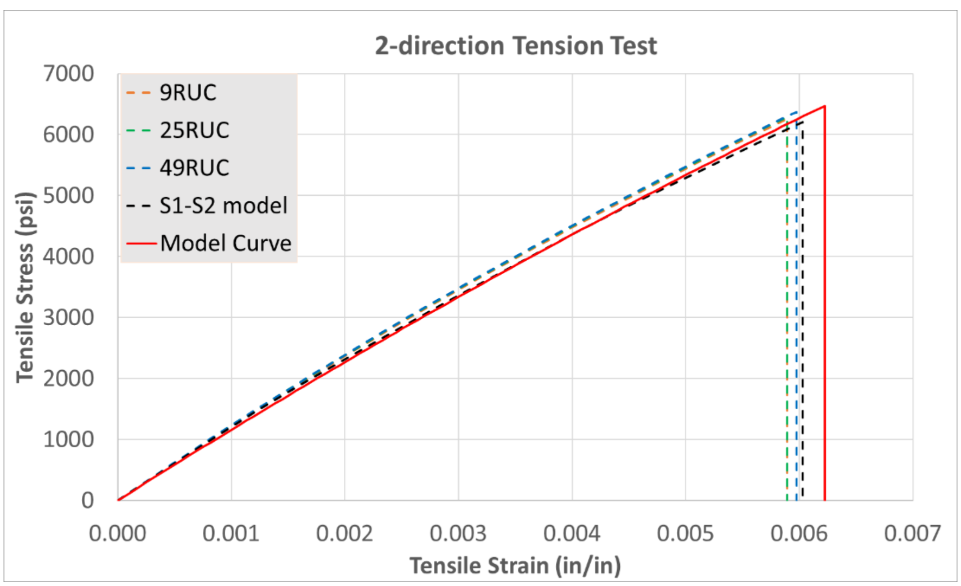

Figure 4.40. Stress-strain response for 2D model under uniaxial tension: Effect of window size

S2-S3 MODEL UNIAXIAL COMPRESSION IN 2-DIRECTION

Model: The boundary conditions applied to the models are as shown in section 4.5.

Results: The stress-strain response (figure 4.41) shows less than 1% difference between the peak stress and ultimate strain values with varying window sizes. There is however a difference between the maximum stress and strain at failure between the three-dimensional model (S1-S2 model) and the S2-S3 model.

Discussion: The 2-direction compression experiment does not satisfy plane strain assumption; this explains the softer response of 2D models compared to S1-S2 model and the model curve. The calibration of the effective plastic strain at failure was done on solid elements, which have a different element formulation that plane strain elements. This explains why 2D models underpredict the peak stress and ultimate strain.

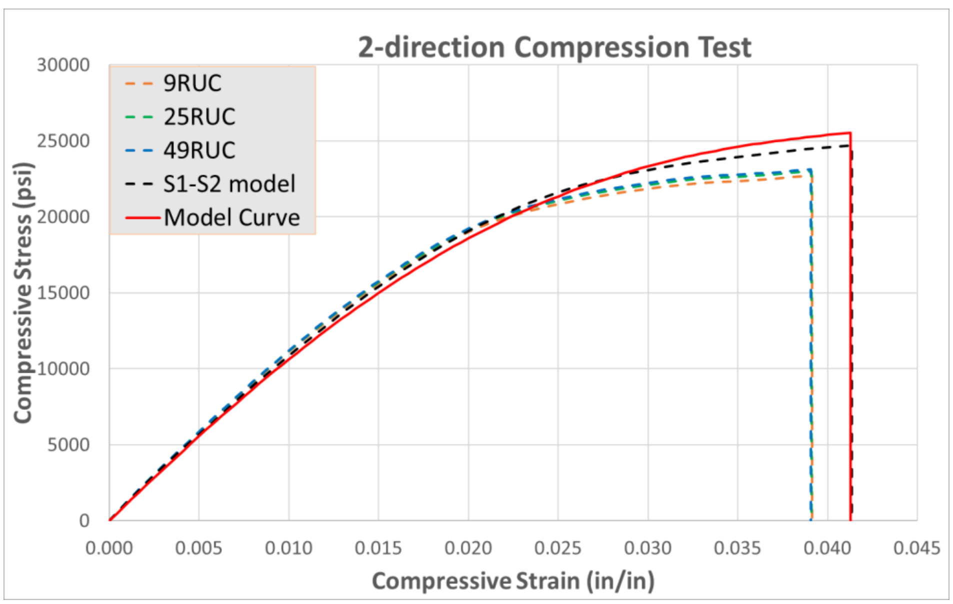

Figure 4.41. Stress-strain response for S2-S3 model under uniaxial compression: Effect of window size

S2-S23 MODEL 2-3 PLANE SHEAR

Model: The displacement boundary conditions are applied to produce a pure shear deformation as shown in figure 4.23.

Results: The computed responses (figure 4.42) show small differences in the peak stress and ultimate strain values between the three models. The initial stiffness predictions agree well with the experimental result.

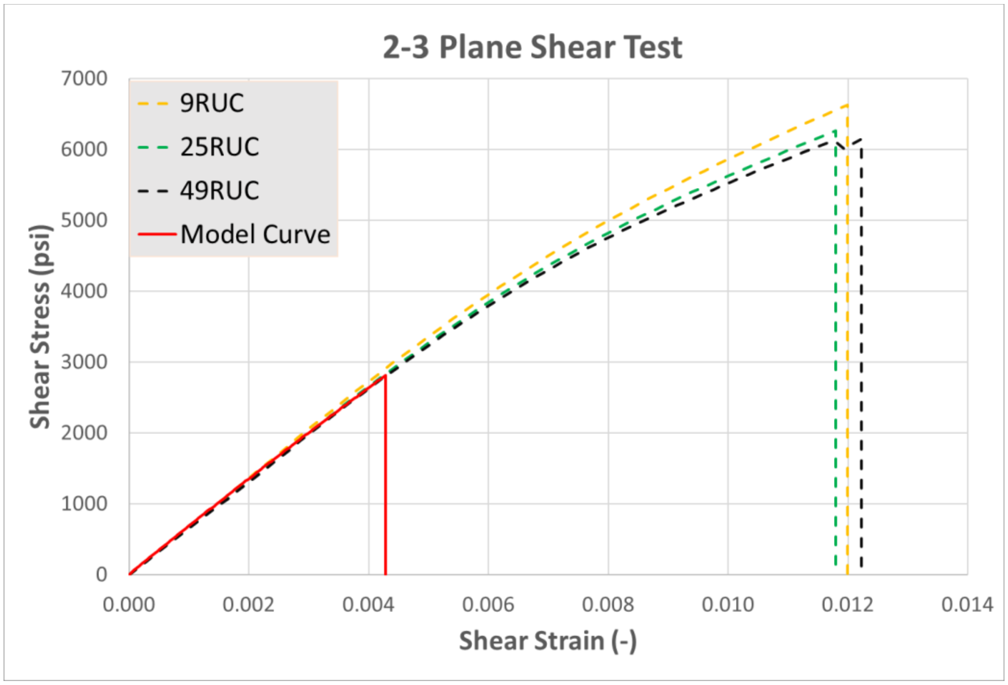

Figure 4.42. Stress-strain response for S2-S23 model under 2-3 plane shear: Effect of window size

Discussion: From the three tests carried out above, the 49-RUC shows gives better strength and ultimate strain predictions that the other window sizes under transverse tension (figure 4.40) while there is no difference in strength and ultimate strain prediction under transverse compression (figure 4.41) . A converging trend of peak strength is seen with increasing window size under 2-3 plane shear. Therefore, the 49-RUC window size is used in all subsequent models.

4.7.3.2. EFFECT OF MESH DENSITY

The next effect considered is that of element size, i.e., mesh density on the strength prediction. Three different mesh sizes were generated with the 49-RUC model. These meshes are referred to as Coarse mesh (figure 4.43(a)), Medium mesh (figure 4.43(b)) and Fine mesh (figure 4.43(c)).

The details of each mesh are shown in table 4.7. Each of the three meshes is subjected to 2-direction tension, 2-direction compression and 2-3 plane shear tests. The model with the best response is then used in all subsequent tests.

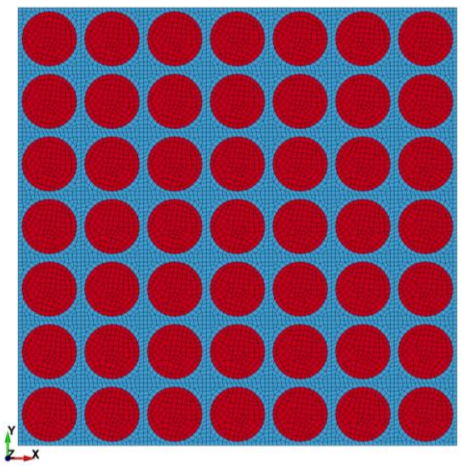

(a)

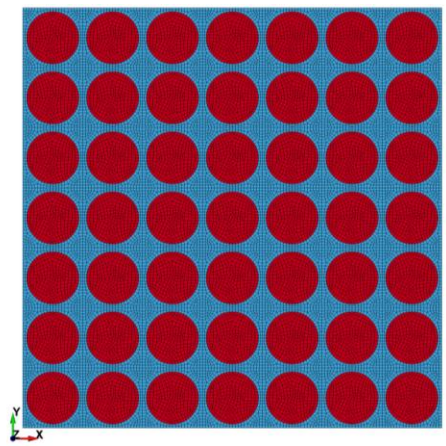

(b)

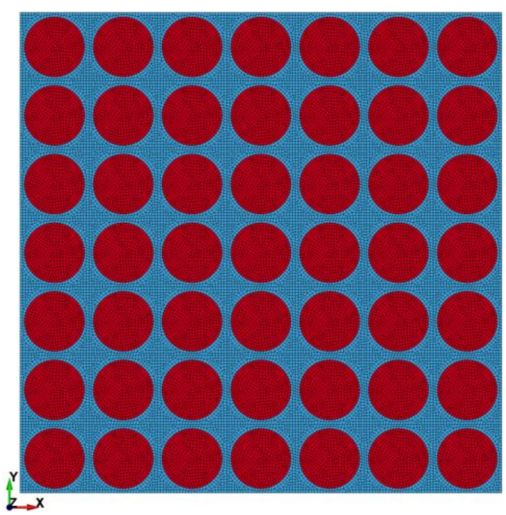

(c)

Figure 4.43. (a) Coarse mesh (b) Medium mesh (c) Fine mesh

Table 4.7. Details of coarse, medium and fine mesh sizes

	Coarse	**Medium**	**Fine**
# Elements	9555	20531	31164
# Nodes	10185	21093	32214
Max. Aspect Ratio	2.05	1.74	1.71
Min. Aspect Ratio	1.06	1.03	1.02

S2-S3 MODEL UNIAXIAL TENSION IN 2-DIRECTION

Model: Three mesh densities are compared in this test. These are shown in figure 4.43. The boundary conditions are as explained in section 4.5.

Results: The response of the three models are very close to each other. There is insignificant difference in the peak stress and ultimate strain as shown in figure 4.44. The failed specimens in figure 4.45 show a similar crack pattern. The crack develops perpendicular to the loading direction (x-direction or 2-direction).

Discussion: The response is mesh independent and is also close to the response computed in the S1-S2 model. The effect of the characteristic element size on the response was reduced by the element characteristic length versus effective plastic Poisson's ratio input curve into the matrix material model (table 3.5).

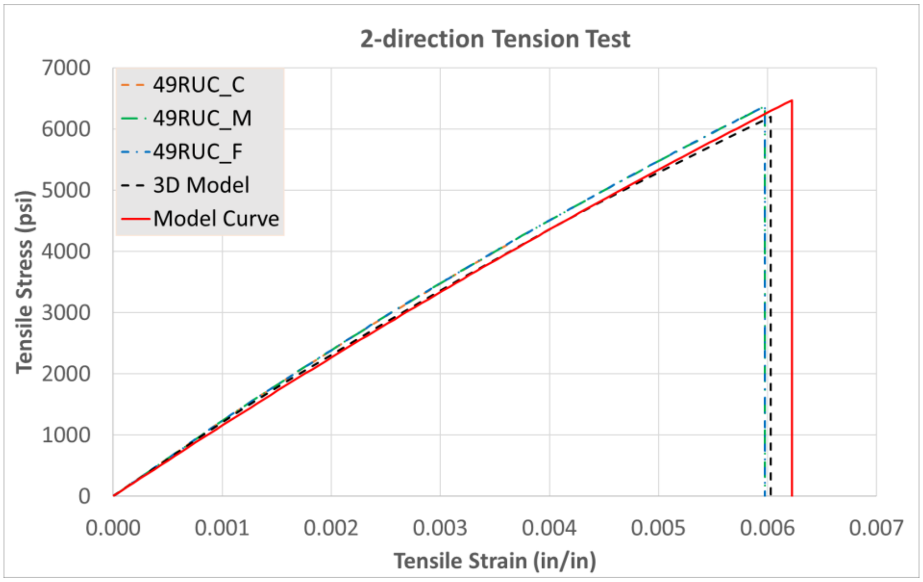

Figure 4.44. Stress-strain response for S2-S3 model under uniaxial tension: Effect of mesh density

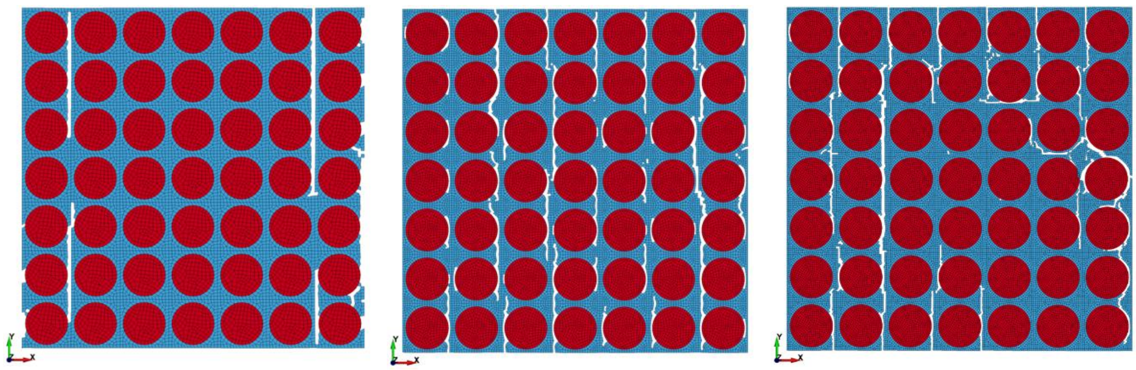

(a) (b) (c)

Figure 4.45. Failed specimen under uniaxial tension (a) Coarse mesh (b) Medium mesh (c) Fine mesh.

<u>S2-S3 MODEL UNIAXIAL COMPRESSION IN 2-DIRECTION</u>

<u>Model:</u> Similar to the 2-direction tension test models, the three mesh densities are investigated in this section under compressive loading. The displacement boundary conditions are as shown in section 4.5.

Result: The compression response in figure 4.46 shows dependence on mesh density – as the mesh gets finer, the peak stress and the ultimate strain reduce. The crack patterns shown in figure 4.47 are different. The coarse mesh shows predominantly vertical cracks while the medium mesh in figure 4.47(b) shows significant crack development along the diagonal of the model. The fine mesh shows a random distribution of cracks.

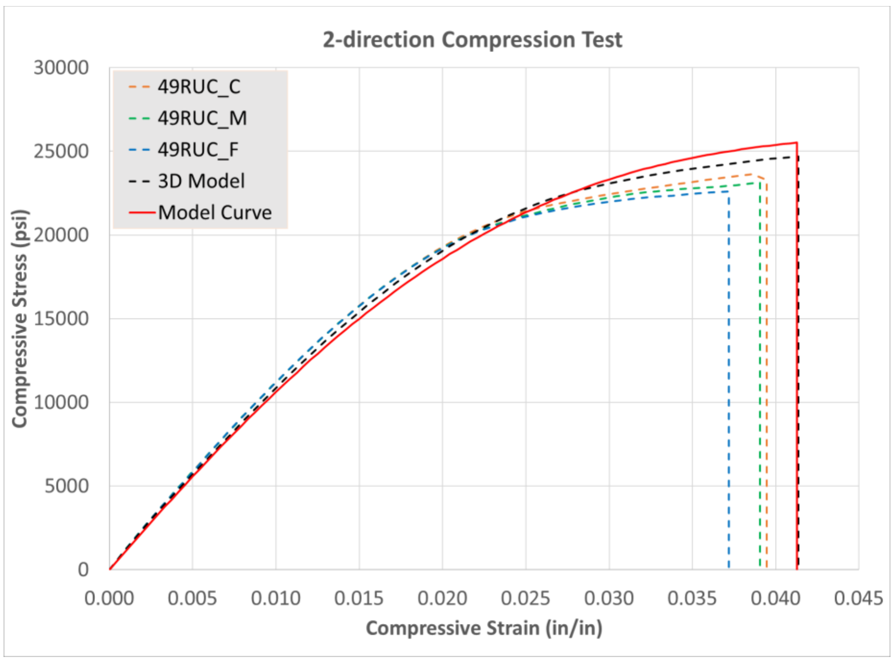

Figure 4.46. Stress-strain response for S2-S3 model under uniaxial compression: Effect of mesh density

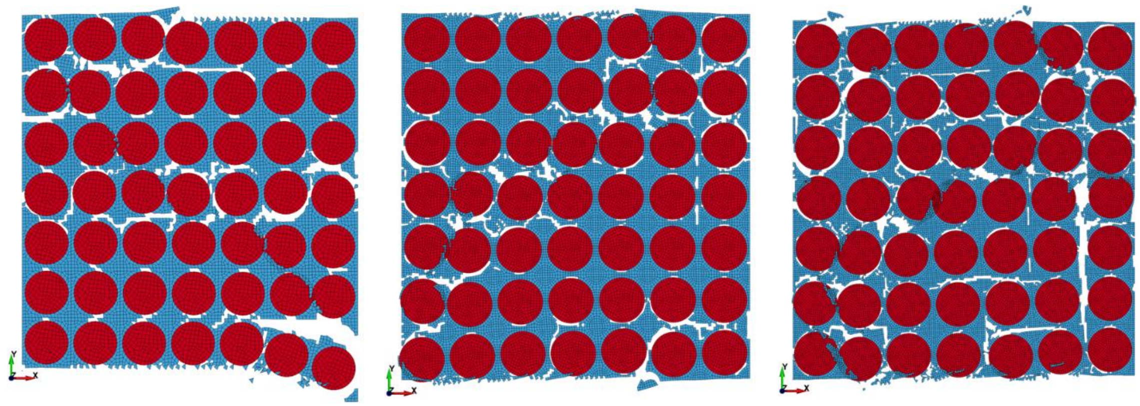

(a) (b) (c)

Figure 4.47. Failed specimen under uniaxial compression (a) coarse mesh (b) medium mesh (c) fine mesh

<u>Discussion</u>: The results show that the three peak stress and ultimate strain values are within 4% and 5% of each other, respectively. Again, it should be noted that the matrix material parameters were calibrated using 3D models (Khaled, et al., 2021).

<u>S2-S23 MODEL 2-3 PLANE SHEAR</u>

<u>Model</u>: The S2-S23 model with various mesh densities shown in figure 4.43 is investigated in this test. The boundary conditions are as shown in section 4.5.

<u>Results</u>: The response shown in figure 4.48 is mesh dependent. However, a clear converging trend with increasing mesh density can be seen. The failed specimens in figure 4.49 show substantial failure at the boundary. The medium mesh in figure 4.49(b) shows failure only at the top and right boundary while the fine mesh shows failure at the left and bottom boundaries.

<u>Discussion</u>: Results show that (a) the tensile response is not mesh sensitive, and (b) the compressive and shear responses show some mesh dependence with the compressive response giving better predictions with a coarser mesh while the shear response shows

convergence trend with finer meshes. In light of these findings, the medium mesh size is used subsequently to check the effect of the gauge size on the homogenized response.

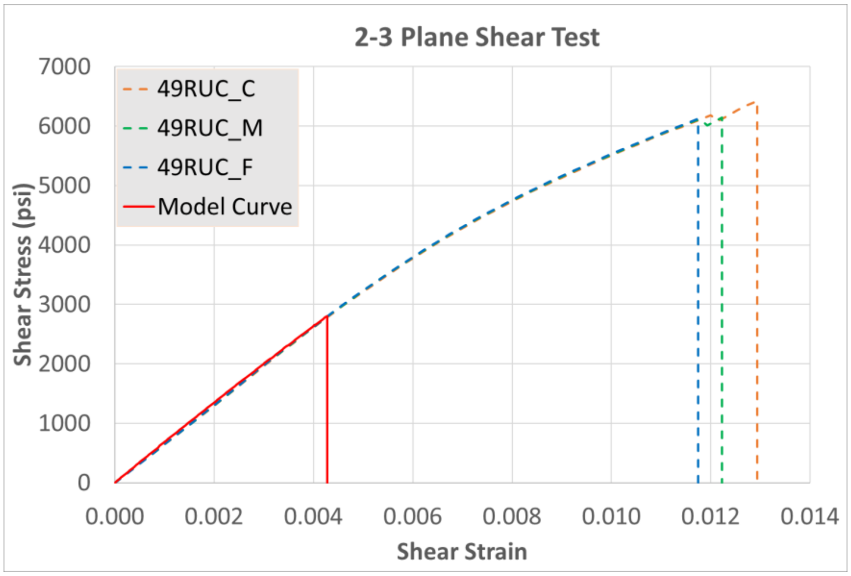

Figure 4.48. Stress-strain response for S2-S23 model under 2-3 plane shear: Effect of mesh density

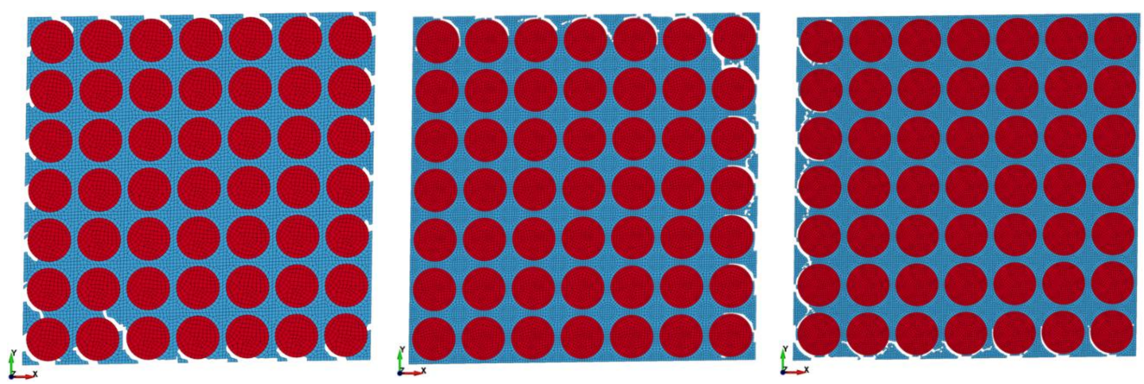

(a) (b) (c)

Figure 4.49. Failed specimen under 2-3 plane (a) Coarse mesh (b) Medium mesh (c) Fine mesh

4.7.3.3. EFFECT OF THE GAUGE SECTION

Finally, the effect of the gauge section is examined. Three gauge section sizes were considered in this study. The large gauge section shown in figure 4.50 covers the entire model. The medium gauge section covers the inner 25-RUC and the small gauge section covers the innermost 9-RUC. The response of this model under 2-direction tension, 2-direction compression and 2-3 plane shear tests is examined next.

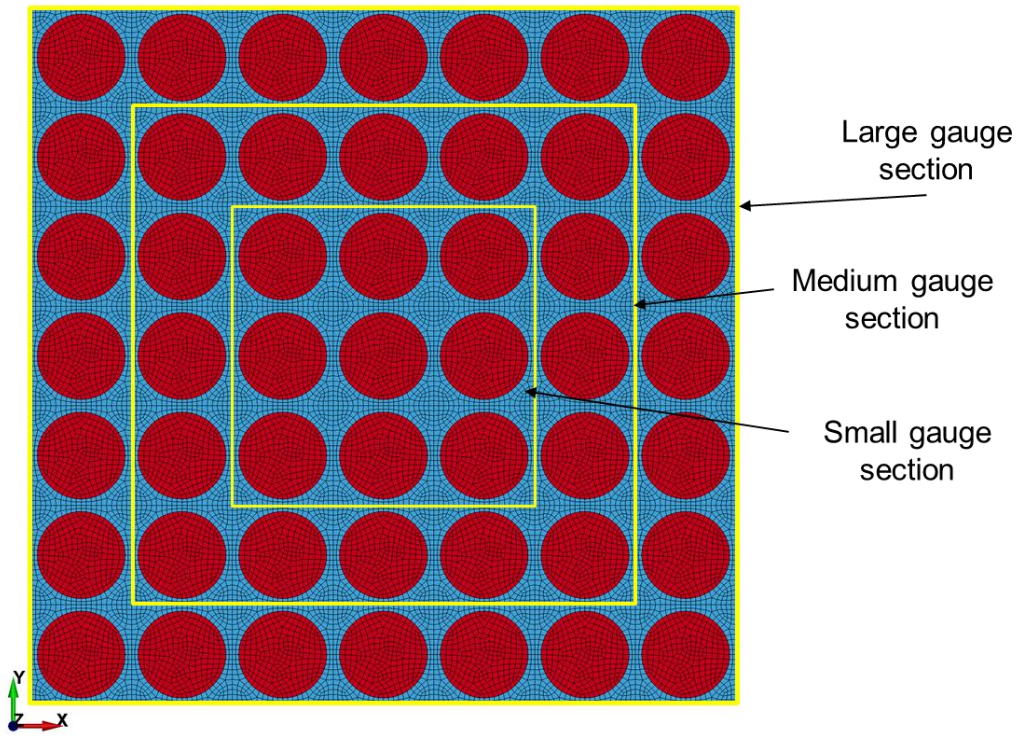

Figure 4.50. Gauge section sizes

S2-S3 MODEL 2-DIRECTION TENSION

Model: The S2-S3 model with the medium mesh size is used in this test. The boundary conditions described in section 4.5 are used to prescribe the motion applied to the boundary nodes.

Results: The tensile response in figure 4.51 shows no significant difference in the peak stress and ultimate strains for the three gauge section sizes.

Discussion: The uniform stress distribution in the model tied to uniform boundary conditions causes the model to have similar homogenized response under transverse tension regardless of the size of the gauge section.

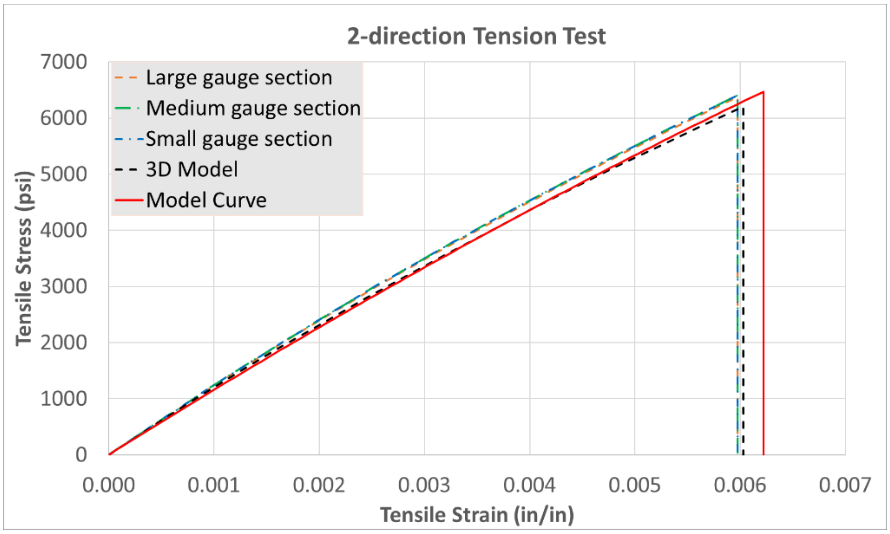

Figure 4.51. Stress-strain response for S2-S3 model under uniaxial tension: Effect of gauge section

<u>S2-S3 MODEL 2-DIRECTION COMPRESSION</u>

<u>Model</u>: Once again, the S2-S3 model with the medium mesh is used in this test. The boundary conditions described in section 4.5 are applied to the model.

<u>Results:</u> The peak stress and ultimate strain predictions are not affected by the size of the gauge section (figure 4.52). The x-stress component, along the loading direction, is uniformly distributed over the entire model as shown in figure 4.53.

<u>Discussion</u>: The stress and strain at failure show virtually no sensitivity to gauge section size.

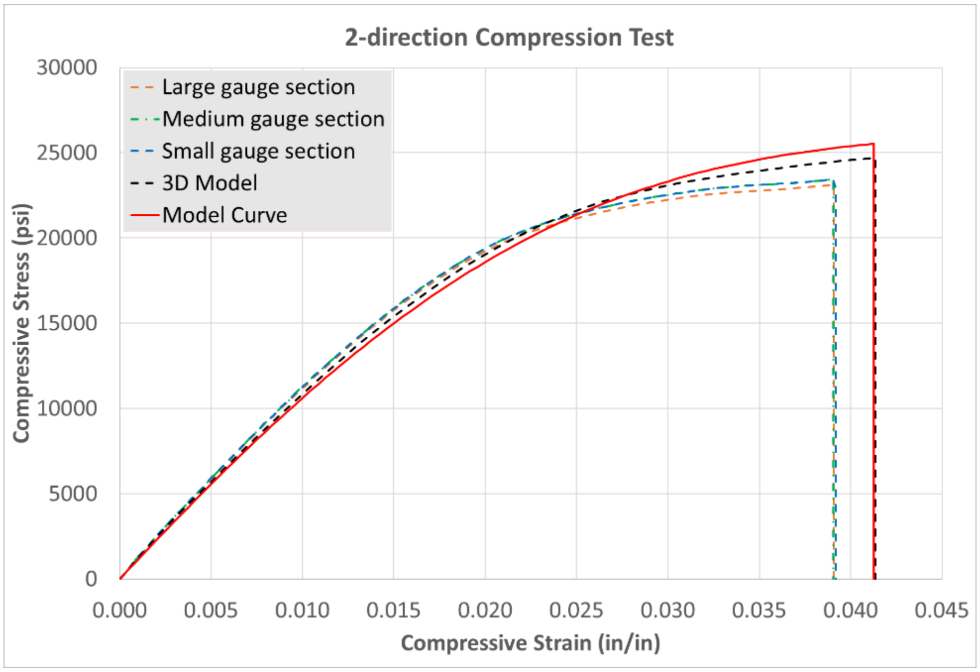

Figure 4.52. Stress-strain response for S2-S3 model under uniaxial tension: Effect of gauge section

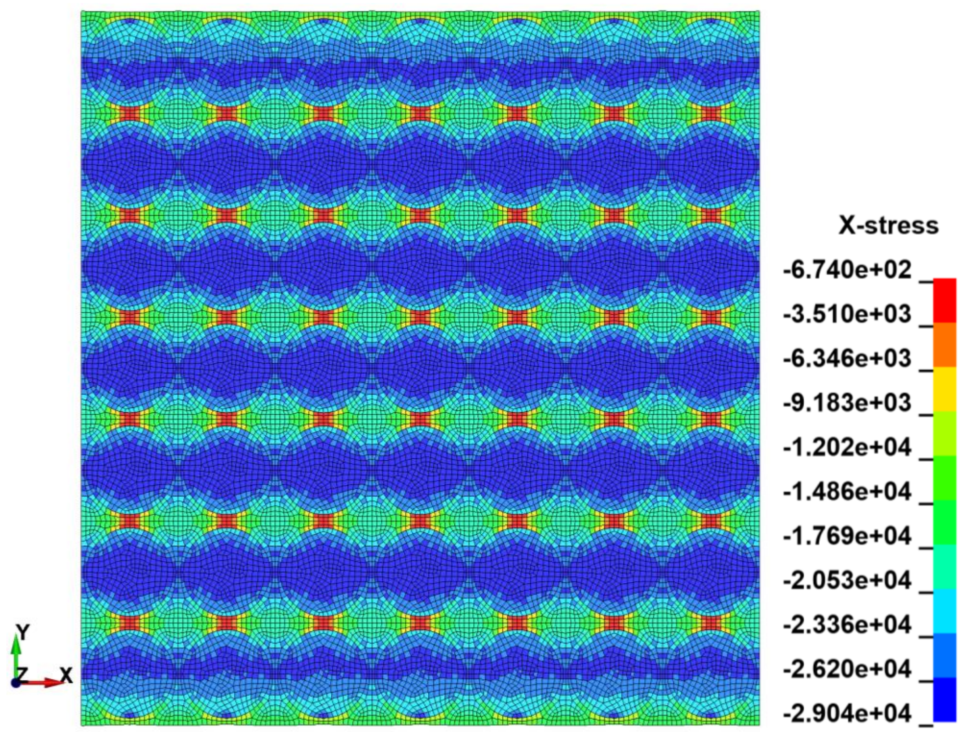

Figure 4.53. X stress distribution

S2-S23 MODEL 2-3 PLANE SHEAR

Model: The S2-S23 model is used in this test. The boundary conditions are applied as described in section 4.5.

Results: The shear stress prediction of the large gauge section is stiffer at higher strain values than that of the Medium and Small gauge sections as shown in figure 4.54. This is because the shear stresses are larger close to the boundary as can be seen in figure 4.55.

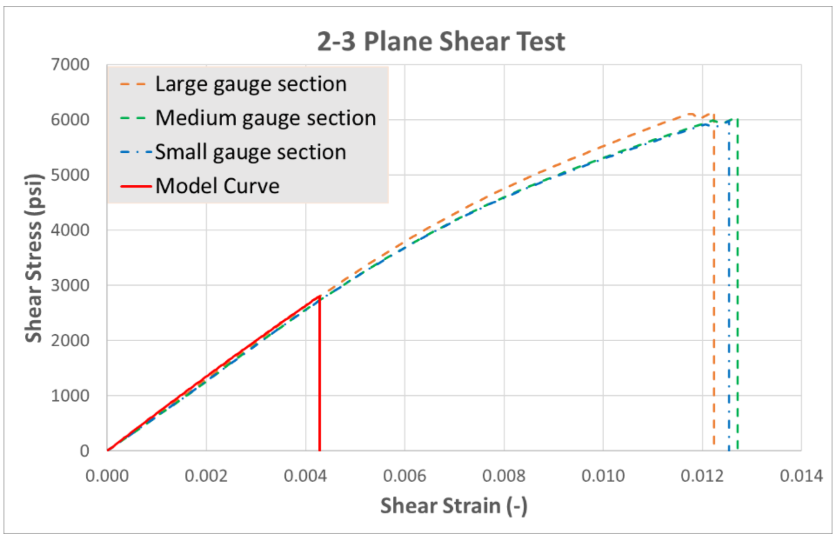

Figure 4.54. Stress-strain response for S2-S23 model under 2-3 plane shear: Effect of gauge section

Discussion: The large gauge section gave stiffer shear stress prediction than the medium and small gauge sections. This indicates a convergence of the shear response with decreasing size of the gauge section. Therefore, the medium gauge section, which covers the inner 25-RUC, is used as the region of interest for post-processing in all subsequent simulations.

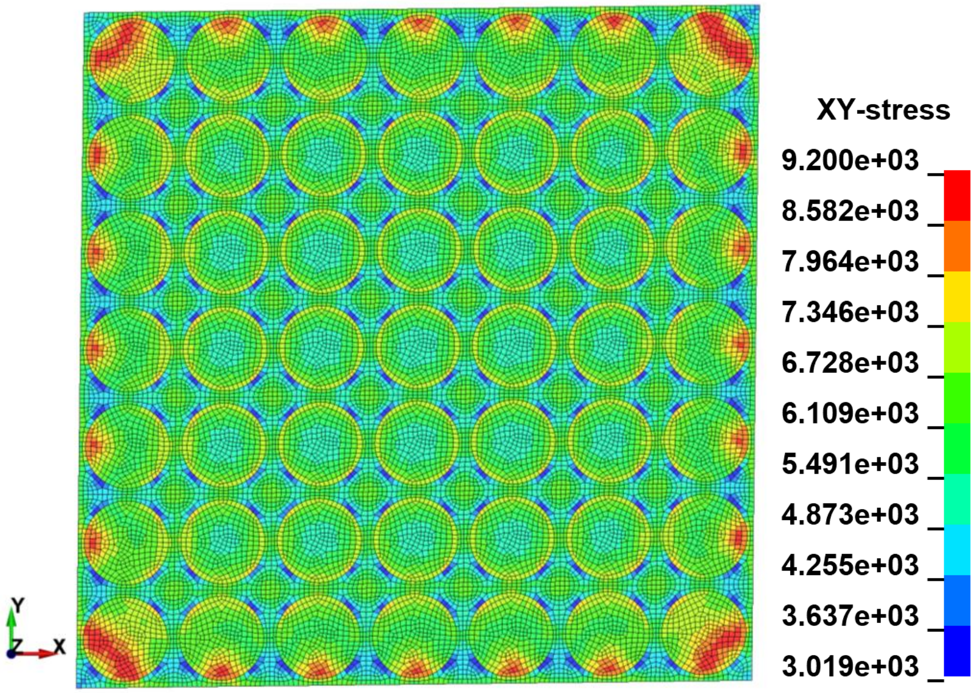

Figure 4.55. XY stress distribution

5. BIAXIAL TEST RESULTS

Unidirectional fiber-reinforced composites fail in various modes based on the loading and the structural geometry. However, the focus in this chapter is creating a large number of data points that lie on the failure surface of unidirectional composites. Detection of failure in unidirectional composites can be split into in-plane state of stress dominated failure and out-of-plane state of stress failure. In this chapter, test specimens are created and subjected to biaxial states of stress. All non-zero stress components are recorded as part of the failure data. The point cloud is thus formed with no limitation imposed on the dimension of the stress space it covers.

The biaxial tests covered herein include biaxial tension in the 1-direction and 2-direction, biaxial tension in the 1-direction and compression in the 2-direction, biaxial compression in the 1-direction and tension in the 2-direction, and biaxial compression in the 1- and 2-directions. These tests are performed on the S1-S2 model. The S2-S21 model is subjected to biaxial 2-direction tension and 2-1 plane shear, 2-direction compression and 2-1 plane shear. The failure surface for each the tests mentioned above is plotted in the corresponding two-dimensional stress space alongside side Puck and Tsai-Wu failure criteria.

The biaxial tests performed on the S2-S3 and S2-S23 model include the combination of transverse loading, namely biaxial tension in the 2- and 3-directions, biaxial tension in the 2-direction and compression in the 3-direction, biaxial compression in the 2-direction and tension in the 3-direction, biaxial compression in the 2- and 3-directions, biaxial tension in the 2-direction and 2-3 plane shear, and finally, biaxial compression in the 2-direction and 2-3 plane shear. The summary of all biaxial tests as well as short names that refer to them is shown in table 5.1.

Table 5.1. Summary of biaxial tests

Test	Short name	Model
1-direction tension – 2-direction tension	T1T2	S1-S2
2-direction tension – 2-direction compression	T1C2	S1-S2
1-direction compression – 2-direction tension	C1T2	S1-S2
1-direction compression – 2-direction compression	C1C2	S1-S2
2-direction tension – 2-3 plane shear	T2S21	S2-S21
2-direction compression – 2-3 plane shear	C2S21	S2-S21
2-direction tension – 3-direction tension	T2T3	S2-S3
2-direction tension – 3-direction compression	T2C3	S2-S3
2-direction compression – 3-direction tension	C2T3	S2-S3
2-direction compression – 3-direction compression	C2C3	S2-S3
2-direction tension – 2-3 plane shear	T2S23	S2-S23
2-direction compression – 2-3 plane shear	C2S23	S2-S23

Both in-plane and out-of-plane data are to be used simultaneously as a failure data in a point cloud failure criterion. The need to separate the loading into in-plane and out-of-plane arises from the challenges in applying multiaxial states of stress on a composite.

In this chapter, the details of each test are presented, the failure modes are explained, and details of the failed specimens are discussed. Failure surfaces are plotted in the corresponding stress space followed by a point cloud representation of the data. Finally, the point cloud failure surface data are presented and the challenges for generating more data are discussed.

5.1. BIAXIAL TESTS ON IN-PLANE MODELS

The in-plane model in this case refers to the three-dimensional S1-S2 and S2-S21 models. The stress components that are non-zero for in-plane biaxial loading include the longitudinal stress σ_1, the transverse stress σ_2 and the in-plane shear stress τ_{21}.

5.1.1. FAILURE DATA IN THE $\sigma_1 - \sigma_2$ SPACE

In the $\sigma_1 - \sigma_2$ stress space, the loading was applied through prescribed motion at different rates in the 1- and 2-directions. The loading was applied simultaneously. In the sections that follow, the results for all stress combinations are presented and discussed.

<u>BIAXIAL 1-DIRECTION TENSION AND 2-DIRECTION TENSION (T1T2) TEST</u>

<u>Model</u>: The S1-S2 model was used for this test. The biaxial loading 1- and 2-direction tension is achieved through simultaneous application of displacement boundary conditions in the positive z and y direction (1- and 2-directions) shown in figure 4.12a and 4.13a. The fixity conditions in the model remain the same as that from uniaxial loading.

<u>Results</u>: The stress vs time curve in figure 5.1(a) shows loss of load carrying capacity in the 2-direction while the composite still has load carrying capacity in the 1-direction. The failed specimen in figure 5.1(b) shows matrix failure, there is no fiber failure.

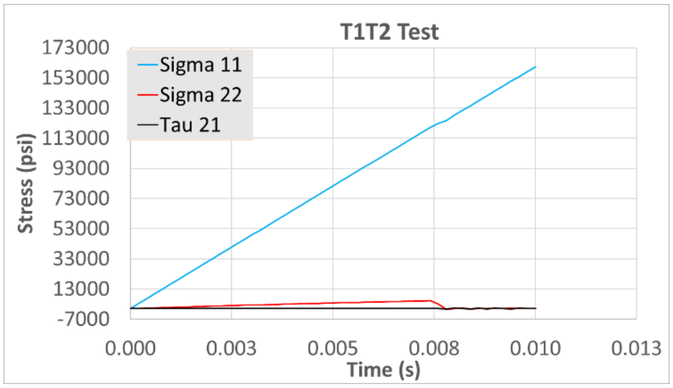

(a)

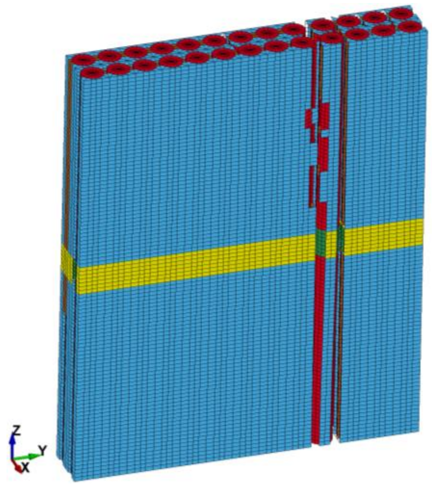

(b)

Figure 5.1. T1T2 test (a) Stress vs time curve (b) failed specimen

Discussion: The transverse tension is the principal failure mode in this test. The strength of the composite in the transverse tension is two-order of magnitude less than that in the longitudinal direction. The shear stress is zero, this is because the boundary conditions are applied to produce a biaxial normal state of stress.

BIAXIAL 1-DIRECTION TENSION AND 2-DIRECTION COMPRESSION (T1C2) TEST

Model: The S1-S2 model presented in section 4.2 and validated in section 4.7.1 is used in this test. The boundary conditions are similar to those in the T1T2 tests with the displacement in the 2-direction being applied in the negative 2-direction.

Results: The stress versus time curve in figure 5.2(a) shows loss of load carrying capacity in both the 1- and 2-direction. This means both the fiber and the matrix failed as shown in figure 5.2(b).

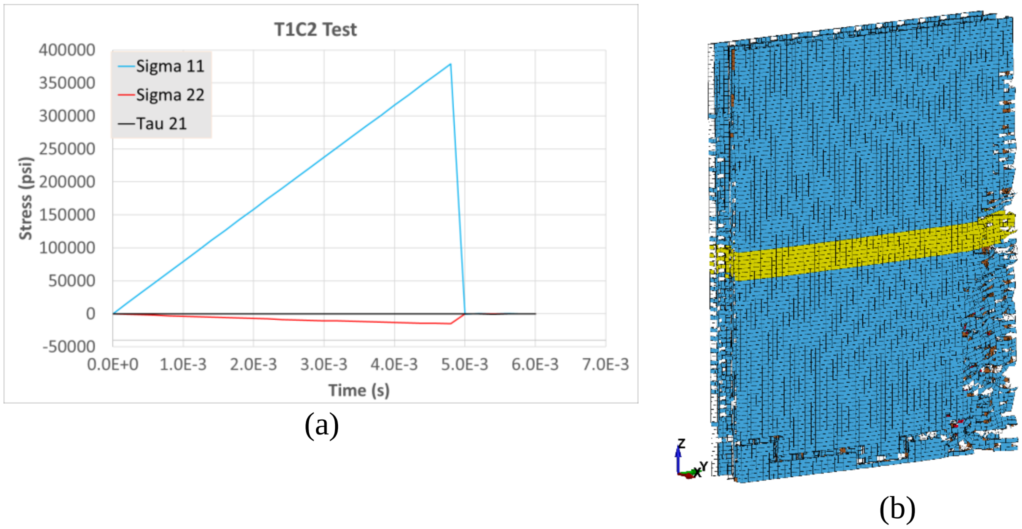

Figure 5.2. T1C2 test fiber-matrix failure. (a) Stress vs time curve (b) failed specimen

In contrast to the failure mode above, the stress vs time in curve 5.3(a) shows loss of load carrying capacity in the 2-direction while there is no failure in the fiber. This is a matrix dominated failure as shown in figure 5.3(b).

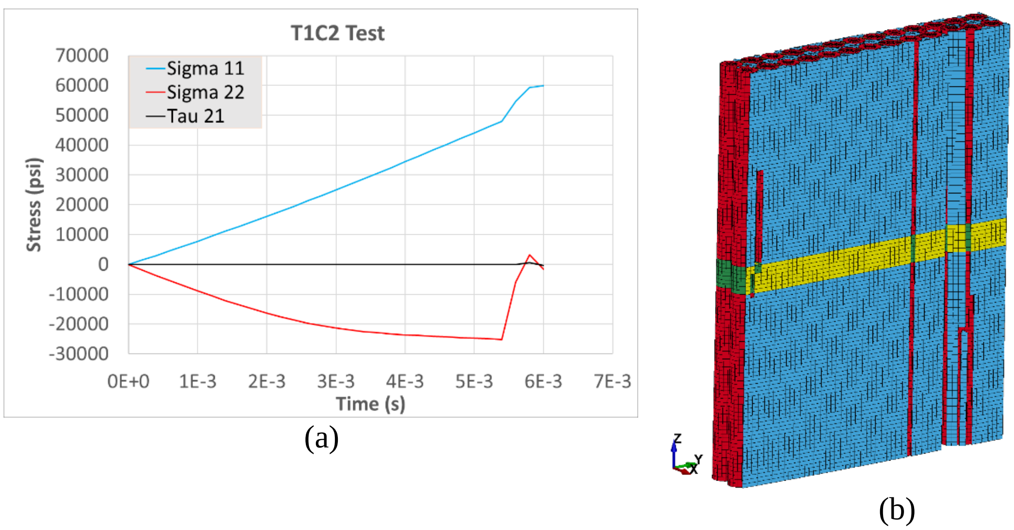

Figure 5.3. T1C2 test matrix dominated failure. (a) Stress vs time curve (b) failed specimen

<u>Discussions:</u> In the 1-direction tension dominated failure, the both the fiber and matrix fail. This because after fiber elements are deleted from the model, the void created in the

model causes an increase in stress in the matrix which in turns leads to matrix element getting eroded.

BIAXIAL 1-DIRECTION COMPRESSION AND 2-DIRECTION TENSION (C1T2) TEST

Model: Similar to the T1C2 test above, the S1-S2 model is used in this test. The boundary conditions are applied as shown in section 4.3.

Results: The failure mode in this test involves both the fiber and the matrix since there is loss of load carrying capacity in all directions as shown in figure 5.4(a) and 5.4(b).

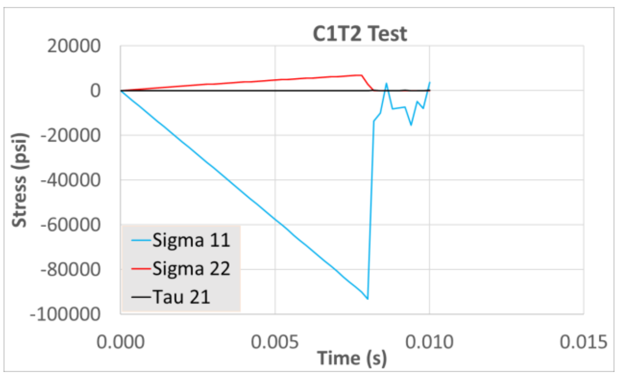

(a)

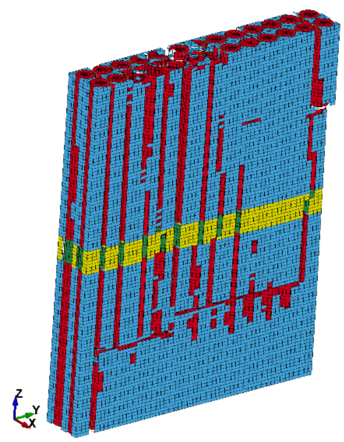

(b)

Figure 5.4. C1T2 test fiber-matrix failure. (a) Stress vs time curve (b) failed specimen

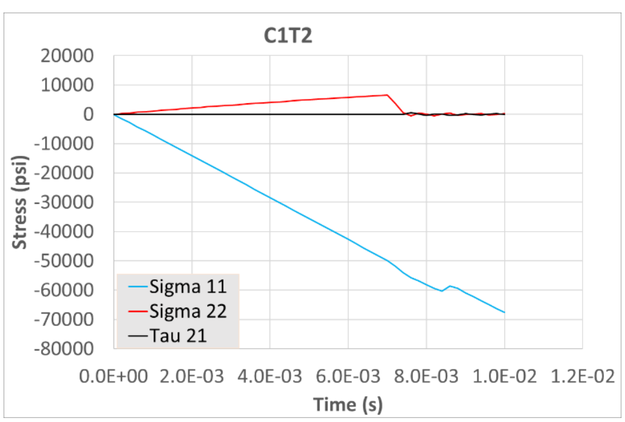

(a)

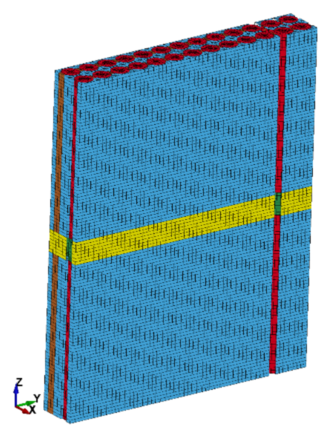

(b)

Figure 5.5. C1T2 test matrix dominated failure. (a) Stress vs time curve (b) failed specimen

The failure shown in figure 5.5(a) shows failure only in the 2-direction, therefore it is a matrix dominated failure as seen in figure 5.5(b).

Discussion: The fiber failure under longitudinal compression leads to matrix failure in the under transverse tension. This is because the model is set up such that the fiber carries most of the longitudinal stress. After fiber element get eroded in the simulation, the stress redistribution causes matrix elements carry higher stresses which in turn causes them to fail (get eroded). In the transverse tension dominated failure mode, there is no fiber failure. The specimen loses its transverse strength before its longitudinal compressive strength.

BIAXIAL 1-DIRECTION COMPRESSION AND 2-DIRECTION COMPRESSION (C1C2) TEST

Model: The S1-S2 model is used in this test. The boundary conditions are applied as shown in figure 4.13.

Results: The failure patterns in this test shows both fiber and matrix failure. In figure 5.6(a), the stress in both the 1- and 2-directions drops sharply. Figure 5.6(b) shows the failed specimen where a visible crack splits the model into pieces. The fiber failure in figure 5.6(c) shows a similar pattern as the visible matrix failure in figure 5.6(b).

Discussion: The biaxial compression tests shows that the model is squashed; it fails in both directions.

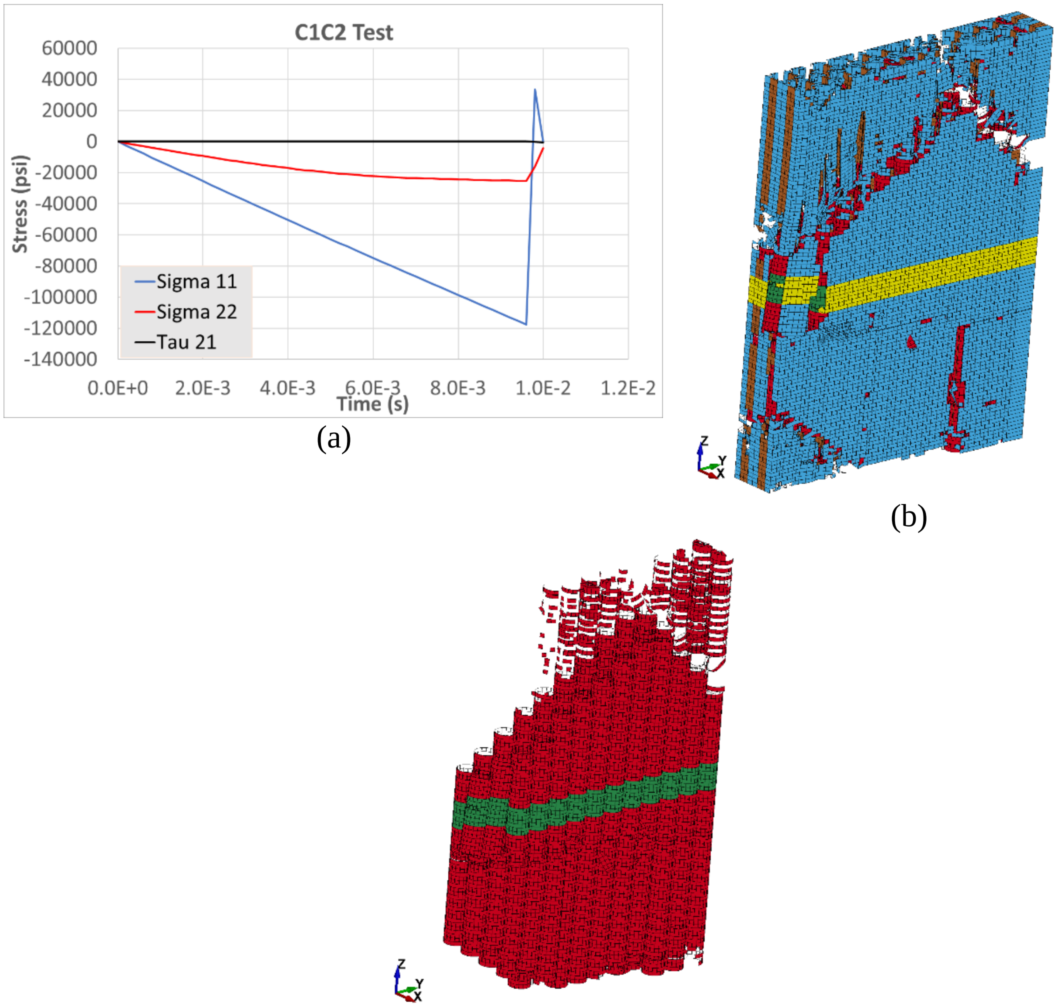

Figure 5.6. C1C2 test fiber-matrix failure. (a) Stress vs time curve (b) failed specimen (c) fiber failure

FAILURE SURFACE IN THE $\sigma_1 - \sigma_2$ SPACE

Results and discussion

The failure surface was plotted in the two-dimensional space since only two stress components are non-zero. In figure 5.7, the virtual test data which correspond to the point cloud are shown in blue, while the point in red correspond to those from validated tests in chapter 4. Puck and Tsai-Wu failure criterion were also plotted on the same figure to allow for visual comparison between the various failure surface. The input values for plotting Puck and Tsai-Wu failure criteria as shown in figure 5.7 based on equations 2.1-2.4 and 2.15 respectively are given in table 5.2. From figure 5.7, the virtual test failure prediction agrees with puck failure criterion. Tsai-Wu failure criterion overlaps with Puck and virtual test data, but it extends beyond maximum stresses in all direction, thus suggesting that under biaxial tension test and biaxial compression test, the composite longitudinal and transverse strengths increase.

The virtual test data also indicate the failure modes for each point. There are four failure modes distinguished, namely fiber failure (F), matrix failure (M), fiber dominated failure in conjunction with matrix failure (FM) and matrix dominated failure in conjunction with fiber failure (MF). In the biaxial tension test, failure is matrix dominated, there is no fiber failure while in other tests, there are portions with both fiber and matrix failure. There is a decreasing transverse strength in tension and compression under increasing longitudinal stress. This is the effect of stress in the 1-direction on stress in the 2-direction.

Table 5.2. Input parameter for plotting Puck and Tsai-Wu failure criteria in the $\sigma_1 - \sigma_2$ space

Parameter	**Input value**	**Source**
X_T	366097 psi	(Khaled, et al., 2018)
X_C	105766 psi	(Khaled, et al., 2018)
Y_T	6471 psi	(Khaled, et al., 2018)
Y_C	25530 psi	(Khaled, et al., 2018)
ν_{12}	0.0168	(Khaled, et al., 2018)
ν_{f12}	0.01125	Table 3.1

$m_{f\sigma}$	1.1	(Puck & Schürmann, 1998)
E_{f1}	$4.27(10^7)$ psi	Table 3.1
E_1	$2.35\ (10^7)$ psi	(Khaled, et al., 2018)

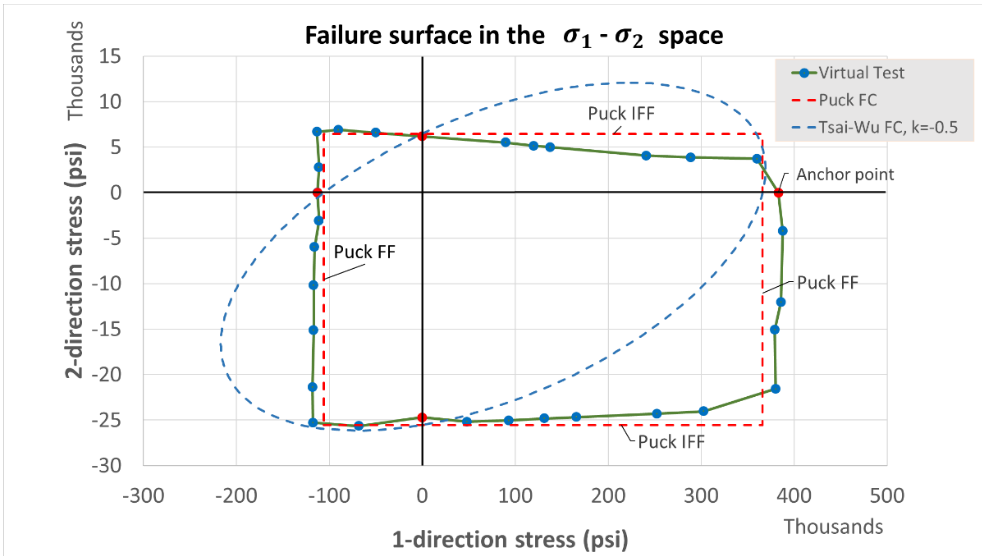

Figure 5.7. Failure surface $\sigma_1 - \sigma_2$ stress space

5.1.2. FAILURE DATA IN THE $\sigma_2 - \tau_{21}$ SPACE

The failure surface in the $\sigma_2 - \tau_{21}$ space is generated using the S2-S21 model. The loading in the 2-direction as well as shear loading are applied simultaneously for tension and compression dominated failure while in shear dominated failure, shear motion is prescribed first before transverse motion is prescribed so as to reduce the effect of normal stress on shear stress predictions.

<u>BIAXIAL 2-DIRECTION TENSION AND 2-1 PLANE SHEAR (T2S21) TEST</u>

<u>Model: </u>The S2-S1 model is used for this test. The uniform displacement boundary condition described in section 4.5 are applied simultaneously with the boundary conditions in figure 4.16.

Results: The stress vs time curve in figure 5.8(a) shows loss of load carrying capacity in all three-direction. The longitudinal stress component is minimal compared to other stress components. The failed specimen in figure 5.8(b) shows failure at the left boundary as well as in the notch section of the specimen.

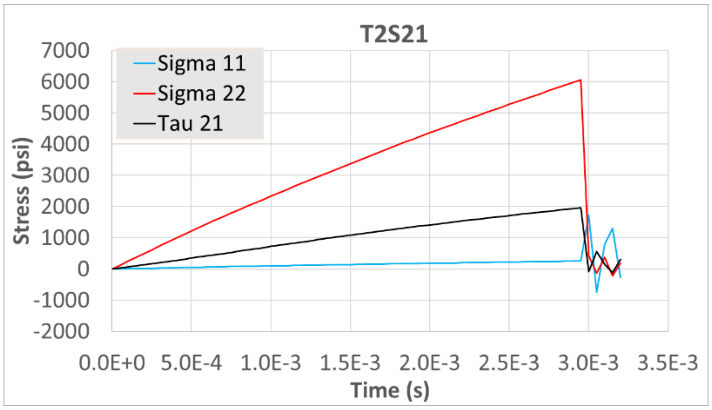

(a)

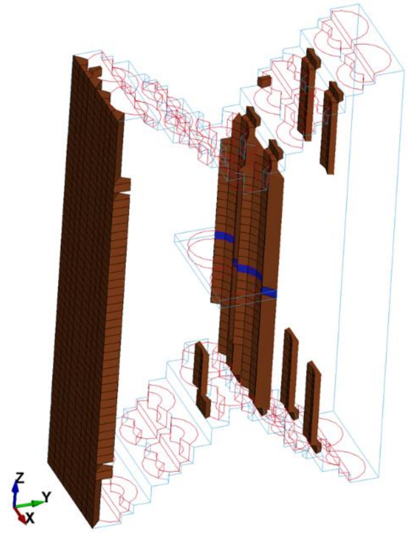

(b)

Figure 5.8. T2S21 test, tension dominated failure. (a) Stress vs time curve (b) failed specimen

Discussion: The crack in the middle of the model coupled with the erosion of elements on the left face causes loss of load carrying capacity. This is a transverse tension dominated failure. Transverse loading decreases shear strength, causing the model to fail at a lower shear strength than in a pure in-plane shear test case.

BIAXIAL 2-DIRECTION COMPRESSION AND 2-1 PLANE SHEAR (C2S21) TEST

Model: The S2-S21 model is used in this test to simulate the biaxial 2-direction compression and in-plane shear test. The boundary conditions are applied in two different ways. Firstly, in in-plane shear dominated failure modes, the shear loading is applied first followed by transverse compression loading. Secondly, in transverse compression dominated failure modes, both in-plane shear and transverse compression loading are applied simultaneously.

Results: The stress versus time curve in figure 5.9. shows loss of load carrying capacity in all directions. However, upon application of transverse loading, the longitudinal stress increases substantially; this is also caused by the initiation in the notch as shown in figure 5.9(b). The loss of load carrying capacity occurs when the element across the depth of the model in the notch get eroded (figure 5.9(c)). This is a shear dominated failure mode.

Figure 5.10(a) shows a compression dominated mode where both loading are applied simultaneously. The nonlinear behavior of the matrix can be seen in the response curve. The longitudinal stress component remains low, it does not increase substantially. The failed specimen in figure 5.10(b) shows eroded elements in the notch section, which is appropriate for this model.

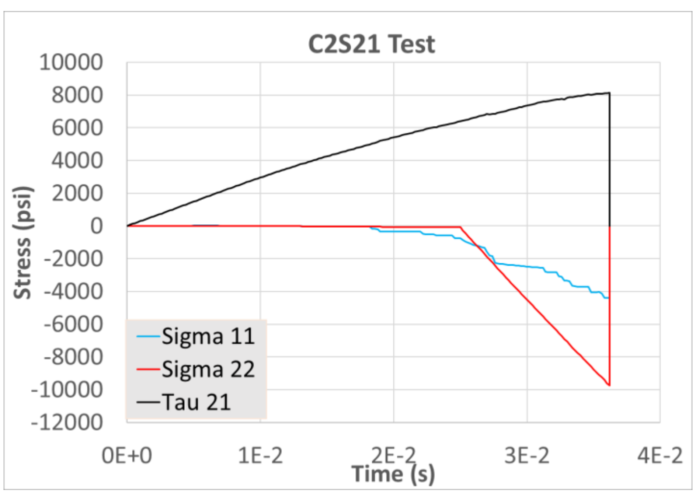

(a)

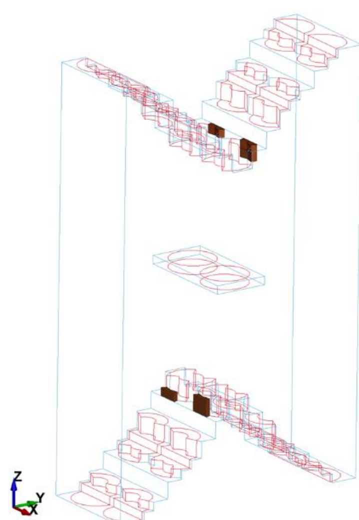

(b)

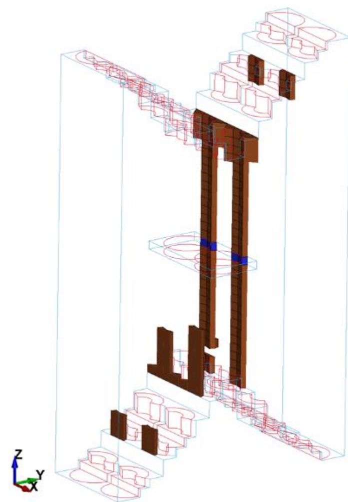

(c)

Figure 5.9. C2S21 test, shear dominated failure. (a) Stress vs time curve (b) failed specimen at failure initiation (c) failed specimen at final failure

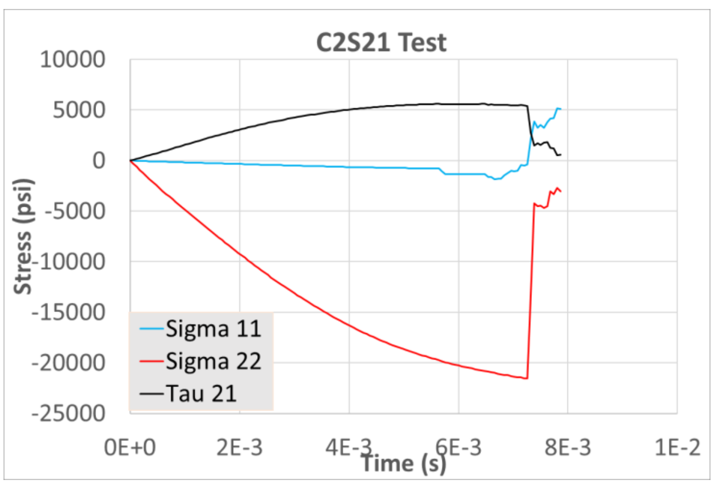

(a)

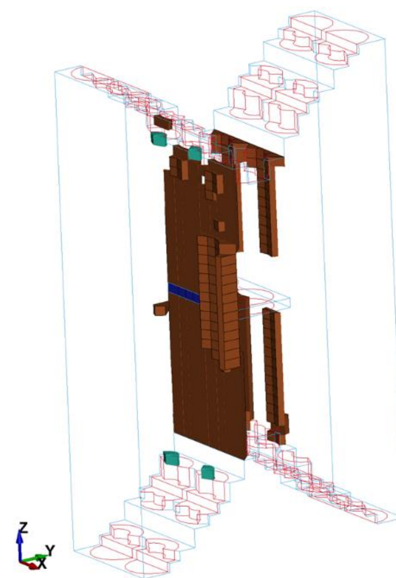

(b)

Figure 5.10. C2S21 test, compression dominated failure. (a) Stress vs time curve (b) failed specimen

<u>Discussion:</u> The transverse compressive stress increases the shear strength. In this biaxial loading, the model failed at a higher shear strength that a pure shear case. The transverse compressive loading is applied after in-plane shear loading in shear dominated failure so as to reduce the effect of the uniform boundary condition on the shear stress in the model,

which gives better response with loading applied only on the right face of the S2-S21 model.

FAILURE SURFACE IN THE $\sigma_2 - \tau_{21}$ SPACE

Results and discussion

The failure surface in the $\sigma_2 - \tau_{21}$ stress space shown in figure 5.11 compares the strength predictions from virtual test with that from Puck and Tsai-Wu failure criteria. The input values for plotting Puck and Tsai-Wu failure criteria according to equations 2.5-2.7 and 2.16 respectively are shown in table 5.3. The virtual test strength prediction in the tension dominated region agrees well with both Puck and Tsai-Wu. However, a conservative prediction is shown in the shear and compression dominated region; this is because the S2-S21 model underpredicts compressive strength of the composite.

Table 5.3. Input parameter for plotting Puck and Tsai-Wu failure criteria in the $\sigma_2 - \tau_{21}$ space

Parameter	Input value	Source
$R_{\perp}^{(+)}\ (Y_T)$	6471 psi	(Khaled, et al., 2018)
$R_{\perp}^{(-)}\ (Y_C)$	25530 psi	(Khaled, et al., 2018)
$R_{\perp\parallel}\ (S_{21})$	7280 psi	(Khaled, et al., 2018)
$p_{\perp\parallel}^{(+)}$	0.35	(Puck, et al., 2002)
$p_{\perp\parallel}^{(-)}$	0.3	(Puck, et al., 2002)
$p_{\perp\perp}^{(-)}$	0.38	Computed from eq. 2.11

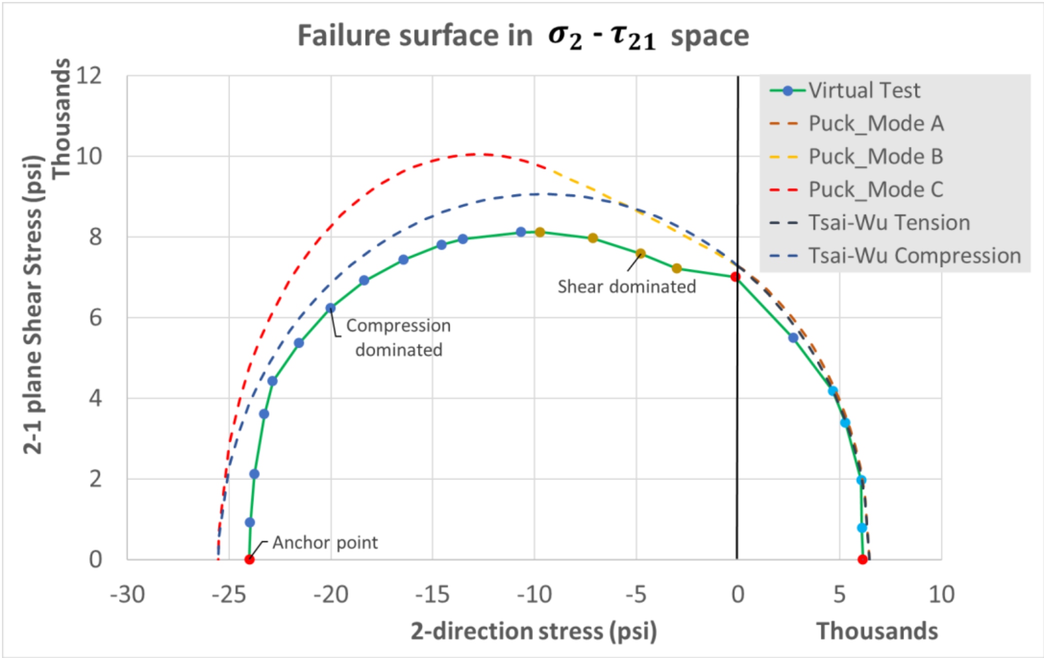

Figure 5.11. Failure surface $\sigma_2 - \tau_{21}$ stress space

The point cloud representation in figure 5.12 is a three-dimensional plot of all stresses at failure for in-plane loading.

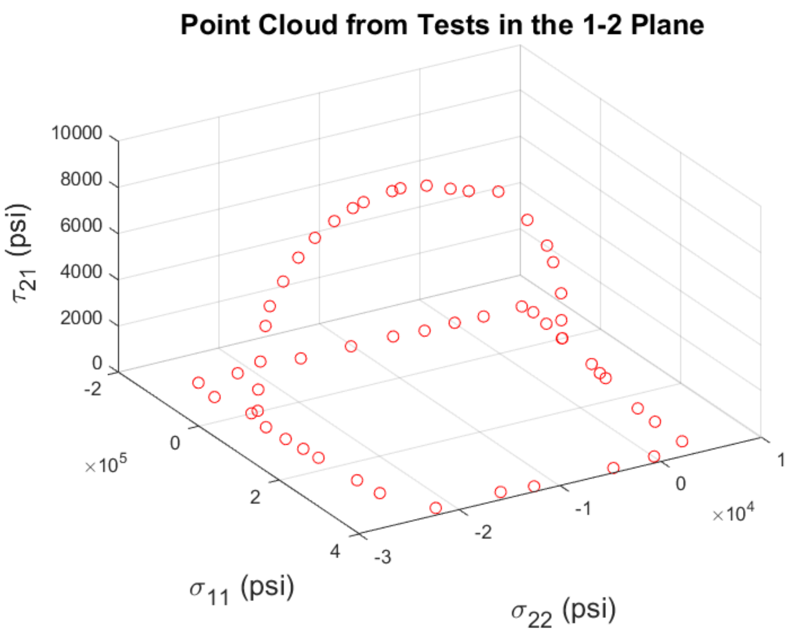

Figure 5.12. Point cloud representation of failure points in the 1-2 plane

5.2. BIAXIAL TESTS ON OUT-OF-PLANE MODEL

The out-of-plane biaxial test are carried out on the two-dimensional model referred to as S2-S3 and S2-S23 model (depending on whether it is subjected to only normal loading or normal and shear loading) validated in chapter 4. The loading is applied according to equations 4.4 and 4.5. In the following section, the result for biaxial loading in the transverse direction are shown. The failed specimens are presented and discussed for selected tests in each combination. The failure surfaces in the $\sigma_2 - \sigma_3$ and $\sigma_2 - \tau_{23}$ spaces are plotted followed by the point cloud representation of the failure data.

5.2.1. FAILURE DATA IN THE $\sigma_2 - \sigma_3$ SPACE

<u>BIAXIAL 2-DIRECTION TENSION AND 3-DIRECTION TENSION (T2T3) TEST</u>

<u>Model</u>: The S2-S3 model with medium mesh is used in this test. The uniform boundary conditions are applied simultaneously in both the 2- and 3-directions.

<u>Results</u>: The stress vs time curve in figure 5.13(a) shows loss of load carrying capacity in all direction. The shear stress component is zero throughout the simulation. The longitudinal stress component is non-zero in this case due to plane strain formulation. The failed specimen in figure 5.13(b) shows the crack develop both in the vertical and horizontal directions since the loading is also applied in both directions.

<u>Discussion</u>: In transverse tensile loading, cracks develop in a perpendicular to the loading direction. In a biaxial transverse tension loading, cracks develop in directions perpendicular to the 2 loading directions as seen in figure 5.13.

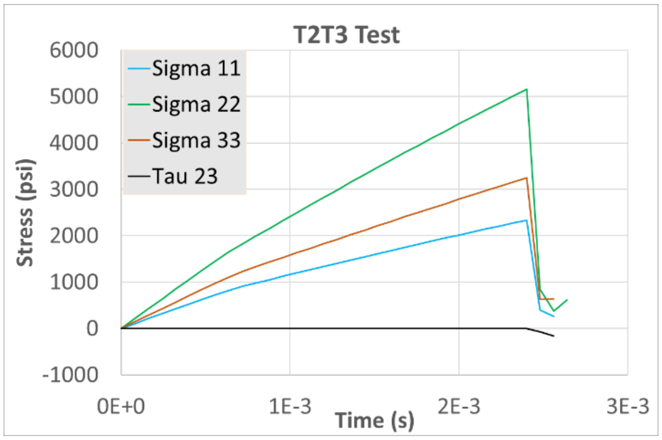

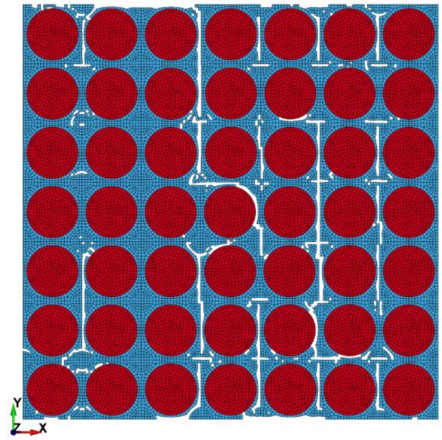

(a) (b)

Figure 5.13. T2T3 test (a) Stress vs time curve (b) failed specimen

BIAXIAL 2-DIRECTION TENSION AND 3-DIRECTION TENSION (T2C3) TEST

Model: Similar to the T2T3 test, the S2-S3 model is used in this test. The Boundary conditions are applied as explained in section 4.5.

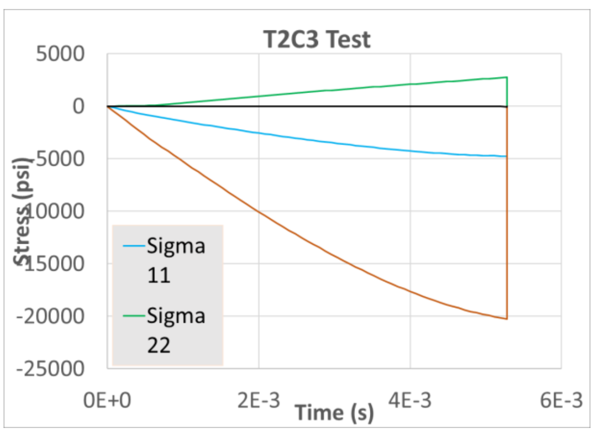

(a)

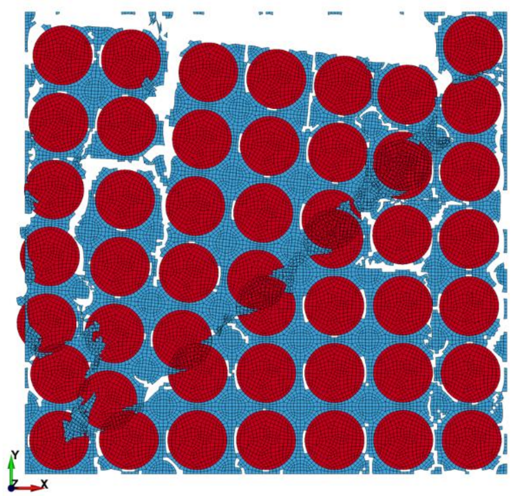

(b)

Figure 5.14. T2C3 test (a) Stress vs time curve (b) failed specimen

Results: Figure 5.14(a) shows loss of load carrying capacity in all directions. The nonlinear behavior in the 3-direction is shown in the response. The failed specimen in figure 5.14(b) shows the model being squashed and a crack diagonal to the specimen is visible.

Discussion: The fiber and matrix elements penetrate each other because no contact was defined in the model. The stress recorded at that time step were not of any use to this study. Post-processing was stopped after the peak stress was reached.

BIAXIAL 2-DIRECTION TENSION AND 3-DIRECTION TENSION (C2T3) TEST

Model: The S2-S3 model is used in this test. The uniform displacement boundary conditions are applied to produce a biaxial state of stress in the model as described in section 4.5.

Results: The response in this test shown in figure 5.15(a) shows loss of load carrying capacity in all directions after peak stress. The failed specimen in figure 5.15(b) shows cracks developing throughout the model.

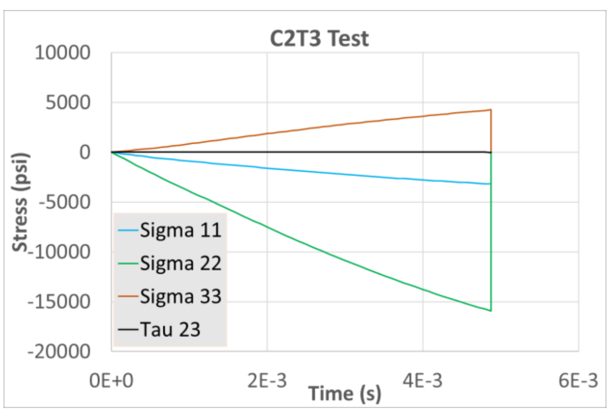

(a)

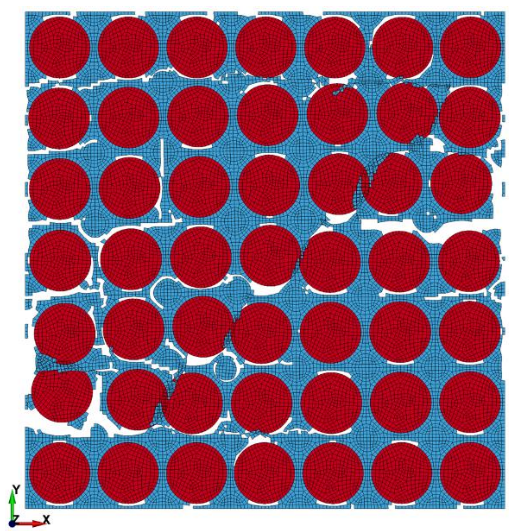

(b)

Figure 5.15. C2T3 test (a) Stress vs time curve (b) failed specimen

Discussion: Transverse compression failure mode is observed in the model, where a crack develops in the diagonal axis of the model. The element penetration is observed because contact was not defined between the fiber and the matrix.

BIAXIAL 2-DIRECTION TENSION AND 3-DIRECTION COMPRESSION (C2C3) TEST

Model: In the biaxial transverse compression test, the S2-S3 model is used. The boundary conditions are applied as described in section 4.5.

Results: The biaxial compression test result shows the nonlinear behavior of the matrix in both the 2- and 3-directions. There is loss of load carrying capacity after peak stress is exceeded as shown in figure 5.16(a) and cracks are present predominantly in the middle portion of the specimen as seen in figure 5.16(b).

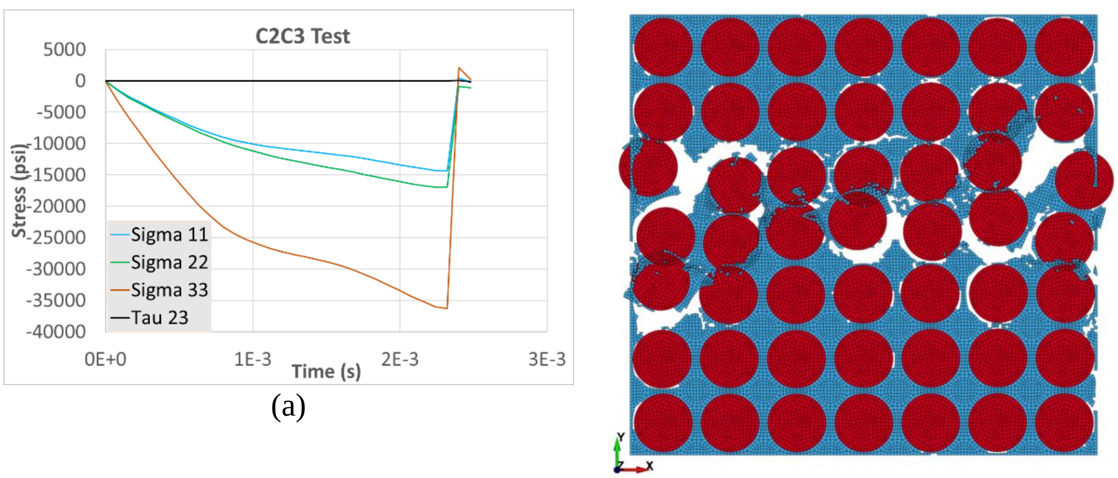

(a)

(b)

Figure 5.16. C2C3 test (a) Stress vs time curve (b) failed specimen

Discussion: This test shows biaxial transverse compression failure model. The failure is brittle.

FAILURE SURFACE IN THE $\sigma_2 - \sigma_3$ SPACE

Results and discussion

The failure surface shown in figure 5.17 shows the virtual test failure points together with Puck and Tsai-Wu failure surfaces. The latter surfaces assume that the composite does not failure under biaxial compression, which is not realistic. The input values for plotting Puck and Tsai-Wu failure criteria based on equations 2.8-2.12 and 2.17 respectively are given in table 5.4.

Table 5.4. Input parameter for plotting Puck and Tsai-Wu failure criteria in the $\sigma_2 - \sigma_3$ space

Parameter	Input value	Source
$R_{\perp}^{At}$ (Y_T)	6471 psi	(Khaled, et al., 2018)
Y_C	25530 psi	(Khaled, et al., 2018)
S_{23}	7280 psi	(Khaled, et al., 2018)
$R_{\perp\perp}^{A}$	9250 psi	Computed from eq. 2.12
$p_{\perp\perp}^{(-)} = p_{\perp\perp}$	0.38	Computed from eq. 2.11

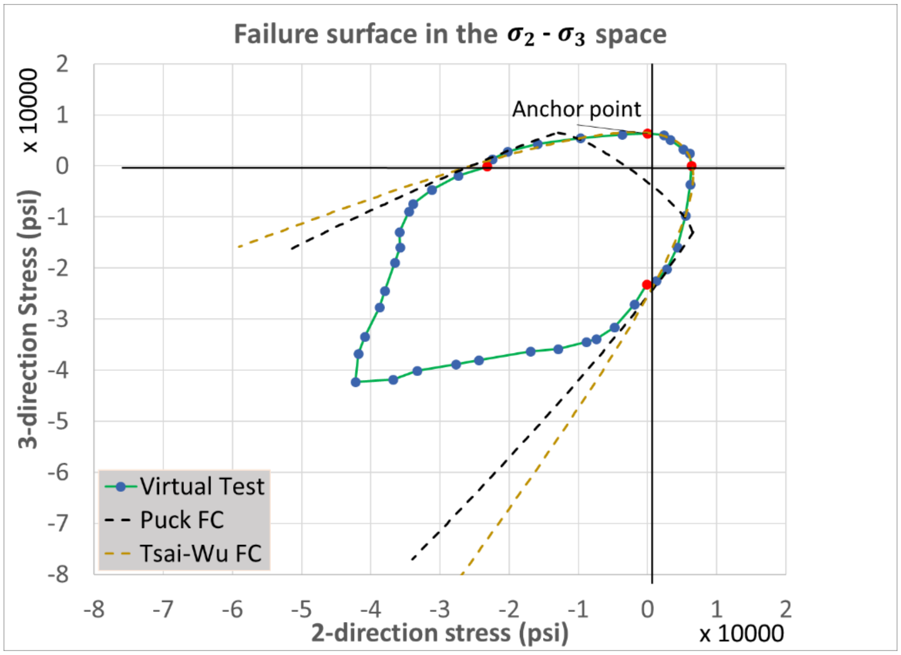

Figure 5.17. Failure surface in the $\sigma_2 - \sigma_3$ stress space

The virtual test prediction shows failure in the biaxial compression region. Virtual test predictions agree well with Tsai-Wu failure criteria. The prediction from Puck agree well in the biaxial tension compression and compression tension zone but does not give good prediction in the biaxial tension zone.

5.2.1. FAILURE DATA IN THE $\sigma_2 - \tau_{23}$ SPACE

The failure surface is generated in the $\sigma_2 - \tau_{23}$ space by applying the normal displacement in the 2-direction first then shear displacement. This seeks to minimize the normal stress component in the 3-direction during the simulation.

<u>BIAXIAL 2-DIRECTION TENSION AND 2-3 PLANE SHEAR (T2S23) TEST</u>

<u>Model</u>: Similar to the tests carried out in the $\sigma_2 - \sigma_3$ space, the S2-S23 model with medium mesh is used in this test. The transverse loading is applied first then shear loading is applied subsequently.

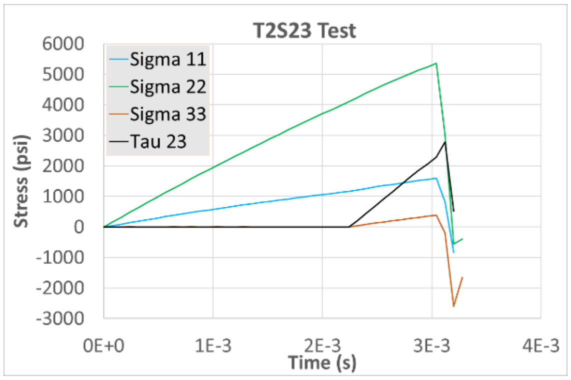

(a)

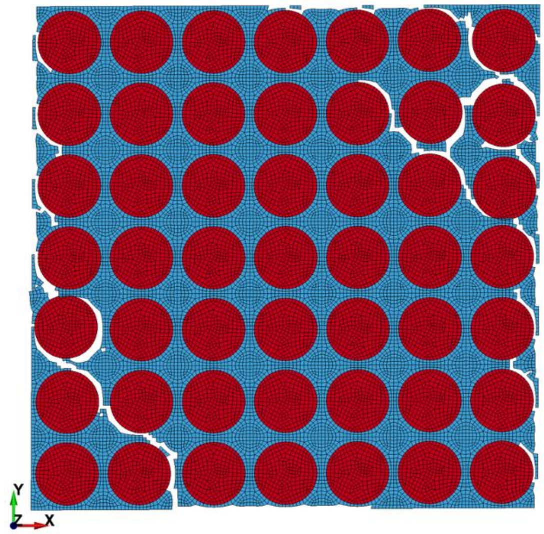

(b)

Figure 5.18. T2S23 test, tension dominated failure. (a) Stress vs time curve (b) failed specimen

<u>Results:</u> The response in shown in figure 5.18 shows loss of load carrying capacity in all directions. The 3-direction stress component is relatively low. The failed specimen in figure 5.18(b) shows the crack predominantly in the top right and bottom left section of the specimen. This is due to the presence of shear loading.

<u>Discussion:</u> The transverse tension loading reduces the compressive strength of the composite. In this test, the model failed at a lower shear strength than that of the pure shear in the 2-3 plane.

<u>BIAXIAL 2-DIRECTION TENSION AND 2-3 PLANE SHEAR (C2S23) TEST</u>

The S2-S23 model is used in this test. Analogous to the T2S23 test, the transverse compression loading is applied first followed but 2-3 plane shear loading using uniform displacement boundary conditions.

<u>Results:</u> The shear dominated response in figure 5.19(a) shows that the compressive stress drops gradually with the application of shear stress then drops sharply with the

shear stress component at failure. Horizontal cracks developed in the model at failure as seen in figure 5.19(b).

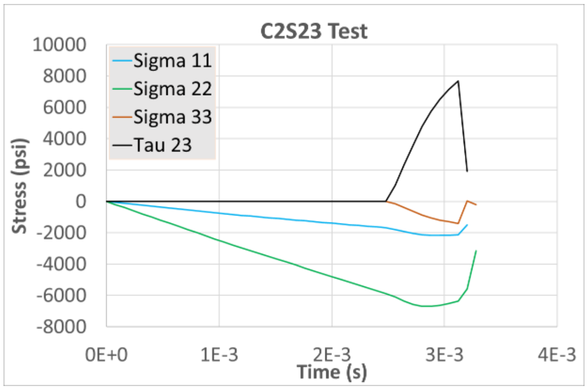

(a)

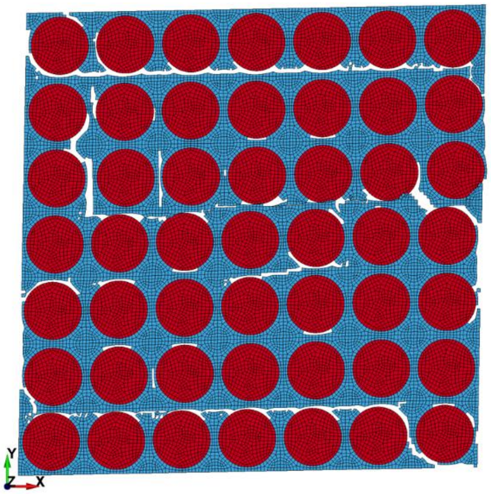

(b)

Figure 5.19. C2S23 test, shear dominated failure. (a) Stress vs time curve (b) failed specimen

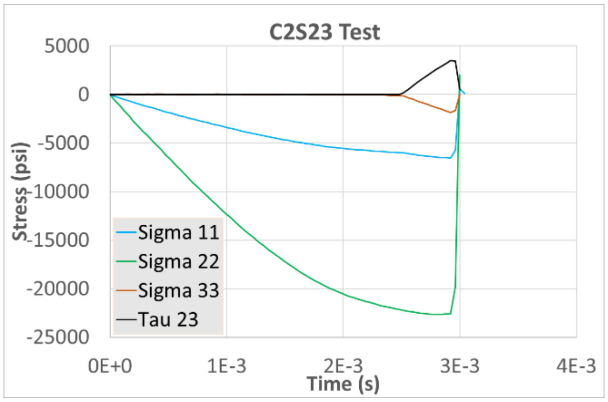

(a)

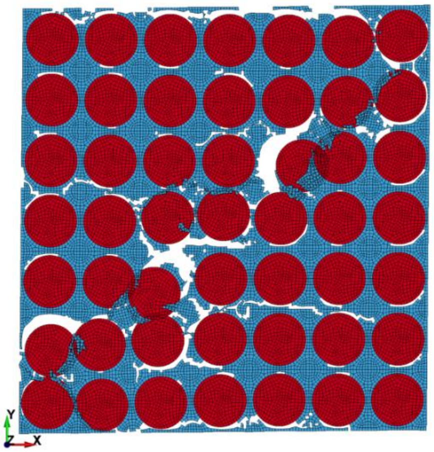

(b)

Figure 5.20. C2S23 test, compression dominated failure. (a) Stress vs time curve (b) failed specimen

Figure 5.20(a) on the other hand, shows a compression dominated failure with the nonlinear behavior of the matrix visible. The failed specimen in figure 5.20(b) shows the prevalence of the diagonal crack through the model, which is typical of compression dominated failure modes.

Discussion: Two failure modes are observed in this test, namely the 2-3 plane shear dominated failure mode and the transverse compression dominated failure mode. The crack patterns in shear mode shows cracks across the model while in the compression dominated failure mode, a predominant crack develops along the diagonal axis of the model, which is consistent with compression failure mode.

FAILURE SURFACE IN THE $\sigma_2 - \tau_{23}$ SPACE

Results and discussion

The input values for plotting Puck and Tsai-Wu failure criteria as shown in figure 5.21 based on equations 2.13-2.14 and 2.18 respectively are given in table 5.5. The failure surface for the $\sigma_2 - \tau_{23}$ stress space is shown in figure 5.21. The virtual test response agrees well with Puck and Tsai-Wu predictions in the tension and shear dominated failure zone while compression dominated failure predictions are conservative. This is because the compressive strength was underpredicted during the validation tests in chapter 4.

Table 5.5. Input parameter for plotting Puck and Tsai-Wu failure criteria in the $\sigma_2 - \tau_{23}$ space

Parameter	Input value	Source
$R_{\perp}^{At}$ (Y_T)	6471 psi	(Khaled, et al., 2018)
Y_C	25530 psi	(Khaled, et al., 2018)
S_{23}	7280 psi	(Khaled, et al., 2018)

$R_{\perp\perp}^{A}$	9250 psi	Computed from eq. 2.12
$p_{\perp\perp}^{(-)} = p_{\perp\perp}$	0.38	Computed from eq. 2.11

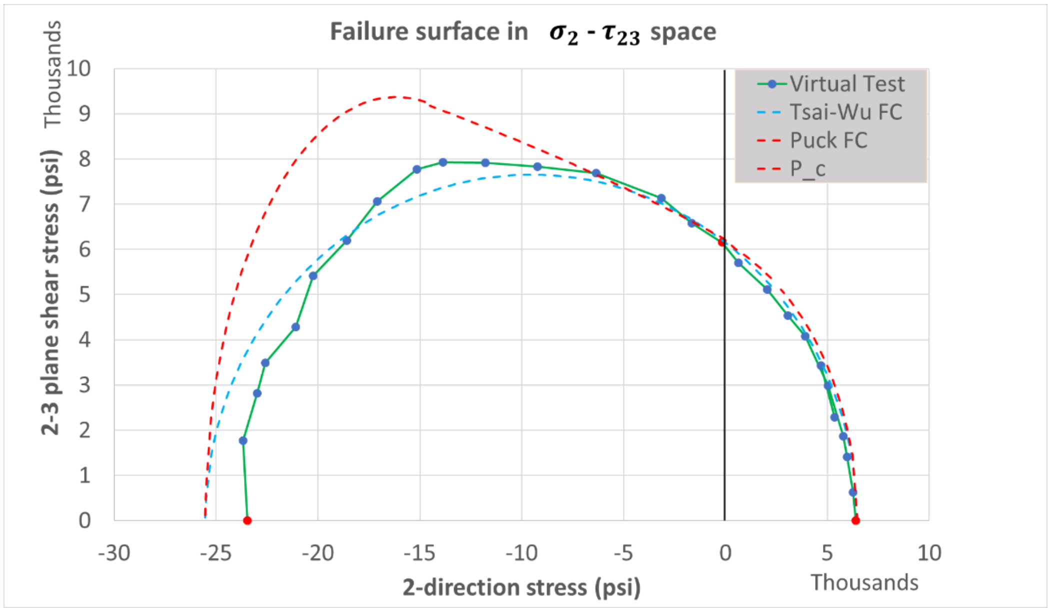

Figure 5.21. Failure surface in the $\sigma_2 - \tau_{23}$ stress space

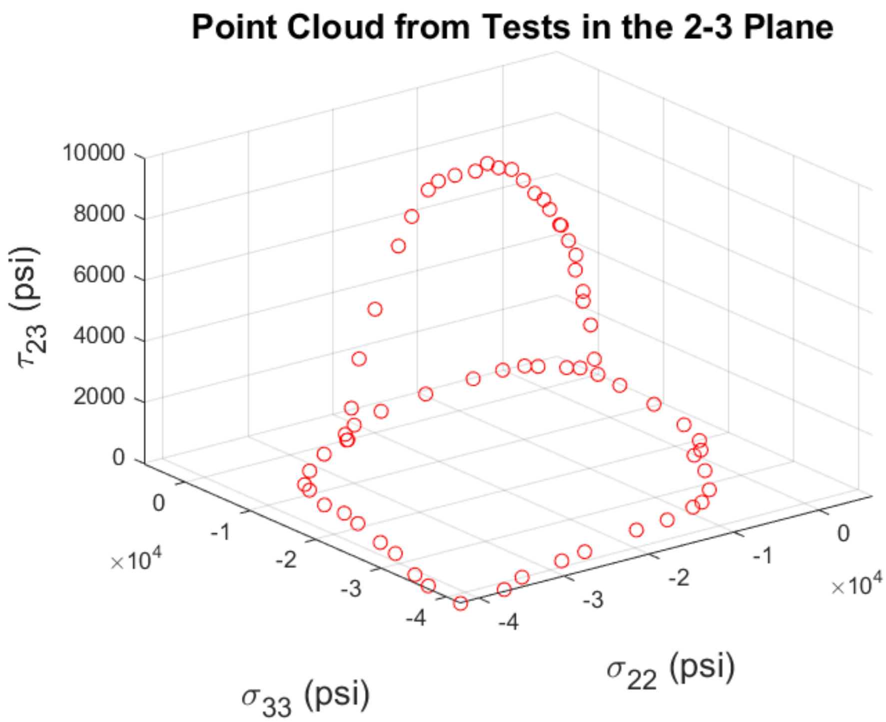

Figure 5.22. Point Cloud representation of failure data in the 2-3 plane

The point cloud representation of the failure surface shows the data in a three-dimensional space.

5.3. USING POINT CLOUD DATA FOR FAILURE PREDICTION

Summary of Point Cloud Failure Surface (PCFS) data

The biaxial tests on the in-plane model produced three non-zero stress components. This represents a three-dimensional point cloud failure surface in the principal material direction (PMD) stress space. The biaxial tests on the out-of-plane model (S2-S3 or S2-S23 model) generated data to cover a four-dimensional point cloud failure surface. The three-dimensional (1-2 plane) and four-dimensional (2-3 plane) stress spaces are divided each into octants and bins respectively depending on the sign of each stress component. The data generated in the biaxial tests discussed in section 5.1 and 5.2 is summarized in tables 5.6 for in-plane data and 5.7 for out-of-plane data.

Table 5.6. Summary of in-plane failure data

Test	σ_1 **(psi)**	σ_2 **(psi)**	τ_{21} **(psi)**
S1-S2 Model			
T1	383068	14.3	0
C1	-112792	-2.4	0
T2	-9	6201	0
C2	-174.5	-24704	-13
C1T2_R1	-113081	6680	0
C1T2_R2	-49889	6595	0
C1T2_R3	-90079	6897	0
C1T2_R4	-110985	2796	0

T1T2_R1	89690	5519	0
T1T2_R2	120031	5132	0
T1T2_R3	137601	5003	0
T1T2_R4	360154	3714	0
T1T2_R5	288779	3873	0
T1T2_R6	241112	4055	0
T1C2_R1	252681	-24305	0
T1C2_R2	131596	-24817	0
T1C2_R3	379136	-15084.2	0
T1C2_R4	380144	-21572	1
T1C2_R5	387874	-4220	0
T1C2_R6	302713	-24036	0
T1C2_R7	93221	-25031	0
T1C2_R8	165911	-24673	0
T1C2_R9	385885	-12029	0
T1C2_R10	48004	-25181	0
C1C2_R1	-116697	-10160	0
C1C2_R2	-68070	-25664	0
C1C2_R3	-117549	-25285	0
C1C2_R4	-115868	-5994	0
C1C2_R5	-110903	-3072	0
C1C2_R6	-117876	-21374	0
C1C2_R7	-116769	-15141	0
C1C2_R8	-112792	-2	0
S2-S21 Model			
T2	255	6133	0
C2	-1922	-24010	1
S21	-1001	-125	7010

T2S21_R1	251	6083	792
T2S21_R2	257	6061	1962
T2S21_R3	264	5271	3394
T2S21_R4	204	4655	4180
T2S21_R5	-251	2726	5490
C2S21_R1	-1768	-23756	2113
C2S21_R2	-1895	-23961	919
C2S21_R3	-1268	-23261	3608
C2S21_R4	-945	-22851	4427
C2S21_R5	-367	-21548	5367
C2S21_R6	-926	-20014	6235
C2S21_R7	-1410	-18348	6913
C2S21_R8	-1426	-16417	7436
C2S21_R9	-1868	-14558	7798
C2S21_R10	-2364	-10634	8117
C2S21_R11	-1817	-13498	7947
C2S21_R12	-4382	-9736	8125
C2S21_R13	-4215	-7133	7966
C2S21_R14	-4032	-4772	7586
C2S21_R15	-4162	-3001	7219
Minimum	**-117876**	**-25664**	**-13**
Maximum	**387874**	**6897**	**8125**

Table 5.7. Summary of out-of-plane failure data

Test	σ_1 **(psi)**	σ_2 **(psi)**	σ_3 **(psi)**	τ_{23} **(psi)**
T2	1765	6343	-4	0
T3	1765	-4	6343	0

C2	-6348	-23214	-122	5
C3	-6348	-122	-23214	5
S23	-79	-153	-153	5697
T2T3_R2	2335	5152	3253	0
T2T3_R3	2255	6096	2418	0
T2T3_R4	2334	3250	5150	0
T2T3_R5	2318	2328	6016	0
T2C3_R1	693	6124	-3648	0
T2C3_R2	-1166	5485	-9733	0
T2C3_R3	-3185	4259	-15935	0
T2C3_R4	-4766	2767	-20254	0
T2C3_R5	-5779	1261	-22452	0
C2C3_R1	-7881	-1865	-27139	-3
C2C3_R2	-9834	-4760	-31595	0
C2C3_R3	-11166	-7415	-33898	0
C2C3_R4	-11724	-8901	-34466	0
C2C3_R5	-13178	-12982	-35841	5
C2C3_R6	-14338	-16947	-36278	3
C2C3_R7	-16766	-24389	-38019	-7
C2C3_R8	-17840	-27680	-38796	7
C2C3_R10	-19679	-33355	-40084	4
C2C3_R11	-20992	-36762	-41801	6
C2C3_R12	-22535	-42271	-42274	-5
C2C3_R13	-21001	-41839	-36759	19
C2C3_R14	-19917	-40903	-33476	7
C2C3_R15	-17840	-38776	-27704	6
C2C3_R16	-16770	-38018	-24405	0
C2C3_R17	-14936	-36510	-18988	1

C2C3_R18	-13939	-35749	-15910	-4
C2C3_R19	-13180	-35841	-12986	-2
C2C3_R20	-11726	-34470	-8905	-3
C2C3_R21	-11168	-33903	-7416	-1
C2C3_R22	-9727	-31236	-4711	-2
C2C3_R23	-7946	-27361	-1890	1
C2T3_R1	693	-3648	6124	0
C2T3_R2	-1160	-9728	5502	0
C2T3_R3	-3185	-15935	4261	0
C2T3_R4	-4764	-20251	2769	0
C2T3_R5	-5778	-22448	1262	-1
T2S23_R1	1792	6245	251	0
T2S23_R2	1167	3919	238	3429
T2S23_R3	1535	5041	483	2291
T2S23_R4	1706	5775	396	1404
T2S23_R5	610	2059	82	4537
T2S23_R6		5356		1863
T2S23_R7	206	632	104	5110
T2S23_R8	914	3049	181	4076
T2S23_R9	1781	5978	477	627
C2S23_R1	-1145	-3156	-928	6582
C2S23_R2	-663	-1647	-723	6148
C2S23_R3	-2130	-6359	-1410	7133
C2S23_R4	-2942	-9238	-1607	7681
C2S23_R5	-3666	-11785	-1811	7827
C2S23_R6	-4649	-15159	-2161	7928
C2S23_R7	-4265	-13869	-2000	7911
C2S23_R8	-5164	-17101	-2143	7775

C2S23_R9	-5536	-18598	-2030	7064
C2S23_R10	-6105	-21100	-1649	5417
C2S23_R11	-6619	-22974	-1701	3492
C2S23_R12	-6814	-23675	-1723	1775
C2S23_R13	-5982	-20237	-2069	6199
C2S23_R14	-6550	-22580	-1844	4280
Minimum	**-22535**	**-42271**	**-42274**	**-7**
Maximum	**2335**	**6343**	**6343**	**7928**

The distribution of the data in octants for the in-plane point cloud is shown in table 5.8. The data is unevenly distributed due to the loading conditions. Only uniaxial and biaxial loading tests were carried out to generate the failure states of stress. Octant IV covering compressive stress in the 1- and 2-directions, and 2-1 plane shear has the most data. The loading pattern needs to be modified to obtain an even distribution of the data.

Table 5.8. In-plane failure data distribution in octants

OCTANT	**Signs** $(\sigma_1, \sigma_2, \tau_{21})$	**Number**	**Percent (%)**
I	(+, +, +)	7	13.7
II	(-, +, +)	3	5.9
III	(+, -, +)	8	15.7
IV	(-, -, +)	21	41.2
V	(+, +, -)	4	7.8
VI	(-, +, -)	2	3.9
VII	(+, -, -)	2	3.9
VIII	(-, -, -)	4	7.8

For out-of-plane data, the 4-dimensional space is divided into 16 bins and the distribution of failure data is shown in table 5.9. Some of the data is sparsely distributed, e.g., 8 bins have no data. This is because the loading was biaxial in the 2-3 plane. To achieve better distribution, the loading needs to be modified and is the subject of future work.

Table 5.9. Out-of-plane failure data distribution in bins

BIN	**Signs** $(\sigma_1, \sigma_2, \sigma_3, \tau_{23})$	**Number**	**Percent (%)**
I	(+, +, +, +)	12	18.2
II	(+, +, +, -)	0	0.0
III	(+, +, -, +)	2	3.0
IV	(+, +, -, -)	1	1.5
V	(+, -, +, +)	3	4.5
VI	(+, -, +, -)	0	0.0
VII	(+, -, -, +)	0	0.0
VIII	(+, -, -, -)	0	0.0
IX	(-,+,+, +)	0	0.0
X	(-, +, +, -)	0	0.0
XI	(-, +, -, +)	0	0.0
XII	(-, +, -, -)	4	6.1
XIII	(-, -, +, +)	1	1.5
XIV	(-, -, +, -)	3	4.5
XV	(-, -, -, +)	30	45.5
XVI	(-, -, -, -)	10	15.2

Validation of the generated point cloud failure surface data can be carried out in a standalone computer program (Rajan, et al., 2021) and is not discussed here.

Generalized Tabulated Failure Criteria Data

A Generalized Tabulated Failure Criterion (GTCF) was developed to define a failure surface based on tabulated data (Goldberg, et al., 2018). Instead of using mathematical expressions to define the failure criterion, points on the failure surface are defined using cylindrical type of coordinate system. In the current implementation of MAT_213, GTFC has been modified to include the in-plane and out-of-plane stresses and strains (Shyamsunder, et al., 2021). The failure states are defined in terms of equivalent failure strain and failure angle space (Shyamsunder, et al., 2019). An in-plane failure surface is defined by the equivalent strain ε_{IP}^{eq} (equation 5.1) as a function of failure angle θ_{IP} (equation 5.2) computed using σ_{11}. The in-plane failure state d_1 is computed as shown in equation 5.3.

$$\varepsilon_{IP}^{eq} = \sqrt{\varepsilon_{11}^2 + \varepsilon_{22}^2 + 2\varepsilon_{12}^2} \tag{5.1}$$

$$\theta_{IP} = \cos^{-1}\left(\frac{\sigma_{22}}{\sqrt{\sigma_{22}^2 + \sigma_{12}^2}}\right) \tag{5.2}$$

$$d_1 = \frac{\varepsilon_{IP}^{eq}}{\varepsilon_{IP^{FAIL}}^{eq}} \tag{5.3}$$

An out-of-plane failure surface is similarly defined in terms of equivalent strain ε_{OOP}^{eq} (shown in equation 5.4) as a function of failure angle θ_{OOP} (in equation 5.5). The out-of-plane failure state d_2 is computed using equation 5.6.

$$\varepsilon_{OOP}^{eq} = \sqrt{\varepsilon_{33}^2 + 2\varepsilon_{13}^2 + 2\varepsilon_{23}^2} \tag{5.4}$$

$$\theta_{OOP} = \cos^{-1}\left(\frac{\sigma_{13}}{\sqrt{\sigma_{13}^2+\sigma_{23}^2}}\right) \tag{5.5}$$

$$d_2 = \frac{\varepsilon_{OOP}^{eq}}{\varepsilon_{OOP^{FAIL}}^{eq}} \tag{5.6}$$

The finite element is eroded if $d > 1$

$$d = \begin{cases} \max\left(d_1, d_2\right) & \text{if } n = 0 \\ \sqrt[n]{\left(d_1\right)^n + \left(d_2\right)^n} & \text{if } n > 0 \end{cases} \tag{5.7}$$

The failure data that was obtained in sections 5.1 can be used to compute in-plane failure surface for GTFC. The summary table for the in-plane equivalent failure angle computed with equation 5.2 and in-plane failure angle computed with equation 5.1 are shown in table 5.10 and 5.11 respectively. The out-of-plane failure surface requires a non-zero 1-3 plane shear component. Test cases accounting for the 1-3 plane shear components will be the subject of future work. Thus out-of-plane data for GTFC have not been computed.

Table 5.10. In-plane failure angle to be used in GTFC

Test	$\boldsymbol{\sigma_1}$ **(psi)**	$\boldsymbol{\sigma_2}$ **(psi)**	$\boldsymbol{\tau_{21}}$ **(psi)**	$\boldsymbol{\theta_{IP}}$ **(psi)**
T2	0	6100	0	0
S21	-1000	-100	7000	91
C2	-2000	-24000	0	180
T2S21_R1	0	6100	800	7
T2S21_R2	0	6100	2000	18
T2S21_R3	0	5300	3400	33
T2S21_R4	0	4700	4200	42

T2S21_R5	0	2700	5500	64
C2S21_R1	-4000	-3000	7200	113
C2S21_R2	-2000	-23800	2100	175
C2S21_R3	-2000	-24000	900	178
C2S21_R4	-1000	-23300	3600	171
C2S21_R5	-1000	-22900	4400	169
C2S21_R6	0	-21500	5400	166
C2S21_R7	-1000	-20000	6200	163
C2S21_R8	-1000	-18300	6900	159
C2S21_R9	-1000	-16400	7400	156
C2S21_R10	-2000	-14600	7800	152
C2S21_R11	-2000	-10600	8100	143
C2S21_R12	-2000	-13500	7900	150
C2S21_R13	-4000	-9700	8100	140
C2S21_R14	-4000	-7100	8000	132
C2S21_R15	-4000	-4800	7600	122
C1T2_R1	-113000	6700	0	0
C1T2_R2	-50000	6600	0	0
C1T2_R3	-90000	6900	0	0
C1T2_R4	-111000	2800	0	0
T1T2_R1	90000	5500	0	0
T1T2_R2	120000	5100	0	0
T1T2_R3	138000	5000	0	0
T1T2_R4	360000	3700	0	0
T1T2_R5	289000	3900	0	0
T1T2_R6	241000	4100	0	0
T1C2_R1	48000	-25200	0	180
T1C2_R2	132000	-24800	0	180
T1C2_R3	379000	-15100	0	180

T1C2_R4	380000	-21600	0	180
T1C2_R5	388000	-4200	0	180
T1C2_R6	303000	-24000	0	180
T1C2_R7	93000	-25000	0	180
T1C2_R8	166000	-24700	0	180
T1C2_R9	386000	-12000	0	180
T1C2_R10	253000	-24300	0	180
C1C2_R1	-117000	-10200	0	180
C1C2_R2	-68000	-25700	0	180
C1C2_R3	-118000	-25300	0	180
C1C2_R4	-116000	-6000	0	180
C1C2_R5	-111000	-3100	0	180
C1C2_R6	-118000	-21400	0	180
C1C2_R7	-117000	-15100	0	180
Minimum	**-118000**	**-25700**	**0**	**0**
Maximum	**388000**	**6900**	**8100**	**180**

Table 5.11. Equivalent failure strain to be used in GTFC

Test	ε_{11}	ε_{22}	ε_{21}	ε_{IP}^{eq}
T2	-5.77E-05	5.94E-03	-1.21E-07	5.94E-03
C2	1.94E-04	-3.46E-02	4.26E-06	3.46E-02
S21	1.65E-04	-2.07E-04	7.01E-03	7.02E-03
T2S21_R1	-5.89E-05	5.89E-03	7.21E-04	5.94E-03
T2S21_R2	-4.84E-05	5.93E-03	1.82E-03	6.20E-03
T2S21_R3	-1.47E-05	5.14E-03	3.16E-03	6.04E-03
T2S21_R4	1.00E-05	4.56E-03	3.93E-03	6.02E-03
T2S21_R5	8.10E-05	2.52E-03	5.30E-03	5.88E-03
C2S21_R1	1.32E-04	-3.12E-03	8.43E-03	8.99E-03

C2S21_R2	2.49E-04	-3.56E-02	3.48E-03	3.58E-02
C2S21_R3	1.98E-04	-3.48E-02	1.46E-03	3.48E-02
C2S21_R4	4.12E-04	-3.76E-02	6.59E-03	3.81E-02
C2S21_R5	5.91E-04	-3.92E-02	8.87E-03	4.02E-02
C2S21_R6	7.13E-04	-3.56E-02	1.04E-02	3.71E-02
C2S21_R7	7.01E-04	-3.07E-02	1.08E-02	3.26E-02
C2S21_R8	7.00E-04	-2.68E-02	1.13E-02	2.91E-02
C2S21_R9	6.81E-04	-2.28E-02	1.15E-02	2.55E-02
C2S21_R10	6.66E-04	-1.96E-02	1.18E-02	2.29E-02
C2S21_R11	5.62E-04	-1.35E-02	1.14E-02	1.77E-02
C2S21_R12	6.44E-04	-1.78E-02	1.17E-02	2.13E-02
C2S21_R13	2.71E-04	-1.01E-02	9.55E-03	1.39E-02
C2S21_R14	2.08E-04	-7.30E-03	9.18E-03	1.17E-02
C2S21_R15	1.70E-04	-4.89E-03	8.73E-03	1.00E-02
C1T2_R1	-6.26E-03	7.82E-03	2.48E-08	1.00E-02
C1T2_R2	-2.80E-03	7.03E-03	1.16E-08	7.56E-03
C1T2_R3	-5.00E-03	7.82E-03	-6.73E-09	9.29E-03
C1T2_R4	-6.10E-03	3.82E-03	-2.54E-08	7.20E-03
T1T2_R1	3.51E-03	4.42E-03	-3.30E-08	5.65E-03
T1T2_R2	4.72E-03	3.72E-03	2.23E-08	6.01E-03
T1T2_R3	5.43E-03	3.42E-03	8.32E-09	6.41E-03
T1T2_R4	1.43E-02	1.44E-04	-8.46E-09	1.43E-02
T1T2_R5	1.15E-02	9.09E-04	-2.71E-08	1.15E-02
T1T2_R6	9.55E-03	1.51E-03	-3.15E-08	9.67E-03
T1C2_R1	2.16E-03	-4.60E-02	1.36E-08	4.60E-02
T1C2_R2	5.49E-03	-4.57E-02	1.89E-07	4.60E-02
T1C2_R3	1.52E-02	-1.96E-02	-9.43E-09	2.49E-02
T1C2_R4	1.54E-02	-3.35E-02	5.71E-07	3.69E-02
T1C2_R5	1.55E-02	-7.90E-03	-2.19E-07	1.74E-02

T1C2_R6	1.23E-02	-4.56E-02	1.12E-07	4.72E-02
T1C2_R7	3.96E-03	-4.62E-02	1.80E-07	4.63E-02
T1C2_R8	6.86E-03	-4.57E-02	2.18E-07	4.62E-02
T1C2_R9	1.55E-02	-1.59E-02	1.79E-07	2.22E-02
T1C2_R10	1.03E-02	-4.58E-02	1.07E-08	4.70E-02
C1C2_R1	-6.26E-03	-7.91E-03	1.76E-08	1.01E-02
C1C2_R2	-3.45E-03	-4.58E-02	1.94E-08	4.59E-02
C1C2_R3	-6.16E-03	-4.06E-02	-4.32E-08	4.10E-02
C1C2_R4	-6.26E-03	-3.95E-03	5.59E-08	7.40E-03
C1C2_R5	-6.02E-03	-1.21E-03	1.53E-07	6.14E-03
C1C2_R6	-6.21E-03	-2.21E-02	1.09E-08	2.30E-02
C1C2_R7	-6.21E-03	-1.31E-02	-2.56E-08	1.45E-02
Minimum	**-6.26E-03**	**-4.62E-02**	**-2.19E-07**	**5.65E-03**
Maximum	**1.55E-02**	**7.82E-03**	**1.18E-02**	**4.72E-02**

6. CONCLUDING REMARKS

The primary objective of this thesis was to use the currently developed explicit finite element analysis framework to create the point cloud failure surface for the T800/F3900 unidirectional composite. The modeling was done at the constituent level to include the properties of the fiber and matrix. Two sets of RUC-based finite element models were created.

The first set was used to generate the point cloud failure data in the 1-2 plane as $(\sigma_1, \sigma_2, \tau_{12})$ data. Three-dimensional models labeled the S1-S2 and S2-S21 models, were generated from a square packing of repeated unit cells to analyze the loading in the longitudinal and transverse direction as well as in-plane shear. Validation tests were performed through a series of uniaxial loading in the 1-direction tension and compression, and 2-direction tension and compression. Agreement with experimental data was generally observed. Biaxial tests were then performed on the three-dimensional models to generate additional in-plane failure data. These include biaxial tension in the 1 and 2 directions, biaxial tension in the 1-direction and compression in the 2-direction, biaxial compression in the 1-direction and compression in the 2-direction, biaxial compression in the 2 and 3-directions, biaxial tension in the 2-direction and 2-1 plane shear, and biaxial compression in the 2-direction and 2-1 plane shear. In each test, a set of failure points were generated by changing the loading rate in each direction. The failure modes in a selected number of tests were analyzed and failure surfaces were plotted and compared to Puck and Tsai-Wu failure criteria. It was observed that under longitudinal stress dominated tests, failure initiates in the fiber while under transverse stress dominated tests, failure initiates in the matrix mostly with a crack in the direction perpendicular to the transverse loading direction. The strength prediction agreed well under tension dominated failure while the virtual test produced conservative predictions under shear and compression dominated failure when these loadings are combined.

The second set was used to generate points in the 2-3 plane as $(\sigma_1, \sigma_2, \sigma_3, \tau_{23})$ data. For these plane strain analyses, the influence of the number of repeating unit cells to the response of the composite was evaluated. It was shown that the response of the model made of 49 repeating unit cells (RUC) showed an agreement with the uniaxial 2-direction tension and 2-direction compression. The effect of the mesh density as well as the gauge section was also investigated. Biaxial loading was then performed on the 49 RUC model to generate failure data. The biaxial test carried out include biaxial tension in the 2 and 3 directions, biaxial tension in the 2-direction and compression in the 3-direction, biaxial compression in the 2-direction and tension in the 3-direction, biaxial compression in the 2 and 3 directions, biaxial tension in the 2 direction and 2-3 plane shear, and biaxial compression in the 2-direction and 2-3 plane shear. For each biaxial test, the ratio between loading rates was varied to produce a set of data points in the stress space. The failure surface for the corresponding stress spaces were plotted and compared to Puck and Tsai-Wu failure surfaces. The virtual test prediction for compression dominated failure under combined transverse compression and 2-3 plane shear was conservative. The point cloud representation of all failure points was plotted for in-plane and out-of-plane data.

The point cloud failure criterion (PCFC) does not assume a shape of the failure surface. Rather it uses failure data as generated through virtual testing. The accuracy of the predictions increases with increase in failure data in the point cloud. PCFC gives closed failure surfaces in all stress spaces examined in this study. It should be noted that both Puck and Tsai-Wu failure criteria cannot predict failure under biaxial normal compressive load in the 2-3 plane. Populating the PCFS requires a series of multiaxial tests so as to cover the 3, 4 and 6-dimensional stress spaces. For each surface, the appropriate model needs to be generated and validated. The computational cost for models with large number of finite elements

The current work can be extended with these additional tasks:

- Automate the entire process for failure data generation through scripts that would generate the finite element models, submit jobs for finite element analysis, and post-process the results.
- Generate failure data to evenly and densely populate the point cloud by considering multiaxial loading conditions.
- The developed framework can be adapted to generate failure data for other composite architectures such as multidirectional composites and woven composites.
- Include rate and temperature effects in the simulations when the composite constituents exhibit rate and temperature effects.
- Implement the PCFC including the needed ANN capabilities in LS-DYNA as a part of MAT_213.

.

REFERENCES

Aboudi, J., 2004. The Generalized Method of Cells and High-Fidelity Generalized Method of Cells Micromechanical Models—A Review. *Mechanics of Advanced Materials and Structures,* 11(4-5), pp. 329-366.

ANSYS-LST, 2020. *LS-DYNA Keyword User's manual, Volume II - Material Models.* s.l.:s.n.

Arya, S. & Mount, D., 1993. *Algorithms for a Fast Vector Quantization. In JA Storer and M. Cohn Editors, Proc. of DCC '93: Data Compression Conference, 381-390, IEEE Press.* s.l., IEEE, pp. 381-390.

Azzi, V. & Tsai, S., 1965. Anisotropic strength of composites. *Experimental Mechanics,* Volume 5, p. 283–288.

Barbero, E. J., 2013. *Finite Element Analysis of Composite Materials Using AbaqusTM.* London: CRC Press.

Bednarcyk, B. & Arnold, S., 2002. *MAC/GMC 4.0 User's Manual: Keywords Manual,* Springfield, VA: National Technical Information Service.

Camanho, P. et al., 2015. Three-dimensional invariant-based failure criteria for fiber-reinforced composites,. *International Journal of Solids and Structures,,* Volume 55, pp. 92-107.

Canal, L. P., Segurado, J. & LLorca, J., 2009. Failure surface of epoxy-modified fiber-reinforced composites under transverse tension and out-of-plane shear. *International Journal of Solids and Structures,* 46(11-12), pp. 2265-2274.

Daniel, I., Daniel, S. & Fenner, J., 2018. A new yield and failure theory for composite materials under static and dynamic loading. *International Journal of Solids and Structures,* Volume 148–149, pp. 79-93.

Davila, C., Camanho, P. & Rose, C., 2005. Failure Criteria for FRP Laminates. *Journal of Composite Materials,* 39(4), pp. 323-345.

Deuschle, H. M. & Kröplin, B.-H., 2012. Finite element implementation of Puck's failure theory for fibre-reinforced composites under three-dimensional stress. *Journal of Composite Materials,* Volume 46, pp. 2485-2513.

Gao, L., Wang, C., Liu, Z. & Zhuang, Z., 2017. Theoretical aspects of selecting repeated unit cell model in micromechanical analysis using displacement-based finite element method,. *Chinese Journal of Aeronautics,* Volume 30, pp. 1417-1426.

Goldberg, R. et al., 2016. Development of an Orthotropic Elasto-Plastic Generalized Composite Material Model Suitable for Impact Problems. *Journal of Aerospace Engineering,* Volume 29, p. 04015083.

Goldberg, R. K. et al., 2018. Implementation of a tabulated failure model into a generalized composite material model. , 52(25. *Journal of Composite Materials,* 52(25), p. 3445–3460.

Harrington, J., 2015. *Using virtual testing for characterization of composite materials.*, MS Thesis, Tempe: Arizona State University.

Harrington, J. et al., 2017. Using Virtual Tests to Complete the Description of a Three-Dimensional Orthotropic Material. *American Society of Civil Engineers,* Volume 5.

Hart-Smith, L., 1998. Predictions of the original and truncated maximum-strain failure models for certain fibrous composite laminates. *Composites Science and Technology,* 58(7), pp. 1151-1178.

Hashin, Z., 1980. Failure Criteria for Unidirectional Fiber Composites. *Journal of Applied Mechanics,* 47(2), pp. 329 - 334.

Hazanov, S. & Amieur, M., 1995. On overall properties of elastic heterogeneous bodies smaller than the representative volume. *International Journal of Engineering Science,* 33(9), pp. 1289-1301.

Herrάez, M., Bergan, A., Gonzalez, C. & and Lopes, C., 2018. *Modeling Fiber Kinking at the Microscale and Mesoscale,* s.l.: s.n.

Hinton, M. & Kaddour, A., 2012. The background to the Second World-Wide Failure Exercise. *Journal of Composite Materials,* 46(19-20), pp. 2283 - 2294.

Hinton, M., Kaddour, A. & Soden, P. eds., 2004a. *Failure criteria in fibre reinforced polymer composites: The World-Wide Failure Exercise.* Oxford: Elsevier Science Ltd.

Hinton, M., Kadour, A. & Soen, P., 2004b. The world-wide failure exercise: Its origin, concept and content. In: *Failure Criteria in Fibre-Reinforced Polymer Composite.* s.l.:Elsevier, pp. 2-28.

Hoffarth, C. et al., 2017. Verification and validation of a three-dimensional Orthotropic Plasticity constitutive model using a unidirectional composite. *Fibers,* Volume 5, pp. 1-13.

Hoffarth, C. et al., 2016. Implementation and validation of a three-dimensional plasticity-based deformation model for orthotropic composites. *Composites Part A: Applied Science and Manufacturing,* Volume 91, pp. 336-350.

Holt, N., 2018. *Experimental and Simulation Validation Tests for MAT 213,* MS Thesis, Tempe, AZ: Arizona State University.

Kaddour, A. & Hinton, M., 2010. Progress in failure criteria for polymer matrix composites: A view from the first World-Wide Failure Exercise (WWFE). In: *Failure Mechanisms in Polymer Matrix Composites.* Paul Robinson, Emile Greenhalgh, Silvestre Pinho ed. s.l.:Woodhead Publishing, pp. 3-25.

Kaddour, A. & Hinton, M., 2013. Maturity of 3D failure criteria for fibre-reinforced composites: Comparison between theories and experiments: Part B of WWFE-II. *Journal of Composite Materials,* 47(6-7), pp. 925-966.

Kaddour, A. & Hinton, M., 2018. Failure Criteria for Composites. In: W. Beaumont & C. Zweben, eds. *Comprehensive Composite Materials II.* s.l.:Elsevier, pp. 573-600.

Kaddour, A., Hinton, M., Smith, P. & Li, S., 2013. The background to the third world-wide failure exercise.. *Journal of Composite Materials,* 47(20–21), p. 2417–2426.

Kanit, T. et al., 2003. Determination of the size of the representative volume element for random composites: statistical and numerical approach. *International Journal of Solids and Structures,* 40(13-14), pp. 3647-3679.

Khaled, B. et al., 2018. Experimental characterization of composites to support an orthotropic plasticity material model. *Journal of Composite Materials*, Volume 52, pp. 1847-1872.

Khaled, B. et al., 2021. Framework for predicting failure in polymeric unidirectional composites through combined experimental and computational mesoscale modelling techniques. *Submitted to Fibers.*

Kolling, S., Haufe, A., Feucht, M. & Bois, P. D., 2005. *A semianalytical model for thesimulation of polymers.* Bamberg, Germany, s.n.

Li, S., 2008. Boundary conditions for unit cells from periodic microstructures and their implications. *Composites Science and Technology,* 68(9), pp. 1962-1974.

Li, S. & Sitnikova, E., 2018. A critical review on the rationality of popular failure criteria for composites. *Composites Communications,* Volume 8, pp. 7-13.

Li, S. & Sitnikova, E., 2020. Chapter 4 - Representative volume elements and unit cells. In: *Representative Volume Elements and Unit Cells.* s.l.:Woodhead Publishing, pp. 67-77.

Li, S., Sitnikova, E., Liang, Y. & Kaddour, A., 2017. The Tsai-Wu failure criterion rationalised in the context of UD composites. *Composites Part A: Applied Science and Manufacturing*, Volume 102, pp. 207-217.

Liu, Z. et al., 2018. Multiscale simulations of material with heterogeneous structures based on representative volume element techniques. *15th International LS-DYNA Users Conference*, pp. 1-10.

Mount, D., 2010. *ANN Programming Manual, ANN Version 1.1,, last accessed Dec 28, 2020.* [Online]
Available at: https://www.cs.umd.edu/~mount/ANN/
[Accessed 28 December 2020].

Naya, F. et al., 2017. Computational micromechanics of the transverse and shear behavior of unidirectional fiber reinforced polymers including environmental effects. *Composites Part A: Applied Science and Manufacturing,* Volume 92, pp. 146-157.

Pahr, D. H. & Böhm, H., 2008. Assessment of Mixed Uniform Boundary Conditions for Predicting the Mechanical Behavior of Elastic and Inelastic Discontinuously Reinforced Composites. *CMES - Computer Modeling in Engineering and Sciences*, 34(2), p. 117–136.

Parakhiya, Y., 2020. *Framework for Generating Failure Surface through Virtual Testing of Uni-directional Polymeric Composite,* MS Thesis, Tempe, AZ: Arizona State University.

Pinho, S. et al., 2005. Failure models and criteria for FRP under in-plane and three-dimensional stress states including shear non-linearity. In: *NASA/TM-2005-213530.* s.l.:s.n.

Pinho, S., Iannucci, L. & Robinson, P., 2006. Physically-based failure models and criteria for laminated fibre-reinforced composites with emphasis on fibre kinking: Part I: Development. *Composites Part A: Applied Science and Manufacturing,* 37(1), pp. 63-73.

Puck, A. & Deuschle, H., 2013. Progress in the Puck Failure Theory for Fibre Reinforced Composites : Analytical solutions for 3 D-stress..

Puck, A., Kopp, J. & Knops, M., 2002. Guidelines for the determination of the parameters in Puck's action plane strength criterion. *Composites Science and Technology,* 62(3), pp. 371-378.

Puck, A. & Schürmann, H., 1998. Failure analysis of FRP laminates by means of physically based phenomenological models. *Composites Science and Technology,* 58(7), pp. 1045-1067.

Rajan, S., Khaled, B. & Shyamsunder, L., 2021. Point Cloud Failure Criterion for Composites using k-Nearest Neighbor Classification.. *arXiv preprint arXiv:2106.02714.*

Raju, K. & Acosta, J., 2010. *Crashworthiness of composite fuselage structures-Material dynamic properties,* Springfiled, VA: National Technical Information Service.

Robbins, J., 2019. *On Building Blocks for Virtual Testing of Unidirectional Polymeric Composites,* MS Thesis, Tempe, AZ: Arizona State University.

Rodríguez, M., Molina-Aldareguía, J., González, C. & LLorca, J., 2012. A methodology to measure the interface shear strength by means of the fiber push-in test. *Composites Science and Technology*, 72(15), pp. 1924-1932.

Romanowicz, M., 2012. A numerical approach for predicting the failure locus of fiber reinforced composites under combined transverse compression and axial tension. *Computational Materials Science,* 51(1), pp. 7-12.

Shyamsunder, L., Khaled, B. & Rajan, S., 2019. MAT_213 v1.3.5 Status. In: *FAA research project monthly teleconference.* Tempe, AZ: s.n.

Shyamsunder, L., Khaled, B., Rajan, S. & Blankenhorn, G., 2021. Improving Failure Sub-Models in an Orthotropic Plasticity-Based Material Model. *Journal of Composite Materials,* 55(15), p. 2025–2042.

Shyamsunder, L. et al., 2020. Implementing deformation, damage, and failure in an orthotropic plastic material model. *Journal of Composite Materials,* 54(4), p. 463–484.

Smith, D. L. & Dow, M. B., 1991. *Properties of Three Graphite/Toughened Resin Composites,* s.l.: s.n.

Sun, Q. et al., 2019. Failure criteria of unidirectional carbon fiber reinforced polymer composites informed by a computational micromechanics model. *Composites Science and Technology,* Volume 172, pp. 81-95.

Talreja, R., 2014. Assessment of the fundamentals of failure theories for composite materials. *Composites Science and Technology,* Volume 105, pp. 190-201.

Teklal, F. et al., 2018. A review of analytical models to describe pull-out behavior – Fiber/matrix adhesion. *Composite Structures*, Volume 201, pp. 791-815.

Totry, E., González, C. & LLorca, J., 2008a. Failure locus of fiber-reinforced composites under transverse compression and out-of-plane shear. *Composites Science and Technology,* Volume 68, pp. 829-839.

Totry, E., González, C. & LLorca, J., 2008b. Prediction of the failure locus of C/PEEK composites under transverse compression and longitudinal shear through computational micromechanics. *Composites Science and Technology,* 68(15-16), pp. 3128-3136.

Tsai, S. & Wu, E. M., 1971. A General Theory of Strength for Anisotropic Materials. *Journal of Composite Materials,* Volume 5, pp. 58-80.

Vajari, D., 2015. A micromechanical study of porous composites under longitudinal shear and transverse normal loading. *Composite Structures,* Volume 125, pp. 266-276.

Vaughan, T. & McCarthy, C., 2011. Micromechanical modelling of the transverse damage behaviour in fibre reinforced composites. *Composites Science and Technology,* 71(3), pp. 388-396.

Vogler, T., Hsu, T. & Kyriakides, S., 2000. Composite failure under combined compression and shear. *International Journal of Solids and Structures,* 37(12), pp. 1765-1791.

Zhou, X.-F., Wagner, H. & Nutt, S., 2001. Interfacial properties of polymer composites measured by push-out and fragmentation tests. *Composites Part A: Applied Science and Manufacturing,* 32(11), pp. 1543-1551.